Single crystal field-effect transistors based on layered semiconductors

Dissertation

zur Erlangung des akademischen Grades
des Doktors der Naturwissenschaften
(Dr. rer. nat.)
an der Universität Konstanz
Fachbereich Physik

vorgelegt von

Roswitha Zeis

April 2005

Referent: Prof. Dr. Ernst Bucher
Referent: Prof. Dr. Peter Wyder

meinen Eltern

Elfriede und Alfred Zeis

DANK

Von der Idee bis zur Fertigstellung haben viele Menschen zum Gelingen dieser Arbeit beigetragen. Bei ihnen allen möchte ich mich bedanken.

Mein besonderer Dank gilt:

- Meinem Doktorvater Prof. Ernst Bucher für die besondere Gelegenheit, die er mir bot, an den Bell Laboratorien zu forschen und seine Unterstützung auch in schweren Krisen,
- Prof. Peter Wyder für die spontane Zusage zur Zweitkorrektur,
- Dr. Ch. Kloc für die hervorragende fachliche Betreuung, die tatkräftige Unterstützung im Labor und den persönlichen, freundschaftlichen Umgangston,
- Dr. C. Besnard für das solidarische Miteinander nicht nur bei fachlichen Fragestellungen,
- Prof. T. Siegrist für seine Diskussionsfreude und Hilfsbereitschaft in jeder Lebenslage,
- C. G. Maclennan für die nette Einführung in die amerikanische Lebensweise und häufiges Korrekturlesen,
- allen Mitarbeitern der Bell Laboratorien für die angenehme Arbeitsatmosphäre,
- H. Riazi-Nejad für die Hilfestellung bei computertechnischen Problemen,
- der Konrad Adenauer Stiftung, dem Deutschen Akademischen Austauschdienst und der Landesgraduiertenförderung für die finanzelle Unterstützung.

List of publications

1. **Zeis R, Siegrist T, Kloc Ch**
   Single-crystal field-effect transistors based on copper phthalocyanine *Applied Physics Letters* 86 (2) 022103

2. **Zeis R, Takimiya K, Kunugi Y, Konda Y, Niihara N, Otsubo T, Kloc Ch**
   Single crystal field-effect transistors based on selenium containing organic semiconductor accepted in *Japanese Journal of Applied Physics*

3. **Zeis R, Besnard C, Siegrist T, Schlockermann C, Chi X, Kloc Ch**
   Field-effect studies on rubrene and impurities of rubrene submitted to *Chemistry of Materials*

4. **Kloc Ch, Zeis R, Williamson E, Chi X, Siegrist T, Ramirez AP.**
   Molecular engineering of TCNQ Perylene single crystals for n-type field effect transistor in preparation

5. **Podzorov V, Gershenson ME, Kloc Ch, Zeis R, Bucher E**
   High-mobility field-effect transistors based on transition metal dichalcogenides *Applied Physics Letters 84* (17): 3301 -3303

6. **Moon H, Zeis R, Borkent JE, Besnard C, Lovinger A, Siegrist T, Kloc Ch, Bao Z**
   Synthesis, Crystal structure and Transistor Performance of Tetracene Derivatives *Journal of the American Chemical Society* (Communication); 2004; 1 26 (47) 1 5322-15323

7. **Roberson L, Kowalik J, Tolbert L, Kloc Ch, Zeis R, Chi X, Wilkins C**
   Pentacene Disproportionation during Sublimation for Field-Effect Transistors *Journal of the American Chemical Society* 127 (9) 3069-3075; (Article)

8. **Takimiya K, Zeis R, Kloc Ch, Kunugi Y, Konda Y, Niihara N, Otsubo T**
   Evaluation of single crystal and thin film field-effect Transistor based on 2,6-Diphenybenzodichalcogenophenes in preparation

9. **Siegrist T, Kloc Ch, Zeis R, Schlockermann C, Chapman BD, Pindak R, Siddons DP, Checco A, Ocko BM**
   Topographic imaging of grain boundaries in single crystal rubrene in preparation

Contents

Chapter 1

Introduction

Over the past fifty years, no other semiconductor device has had such huge influence on technological progress as the field effect transistor. Its application has changed deeply the way of living in our modern society. Field effect transistors are the building block of today's communication and information technology. Therefore, today, the development of high-performance devices is a driving force in solid-state science. For decades, semiconductor science has been focusing mainly on silicon based devices. Silicon technology, however, requires photolithography and vacuum deposition, carried out under high temperatures in ultraclean rooms. Silicon chip production is therefore rather complex and only cost-effective due to the high quantities required. Because of this, alternative materials like organic semiconductors have gained special attention in recent years. Organic materials consisting of oligomers or conjugated polymers have some interesting advantages compared to their inorganic counterparts. They can be easily deposited over large flexible substrates by spin and dip coating techniques. Furthermore, simple electronic circuits (Fig.1.1) can even be printed by ink-jet printing solutions of some organic semiconductor. Additionally, the electrical properties of organic com-

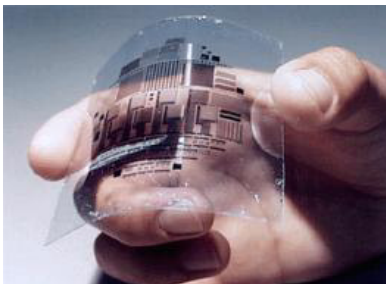

Figure 1.1: *A electronic circuit plotted by ink-jet printing*

pounds can be tuned by adding sidegroups or replacing individual elements in the molecules. Intensive effort has been put into the synthesis of new materials with improved performance and novel properties. For industrial device applications, the field effect transistor (FET) must fulfill certain requirements: e.g., a low threshold voltage so as to operate at low voltages, a high on/off ratio for obtaining a well-defined signal, and chemical stability. However, the most important requirement is carrier mobility, which defines the switching speed of the field effect transistor. In order to compete with the hydrogenated amorphous silicon thin film transistors (TFTs) that are widely used in today's flat-panel displays, the mobility of any newly designed organic FET should be above 1cm^2/Vs. The schema presented in Fig.1.2 compares the field effect mobilities for silicon based devices with the best polymer and oligomer TFTs. Despite the technological progress that has been made in

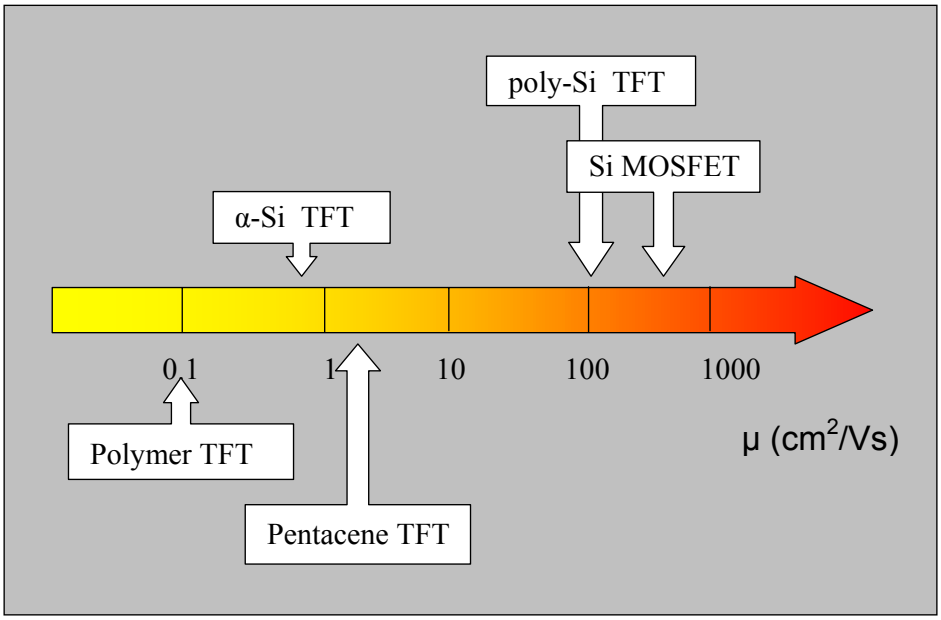

Figure 1.2: *The scale of the field effect mobilities in different types of field effect transistors based on organic and silicon solids*

recent years in developing organic thin film transistors, [Bao04] the electrical transport mechanisms in these devices are not yet well understood. Often, disorder and grain boundaries mask the intrinsic semiconductor properties in thin film transistors. To avoid grain boundaries and to limit the concentration of impurities and defects, single crystal field effect transistor are often employed. These are then model systems to study charge transport in ma-

terials and the relationship between molecular and crystal structure. I had the opportunity to perform much of my thesis research at Bell Laboratories, where material research is top-ranking. Therefore I had access to a broad spectrum of various types of materials.

- A big part of my thesis is dedicated to the materials **rubrene** and **pentacene**, due to their prominent position in the research of organic field effect transistors.
- **Substituted tetracenes** are prime examples of how device performance can be improved by adding functionalizing sidegroups.
- Another focus was on **copper phthalocyanine**, a material that is of special interest for technical applications because of its thermal and chemical stability.
- A different approach is mixing two organic compounds **TCNQ** and **Perylene** which leads to a class of material called charge-transfer salts.
- In cooperation with V. Podzorov (Rutgers University, USA), I worked on field effect transistors based on **layered transition metal dichalcogenide**. Their crystal structures are closely related to those of organic materials.

The materials I investigated were synthesized by H. Katz (Bell Laboratories, USA), Zh. Bao (Stanford University, USA), C. Nuckolls (Columbia University, USA) and K. Takimiya (Hiroshima University, Japan). At Bell Laboratories, Ch. Kloc and E. Bucher grow the crystals. T. Siegrist and C. Besnard performed the X-ray structure analysis.

Chapter 2

The field effect transistor

This chapter presents a short historical retrospective of the development of the first field effect transistor (FET) at Bell Laboratories, followed by a brief introduction to its operating mode. The second part of the chapter will focus on the basic characteristics of a field effect device.

2.1 The principle of a FET

Already in the early 1930s, the German scientist Julius Lilienfeld [Lil30] had an idea for making a solid state device out of semiconductors. He reasoned that a strong electrical field could cause the flow of electricity within a nearby semiconductor. He patented his idea for a field effect transistor, although he probably never had a working device. In 1945, William Shockley, at Bell Laboratories, [SP48] took over Lilienfeld's idea and also tried to build a field effect device, but it didn't work. Three years later, Walter Brattain and John

Figure 2.1: *The first point contact transistor*

Bardeen [BB48], also at Bell Laboratories, built the first working transistor, the germanium point-contact transistor, which was manufactured as the "A" series. A photo of this first transistor is presented in Fig. 2.1. Shockley then designed the junction (sandwich) transistor, which was manufactured for several years afterwards. But in 1960, based on Lilienfeld's original idea, Bell scientist John Atalla [KA60] developed the first metal insulator semiconductor field effect transistor (MISFET) using a thermally oxidized silicon structure. By the late 1960s, manufacturers converted from junction type integrated circuits to field effect devices. Today, most transistors are MOSFETs.

The MOSFETs can basically be considered as a parallel plate capacitor, where one electrode, the gate electrode, is electrically insulated, via an insulating oxide layer, from the semiconductor. Two electrodes, the source and

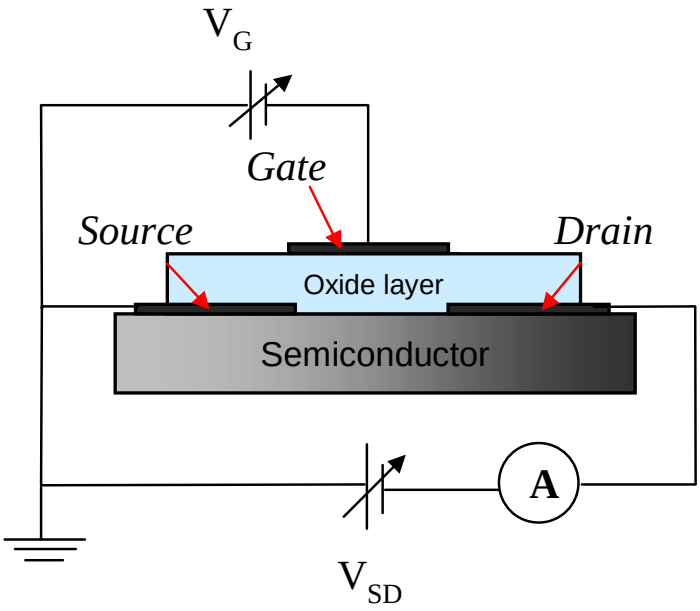

Figure 2.2: *The schematic representation of a MOSFET and the measuring circuit*

the drain, are in contact with the semiconductor. By applying a gate voltage, V_G, with respect to the source electrode, charge carriers can electrostatically be accumulated or depleted in the semiconductor at the semiconductor-insulator interface. Due to this field effect, the charge carrier density in the semiconductor can be varied. Therefore the resistivity of the semiconductor (upon application of a source-drain field) can be varied over orders of magnitude [SBB+97].

To demonstrate the different operating regimes of a p-type transistor, the band-bending diagrams of the metal-insulator-semiconductor diode are schematically given in Fig. 2.3. At equilibrium the Fermi levels of the materials align, by charge carries which move to or from the semiconductor-insulator interface. When a bias is applied which is equal to the difference between the Fermi level of the gate metal and the semiconductor, no band bending will occur in the semiconductor at the semiconductor-insulator interface. This biasing condition is defined as the flat-band voltage (Fig. 2.3a). For a p-type

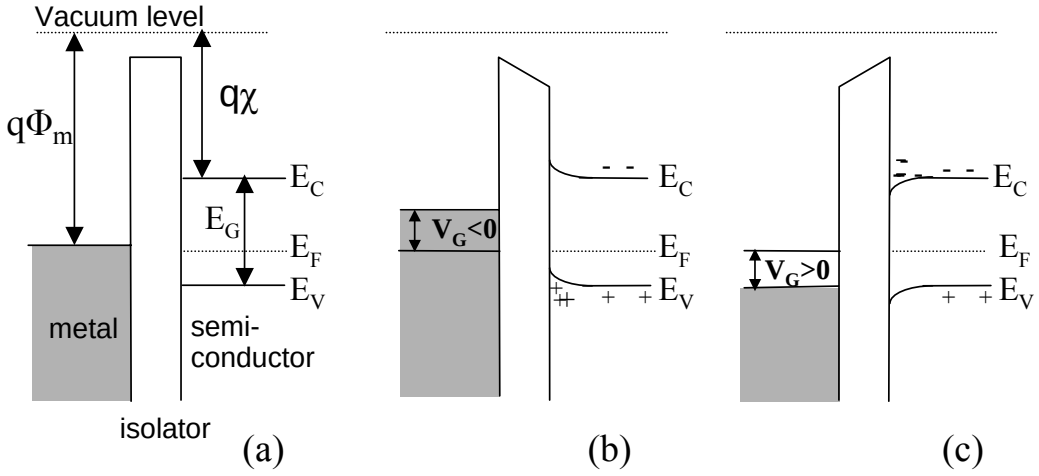

Figure 2.3: *Energy level band diagram of ideal metal-insulator-semiconductor diode structure with a p-type semiconductor: (a) flat-band condition, (b) accumulation, (c) depletion.*

semiconductor, the application of a negative gate voltage will induce charges at the semiconductor-insulator interface (these charges are supplied by the source and drain contacts). In effect the Fermi level of the gate metal is varied with a value of qV_G, causing band bending in the semiconductor layer as it is schematically presented in Fig. 2.3b. For a positive applied V_G the energy bands in the p-type semiconductor are bent downwards, and the mobile positive charge carriers are depleted from the semiconductor-insulator interface. In this case the transistor is biased in the depletion mode (Fig. 2.3c).

2.2 Basic characteristics of a FET

If a small source-drain voltage $V_{SD} <\mid V_G - V_T \mid$ is applied (V_T is the threshold voltage) the FET operates in the linear regime (Fig.2.4). In this regime the applied gate field is uniformly distributed along the conducting channel which results in a uniform charge distribution of the induced free charge carriers. Assuming a constant mobility, the channel current increases linearly with the additional charge induced in the channel δQ_{ind} due to a voltage increase at the gate contact $\delta Q_{ind} = C_i \delta V_G$. In the linear regime the channel current I_{SD} is given by [Sze85]

$$I_{SD} = \frac{W}{L} \cdot \mu C_i (V_G - V_T) \cdot V_{SD} \tag{2.1}$$

with W the channel width, L the channel length, μ the charge carrier mobility and C_i the gate insulator capacitance per unit area.

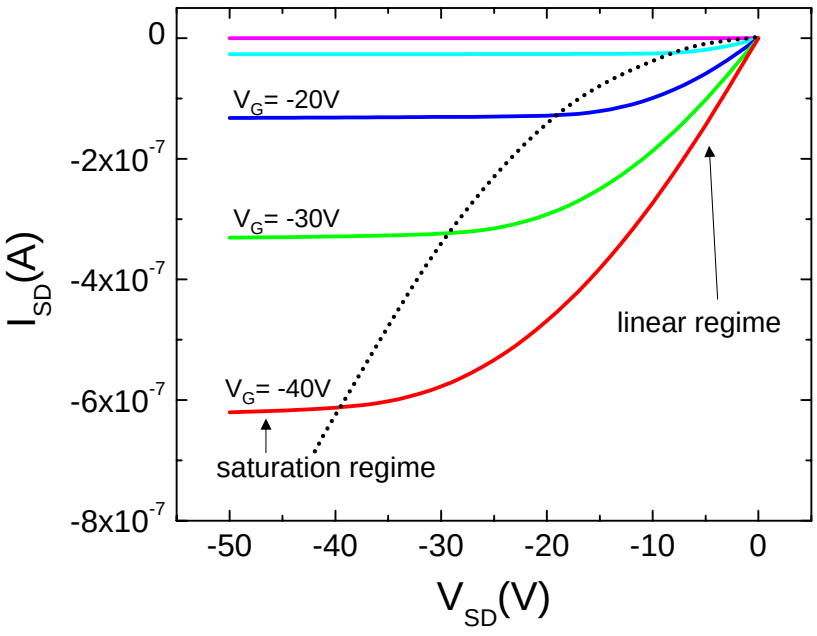

Figure 2.4: *The output characteristic of a pentacene single crystal device showing the saturation and the linear regimes of operation. The broken line indicates the border between these two regimes*

For a source-drain voltage $V_{SD} =\mid V_G - V_T \mid$ the gate field at the drain contact is zero. If the V_{SD} further increases, the area around the drain contact

becomes depleted with no induced free carriers. This phenomenon is called the pinch-off effect and beyond this point the channel current saturates. In this regime, the channel current is given by [Sze85]

$$I_{SD} = \frac{W}{2L} \cdot \mu C_i (V_G - V_T)^2 \tag{2.2}$$

Both the linear and the saturation regimes are indicated in the output characteristics (Fig.2.4) of a pentacene single crystal transistor. Note that in the saturation regime the channel current quadratically increases with the gate voltage in contrast to the linear regime.

The current in a MOSFET is transported predominantly by carriers of one polarity only (e.g., holes in a p-type device). Therefore, the MOSFET is usually referred to as a unipolar device. This is the case for all the organic single crystal devices I investigated. Specifically, the p-type conductivity has been observed, for instance, in anthracene, tetracene, pentacene, perylene, rubrene, whereas the n-type conductivity was observed in TCNQ and Perylene-TCNQ (see chapter 10). In principle, the unipolar operation can be explained by the choice of metallic contacts that are efficient injectors of only one type of carrier. To realize an ambipolar transistor, which can operate as either an n-type and p-type transistor, holes and electrons have to be injected from the same electrode. The main difficulty therefore is that a good contact for one charge polarity typically results in an injection barrier for the other polarity. However, this injection barrier can be reduced by using a material with a smaller energy gap. Furthermore, the width of an injection barrier can be narrowed by applying a large source and drain field, or by the accumulation of high charge carrier densities in the channel by means of the field-effect [Sze85]. For sufficiently high amounts of accumulated charge, the injection barrier becomes small enough to allow tunnelling from the electrode into the semiconductor. Besides the small band gap of the semiconductor, the purity of the crystal material also plays an important role in minimizing trapping effects. Only WSe_2 (see chapter 12) fulfills these requirements and ambipolar operation has been observed.

To evaluate the device performance, the main characteristics, including the charge carrier mobility (μ), the field-effect threshold (V_T), and the subthreshold slope (S), were taken from the conventional MOSFET theory. They are summarized below.

2.2.1 Field-effect threshold

The threshold voltage V_T is a measure of the amount of charge that must be electrostatically induced in order to switch on the electrical conduction in

a FET. It can be obtained in two ways, the first by applying the equation 2.1 that describes FET operation in the linear regime. In this case, the quasilinear (high- V_G) part of the transconductance characteristic $I_{SD}(V_G)$ presented in Fig.2.2.1 has to be extrapolated to zero current.

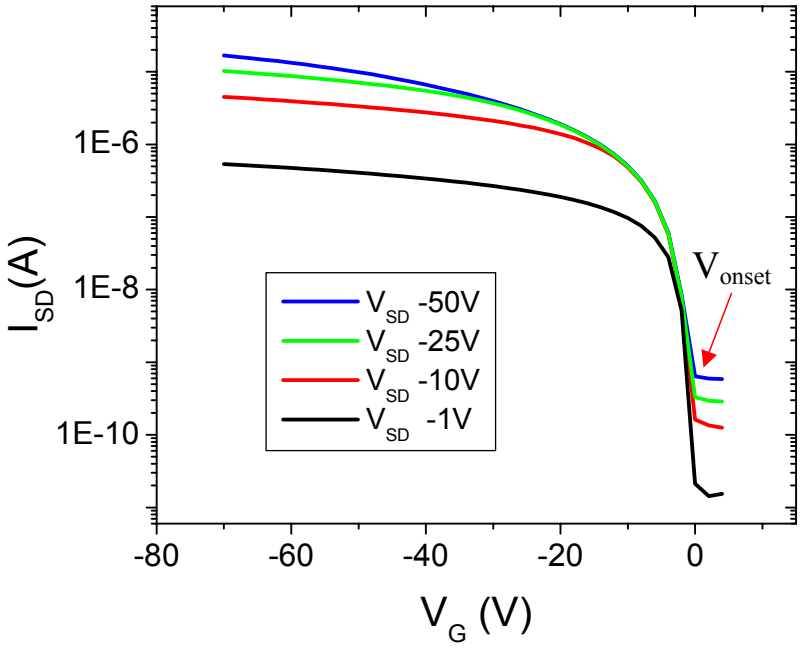

Figure 2.5: *The trans-conductance characteristics of an OFET fabricated on a rubrene single crystal, measured at different values of the source-drain voltage V_{SD}. The arrow marks the field-effect onset V_{onset}.*

It is also possible to extract the threshold voltage from the square root of the saturation current I_{SD} plotted against the gate voltages V_G. This curve, presented in Fig.2.6, is fit linearly and the intercept on the V_G-axis is defined as the V_T of the transistor.

The magnitude of the field-effect threshold voltage depends on several factors, such as the density of charge traps on the interface between the organic crystal and the gate dielectric, the quality of the source/drain contacts, and the absence/presence of a built-in conduction channel. In the case of FETs with parylene as dielectric material, the built-in channel is absent. This means that for a p-type/n-type device the field-effect onset V_{onset} is observed at a negative/positive gate voltage (Fig.2.2.1). Therefore, the upper limit of the density of the charge traps n at the semiconducter/parylene interface

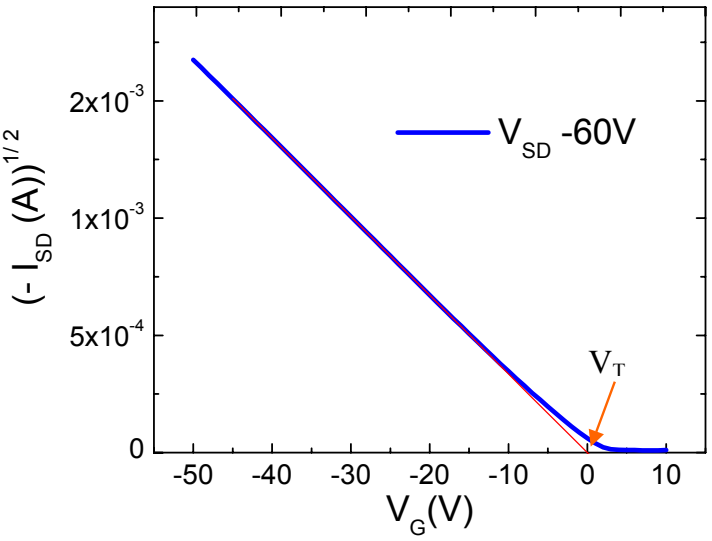

Figure 2.6: *Plot of the square root of source-drain current in the saturation regime as a function of the gate voltages for a pentacene device. The red line intercepts the V_G-axis at the threshold voltage. From the slope of the red line the field-effect mobility can be derived.*

can roughly be determined by applying equation [Hor98]

$$n \approx \frac{V_T \cdot C_i}{q} \tag{2.3}$$

The charge induced by the gate field in the sub-threshold regime fills the traps that immobilize the charge carriers.

2.2.2 Sub-threshold slope

The sharpness of the field-effect onset is characterized by the sub-threshold slope

$$S = \frac{\partial V_G}{\partial(\log I_{SD})} \tag{2.4}$$

Since this quantity depends on the capacitance of the insulating layer C_i, it is also convenient to introduce the normalized slope, $S_i = S \cdot C_i$, which permits a more direct comparison of the properties of different devices [PPG03]. Usually, the normalized sub-threshold slopes of pentacene thin film transistors

($S_i = 15 - 80V \cdot nF/decade \cdot cm^2$) [DKP+99, DPK+99, LGNJ97] are referred to as a standard of comparison. However, for single crystal devices, a smaller value of S_i can be achieved. So far, pentacene ($S_i = 3V \cdot nF/decade \cdot cm^2$)(see chapter 6) and rubrene ($1.7V \cdot nF/decade \cdot cm^2$) [PSL+03] single crystal FETs exhibit the sharpest field-effect onset.

It is commonly believed that the sub-threshold slope is mainly determined by the quality of the insulator/semiconductor interface [Sze85]. This is definitely the case for Si MOSFETs, where the resistance of source and drain contacts is low and does not depend on the gate voltage. In contrast, the contact resistance in the OFETs (Schottky-type FETs) is high; it depends non-linearly on V_G as the result. The subthreshold slope also reflects the quality of contacts (see also chapter 9).

2.2.3 Field-effect mobility

Starting from the trans-conductance characteristics, the mobility of carriers μ at the surface of single crystals can be estimated in the linear regime of the device operation by applying Eq. 2.5 [Sze85].

$$\mu = \frac{L}{W \cdot C_i \cdot V_{SD}} \cdot (\frac{\partial I_{SD}}{\partial V_G}) \tag{2.5}$$

There, the conductivity of the channel ($\sigma = en\mu$) varies linearly with the density of mobile field-induced charges n. This definition of μ assumes that all charge carriers with the density

$$n = \frac{C_i \cdot (V_G - V_T)}{e} \tag{2.6}$$

induced by the transverse electric field above the threshold, are mobile. For rubrene single crystal devices, this assumption can be justified, because only a very weak dependence $\mu(V_G)$ is observed. However, the mobilities in other organic devices and amorphous silicon (α-Si:H) FETs [SHS89] are strongly V_G-dependent. In these cases, most of the charge above the field-effect threshold is induced into the in-gap localized states and only a small fraction is induced into the conduction band. For this reason, the calculated value of the mobility, using Eq. 2.5, is underestimated.

Additionally, the field-effect mobility μ can also be derived from the gate voltage dependence of the saturation current by applying Eq. 2.2. The plot of the square root of I_{SD} versus the V_G leads to a straight line (Fig.2.6).

$$\mu = \frac{2L}{C_i \cdot W} \cdot (\frac{\partial \sqrt{I_{SD}}}{\partial V_G})^2 \tag{2.7}$$

As shown by Eq.2.7, the mobility increases quadratically with the slope of this line.

For the different crystal materials that have been investigated the mobility of the field-induced carriers varies over a wide range (see chapter 11). Distinguished are rubrene and WSe_2 with a hole mobility of 13 cm^2/Vs and 475 cm^2/Vs measured at room temperature.

Chapter 3

The crystal material

The field effect geometry allows me to investigate the transport properties of various organic as well as inorganic single crystals. To investigate the charge transport in these crystal materials, different models are introduced.

3.1 Charge transport in organic single crystals

Molecular crystals are composed of discrete molecules held together by weak van der Waals forces and the molecules themselves consist of atoms held together by covalent bonds. For this reason, the crystals are quite brittle, exhibit low melting points and often show poor electrical conductivity. Because of the weak nature of the bonding between molecules in a molecular solid, it is to be expected that the properties of the individual molecule are retained in the solid state to a far greater extend than would be found in solids exhibiting other types of bonding. It is therefore important to understand the properties of atomic carbon itself and the intramolecular bonding mechanisms of hydrocarbons [PS82].

Carbon, in the ground state, has four electrons in the outer electronic level. The orbitals of these electron may mix under the creation of four equivalent degenerate orbitals, referred to as sp^3 hybrid orbitals in a tetrahedral orientation around the carbon atom. Methane exemplifies this type of bond. If only three chemical bonds are formed, they have three coplanar sp^2 hybridized orbitals which are at an angle of 120° apart from each other. These bonds are called σ-bonds, and are associated with a highly localized electron density in the plane of the molecule. The one remaining free electron per carbon atom resides in the p_z orbital, perpendicular to the plane of the sp^2. The p_z on the neighboring atoms overlap to form so called π-bonds.

A schematic representation of this hybridization is given in Fig. 3.1 for the double-bonded carbon structure of ethylene (C_2H_4).

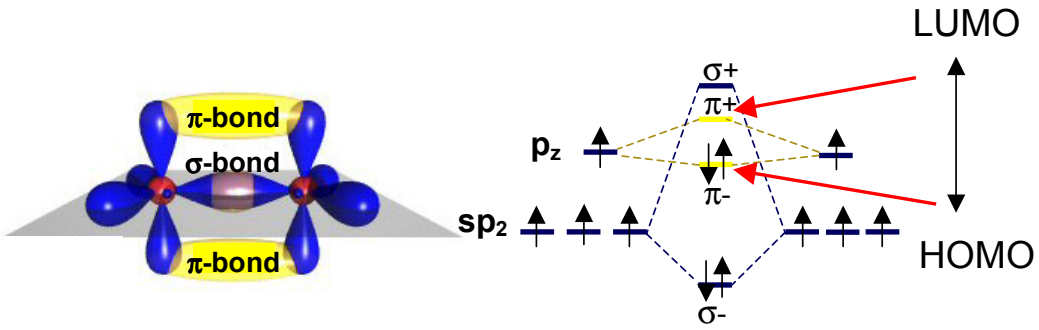

Figure 3.1: *Molecular orbitals of ethylene (C_2H_4). The p_z atomic orbitals of the C atoms overlap to form the bonding molecular π-orbital that define the HOMO and LUMO level in the Molecule.*

This kind of hybridization is also found in conjugated aromatic hydrocarbons like tetracene and pentacene. The term conjugated refers to the alternating sequence of single and double bonds in the molecule. The term aromatic derives from the characteristic odor these compounds release. The general formula for aromatic hydrocarbons or acenes is $C_{4n+2}H_{2n+4}$ where n is the number of rings in the molecule. These molecules are generally flat and there are (4n+2) π- electrons per molecule, one from each carbon atom. As shown in Fig.3.2 the π-electrons establish a delocalized cloud above and below the plane of the molecule. The general chemical stability of these molecules decreases as n increases. For instance, pentacene decomposes at high temperature in the presence of light and air (see chapter 6), whereas tetracene and anthacene are more stable [PS82].

The highest occupied orbitals (HOMOs) and the lowest unoccupied orbitals (LUMOs) are both π-orbitals (Fig.3.1). Therefore, these delocalized π-electrons are largely responsible for the opto-electronic behavior of the organic crystal.

Electronically each organic molecule in a crystal can be seen as an entity of its own. Although, the π-electrons are completely delocalized and mobile along the conjugated carbon atoms in each molecule, an injected excess charge carrier (electron or hole) cannot easily proceed from molecule to molecule in the crystal because the overlap of the adjacent molecule is small. There are two different theoretical models to explain the charge carrier pro-

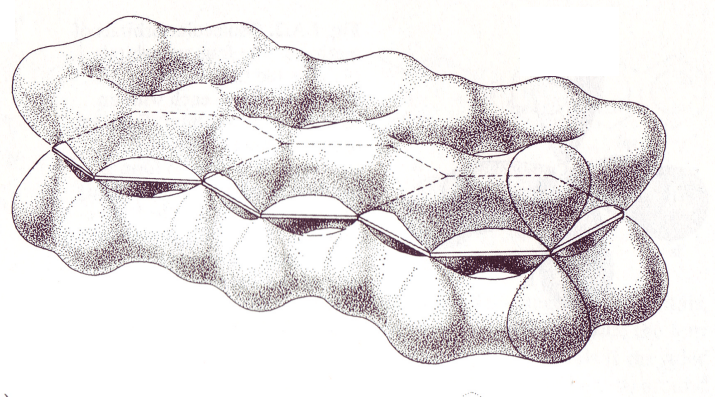

Figure 3.2: *Schematic view of the lowest bonding orbital of the anthracene molecule; for clarity, hydrogen atoms are not shown. The figure is taken from ref.[PS82].*

cess in molecular crystals. One is based on the band model, which is usually used to describe the charge transport in inorganic semiconductors; the other is based on the idea of localized carriers that hop from one molecule to the next.

3.1.1 Band and hopping transport

The high mobility found in conventional inorganic semiconductors like Ge rests in the fact that charges in crystalline materials move freely in delocalized bands. These bands result from the coalescing of discrete levels; when a large number of atoms are gathered together in a three dimensional lattice, the discrete atomic levels widen into bands [Hor99]. In these wide bands, the mobility depends on the temperature with

$$\mu \propto T^{-n} \tag{3.1}$$

where $n > 1$ [PS82]. In contrast, the lower mobility found in organic semiconductors is because the molecular levels, which become the building blocks for organic crystals, do not interact with each other so easily. Therefore, the charges are strongly localized and move by hopping from site to site, being scattered at virtually every step. For localized charges the temperature dependence goes as

$$\mu \propto \exp^{-E_a/k_B T} \tag{3.2}$$

where E_a is an activation energy. Molecular crystals like rubrene fall in a intermediate category of these two transport mechanisms, the temperature dependence shows evidence of band and hopping motion as well.

Localization of the states in organic crystals may have various reasons. The cohesion between individual units is ensured by weak van der Waals forces rather than strong covalent bonding. Additionally, conjugated molecules tend to change their geometry upon charging, which means they show a strong electron-phonon coupling. The association of the charge with lattice deformation is termed polaron. When the charge moves in the solid, the associated formation follows like a shadow. In other words a polaron is a self-localized charge. Another source of charge localization is disorder due to crystal defects, such as vacancies, delocalization and grain boundaries.

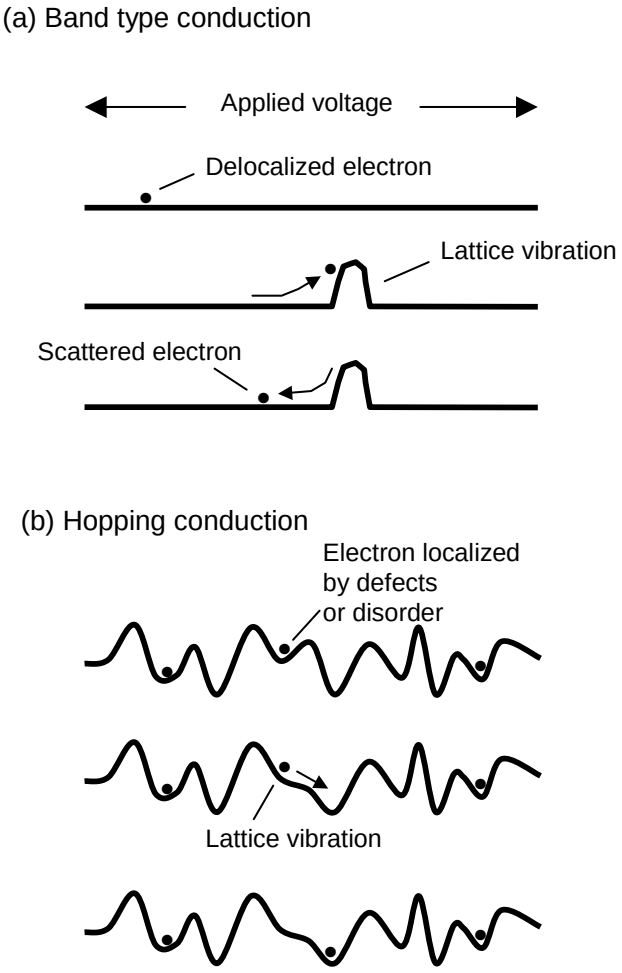

Figure 3.3: *Transport mechanisms in solids. (a) Band transport. In a perfect crystal, depicted as the straight line, a free carrier is delocalized, and it moves as a plane wave without scattering. In a real crystal, there are always lattice vibrations or phonons that disrupt the crystal symmetry. These phonons scatter the electron and thereby reduce its mobility. Lowering the temperature will therefore increase the mobility. (b) Hopping transport. If the carrier is localized due to defects, disorder or selflocalization, e.g. in the case of polarons, the lattice vibrations are essential for a carrier to move from one site to another. For hopping transport the mobility increases with increasing temperature. The figure is adapted from ref. [PS82]*

3.1.2 The concept of polaron hopping

As already mentioned above, the quasiparticle polaron results from the coupling of charge with the deformation of the lattice associated with the charge. The polaron is termed "small" when the deformation region is comparable to the size of the molecule. The theory of small polaron transport was already developed in the late fifties by Yamashita and Kurosawa [YK58], and Holstein [Hol59]. In this theory, Holstein used a used a Hamiltonien composed of three terms, one that accounts for the lattice, the second for the electron and the last one for the electron phonon coupling. The lattice component consists of a sum of harmonic oscillators that vibrate at a frequency ω_o. The dominant parameter of the electron component is J, the so-called electron transfer, or overlap integral. The magnitude of the electron-phonon coupling can be quantified through the so-called polaron binding energy E_b, which corresponds to the energy gain due to the polarisation and deformation of the lattice. The small polaron limit corresponds to strong coupling, where $E_b \gg J$, in which case the electronic term can be treated as a perturbation. Polaron motion takes place via a succession of random jumps, in each of which the electron hops to the neighbor site. Later, the concept of polaron hopping was improved by Emin [Emi85]. He introduced the concept of coincidence, where site jumps occur when the energy state of the second site coincidences with the first one. Such a coincidence is achieved by thermal deformation of the lattice. Emin [EH69] also made a distinction between adiabatic and non-adiabatic processes. In the former, the lifetime of the coincidence is much larger than the electron transit time, in which case the electron has time to follow the lattice deformations. In the high temperature limit, the mobility of the adiabatic small polaron is given by Eq.3.3.

$$\mu = \frac{\omega_o q \delta^2}{2\pi k_B T} \cdot \exp(-\frac{E_b}{k_B T}) \tag{3.3}$$

Here δ stands for the mean intermolecular distance. At low temperatures, the variation of the mobility is found to deviate from the thermally activated law [Hor99].

3.1.3 Multiple trapping and release model

The temperature dependent transport data for organic single crystals can also be interpreted in terms of a multiple trapping and release model. In fact, this model has been developed to account for the charge transport in amorphous silicon[LS70], where the carrier mobility is significantly lower than for single crystals. This comes from localized levels (traps) in the energy gap, due to

defects like dangling bounds in the amorphous material. However, the model can also be applied [PMB+04] to explain the thermally activated and gate bias dependent behavior of field-effect mobility in an organic single crystal.

The model is based on a mechanism in which carriers moving in the extended level are trapped by the localized defects. The charges can eventually be thermally released again and contribute to charge transport. As the release mechanism is thermally activated, this results in a thermally activated mobility. In the simplest case where there is a single trap level, the activation energy corresponds to the distance between the trap level and the edge of the extended transport band [Hor99]. A large concentration of localized states in the forbidden gap can also explain the gate voltage dependence of the mobility. At low gate voltage, most of the charges are trapped by these states, thus leading to low mobility. As the gate voltage increases, the Fermi level moves toward the extended band edge and more traps are filled. Eventually, all traps will be filled and any additional injected charge will be free to move in the extended states with a mobility independent of the gate bias. This principle is displayed in Fig. 3.4.

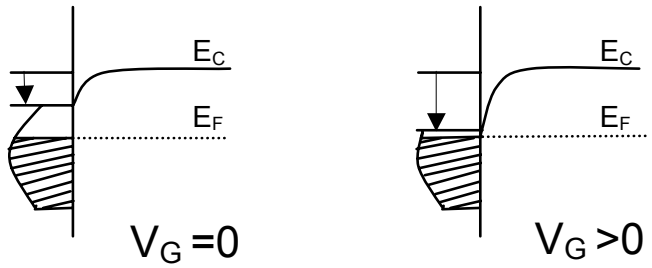

Figure 3.4: *Principle of the trap limited mobility. Left, at zero gate voltage, the Fermi level is located within the trap distribution, and mobility is limited by traps. Right, when a gate bias is applied, the traps are filled and charges are injected above the mobility edge, where their mobility is enhanced. The figure is taken from ref.[GHRH99].*

3.1.4 Structure of organic single crystals

The probability of the hopping process in the crystal material is correlated to the size of the π-overlap integral, which is defined by the relative arrangement of the molecules in the crystal. Therefore, the crystal structure plays a key role for the charge transport.

The strong interactions between the atoms determine the packing in covalent and ionic crystals. In covalent crystals, the electronic distribution will be localized in preferred directions, due to the fact that electron pairs are shared between the atoms. An example therefore is diamond, where all four electrons in the outer electronic level of carbon participate and form covalent bonds, building tetrahedrons with fixed angles. The ions in ionic crystals can be approximated as charged spheres, which are bonded by electrostatic interactions. Because of the spherical nature of the atoms and the relatively strong interactions between them, the crystal structure can be seen as formed by closed packing of anions (cations) with the cations (anions) filling the tetrahedral and octahedral holes.

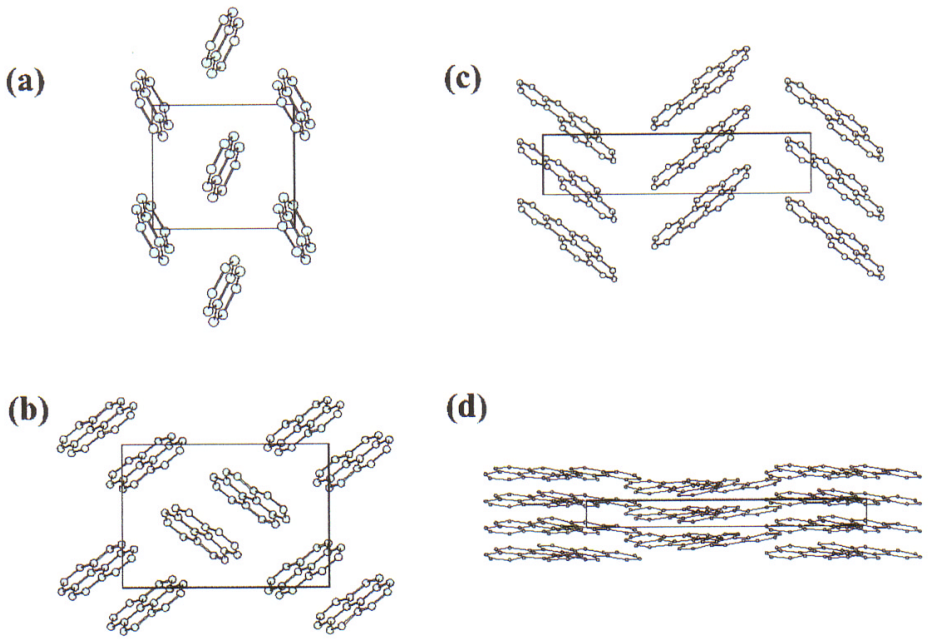

Figure 3.5: *The four different crystal packings observed for aromatic hydrocarbon. (a) Naphthalene, an example of herringbone structure (b) Pyrene, crystalized in a sandwiched herringbone structure (c) Benzopyrene, an example of a γ structure (d) Violanthrene, crystalized in a β structure. The schema is taken from ref. [Mat02].*

For organic molecular crystals the situation is different. Because of the weak interactions between the molecules and the complicated shape of the molecules, it is hard to predict the structure in which the molecules will crystalize. However, the packing of many organic molecular crystals can be

classified into some general structure types. Based on a study that Gavezzotti et al. [GD88] performed on planar aromatic hydrocarbons, four basic structural types were defined. These four crystal types are shown in Fig. 3.5. All of these crystal types are built in a layered structure, but the structure in the layers varies from type to type. Naphthalene is a prime example of a herringbone structure. In addition to naphthalene, anthracene and tetracene were also found to crystalize in this particular structure. In the second type two parallel oriented molecules together form a herringbone structure. This crystal arrangement is called sandwiched herringbone structure. The third structure type is characterized by a shorter axis length, therefore the herringbone pattern is flattened in one direction. This is even more the case for the final type, the β-structure, which is closely related to the graphite structure and the crystal structures of layered transition metal dichalcogenides. In his attempt to link the the geometrical properties of the molecule with the crystal structure Gavezotti et al. found some general trends. Disk-shaped molecules tend to crystallize into β structures, because the C-C interactions promote parallel stacking whereas elongated molecules with H-atoms on the rim prefer herringbone stacking. However, a given substance may crystallize in various structures: especially for copper phthalocyanine [MT83] and pentacene [Mat02] many polymorphisms are known.

3.2 Transition metal dichalcogenides

The transition metal dichalcogenides (TMDs) belong to the class of layered inorganic semiconductors with a chemical formula MX_2, where M stands for a transition metal and X - for Se, S or Te [Lie77, Buc92]. Single crystals of TMDs are formed by stacks of X-M-X layers (Fig. 3.6). Atoms within each layer are held together by strong covalent-ionic mixed bonds, whereas the layers are weakly bonded to each other by van der Waals forces. The bonding anisotropy defines the unique morphology of single crystals of these compounds as thin, flexible and easy-to-cleave platelets with atomically smooth (a,b)-facets. The electronic properties of TMDs vary from semiconducting (e.g. WSe_2) to superconducting (e.g. $NbSe_2$) [Lie77, Buc92]. The semiconducting members of this class are considered to be promising materials for solar cells, photoelectrochemical cells and p-n-junctions [SELS$^+$83, SLSO$^+$85, TW85]. Similarly to graphite, the layered TMDs can form nanostructures, such as fullerene-like nanoparticles [TMGH92], nanocrystals [ZLH$^+$96] and nanotubes [Rem01]. Because of the outstanding chemical inertness and unique shapes of these nanostructures, they may have numerous potential applications ranging from solid lubricants [Rap97] to the tips in scanning

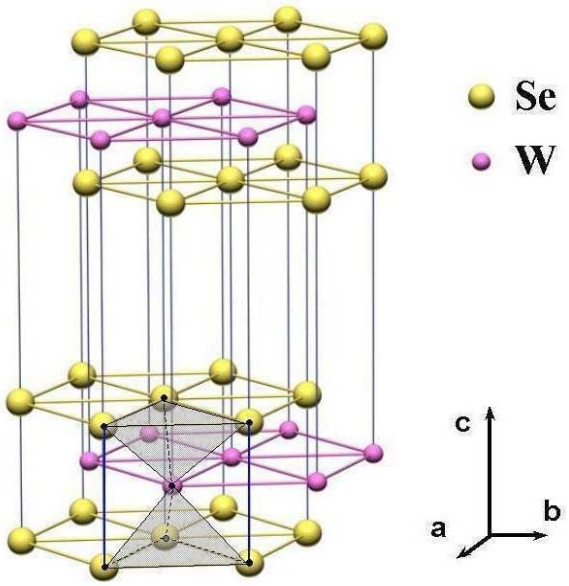

Figure 3.6: *Layered structure of tungsten diselenide WSe_2. Each layer consists of covalently/ionically bonded atoms of W (magenta) and Se (yellow) that form trigonal prisms with the W atom at the center; the adjacent layers are bound together in the c-direction by weak van der Waals forces*

probe microscopes [TZ01].

As pointed out in the previous section, the structures of layered TMDs and organic materials show some similarities. For both types of materials, the surface is van der Waals determined. This makes them in principal well suited for the field-effect experiments. Owing to the weak van der Waals bonding, the surface is characterized by an intrinsically low density of dangling bonds that can act as the charge traps. Additionally, once found, a proper device technique to handle organic single crystals can also be applied to TMDs single crystal.

Chapter 4

Device fabrication

In this chapter, I will outline the individual steps to fabricate a field effect transistor. After a presentation of the crystal growth for organic materials and transition metal dichalcogenides, I will focus on the difficulties of gently depositing electrodes and a dielectric layer for a ready device.

4.1 Crystal growth

4.1.1 Organic material

Most of the single crystals used for the fabrication of organic FETs have been grown by horizontal physical vapor transport in a flow of argon or hydrogen [KSSL97, LKSS98]. The schematic set-up is shown in figure 4.1.

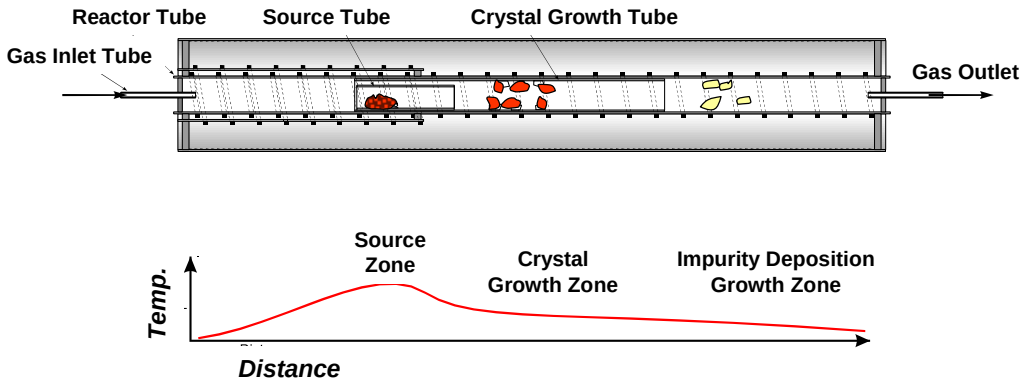

Figure 4.1: *Schematic of the growth apparatus. The temperature profile across the furnace is shown in the bottom part of the figure.*

The crystals are grown in a horizontal two-zone furnace. The starting material volatilizes and is carried away from the source zone by a stream of gas. In the growth zone crystals nucleate and grow free-standing, stress-free into the quartz tube. In addition, the growth technique is a very efficient purification technique. More volatile impurities will condense in the impurity deposition zone, and less volatile impurities will remain in the source zone. The evaporating material is heated to typically around 300°C in the first zone of a two-zone furnace. The second zone of the furnace is held at approximately 200°. Of course, the temperature of the furnace has to be adjusted for each substance individually. For instance, copper phthalocyanine has a lower vapor pressure [YTAKK95] than rubrene [BGMP04]; therefore a higher source temperature is required for its growth. Heating is applied by a resistance wire and using thermocouples the temperature can be checked and stabilized. The horizontal setting is used for experimental convenience. The advantage of this geometry is that the starting material can be inserted easily and both the residual starting material and the crystals can be removed easily after growth.

Nearly all organic crystals grown by the physical vapor transport are shaped as elongated "needles" or thin platelets. A couple of prominent examples of organic single crystals are presented in Fig. 4.2. The dimension

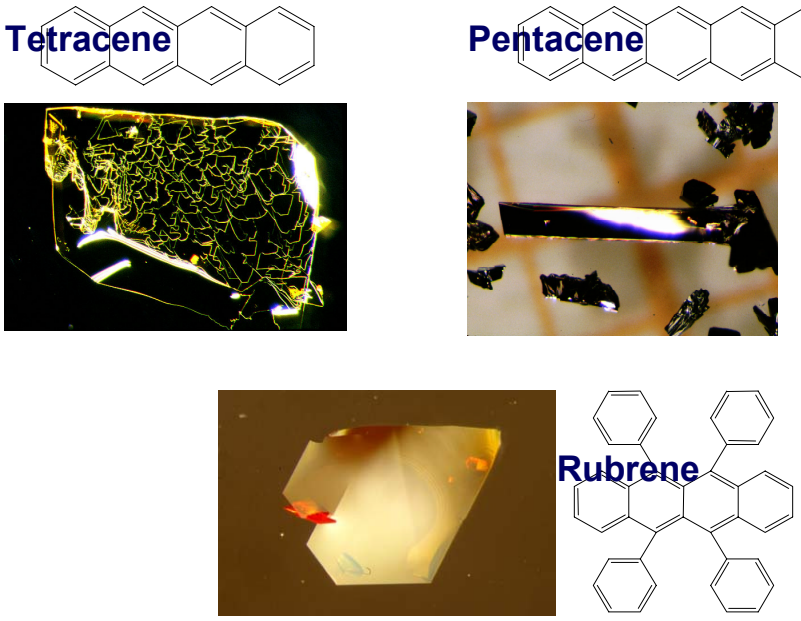

Figure 4.2: *Organic single crystals grown by physical vapor transport*

of the crystals can range from several millimeters to several centimeters in width and length. The crystal thickness also varies between 10 and 400μm.

Many authors [JBP04, BGMP04, BLR04] claim that to achieve a high field effect mobility, the starting material must be pre-purified using several re-growth cycles. This conclusion is different from my experience. Impurities that can act as traps for charge carriers and therefore reduce the field effect mobility exist not only as byproducts in the commercial powder, they are also formed during the growth process. Photo-induced reactions with O_2 and the formation of other disproportionation products are known for most organic molecules [JBP04, RKT$^+$]. Consequently, using multiple sublimations, especially for growth processes performed in the light and at high temperatures, might lead to increased impurities and could seriously deteriorate the desired electronic transport properties of the crystals.

In some experiments (see chapters 5 and 6), I used crystals which were grown in a sealed ampoule. Therefore, previously sublimed crystals, grown in a flow of inert gas, were further used for typical vacuum-sealed ampoule growth. This last procedure resulted in crystals growing in smaller temperature gradients close to thermodynamic equilibrium and produced thicker crystals.

4.1.2 Transition metal dichalcogenides

The single transition metal dichalcogenide crystals are grown from polycrystalline material, which is synthesized from powder or pellets of the individual elements (Fig. 4.3). Therefore, the elements are mixed, filled in a quartz

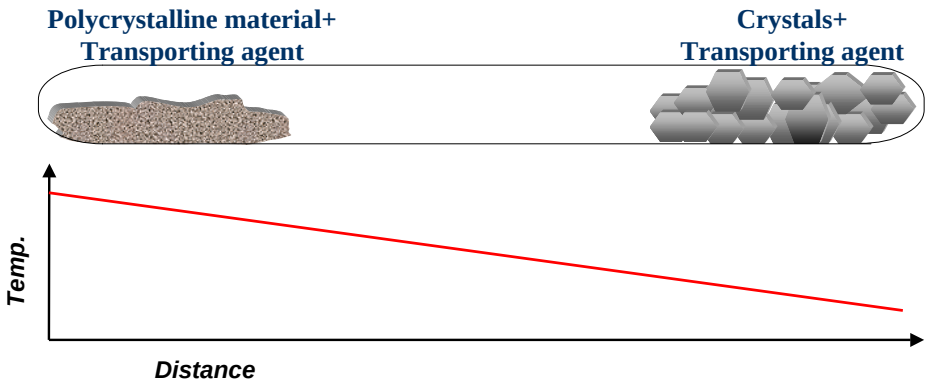

Figure 4.3: *Schematic of the vapor phase transport method. The temperature profile across the furnace is shown in the bottom part of the figure.*

tube and sealed under vacuum to remove oxygen as a reactant. To facilitate the sealing of the tube, inert helium gas is introduced into the tube. The tube is sealed using a hydrogen-oxygen torch. To make sure that a reaction occurs, the ampoules are kept at high temperatures (below 600°C) for several days. In the next step the crystals are grown by vapor phase transport. Here, the polycrystalline material plus the transporting agent like I_2, Se and S are inserted at one end of a silica tube and sealed. Then, the ampoule is placed in a two zone furnace and kept in a temperature gradient going from around 900°C to 1000°C. The schematic of the vapor phase transport method (VPT) is displayed in Fig. 4.3. Within several weeks, up to 300 μm thick and 1-2 cm^2 large platelets are formed. Some results of these crystal growth processes are shown in Fig. 4.4.

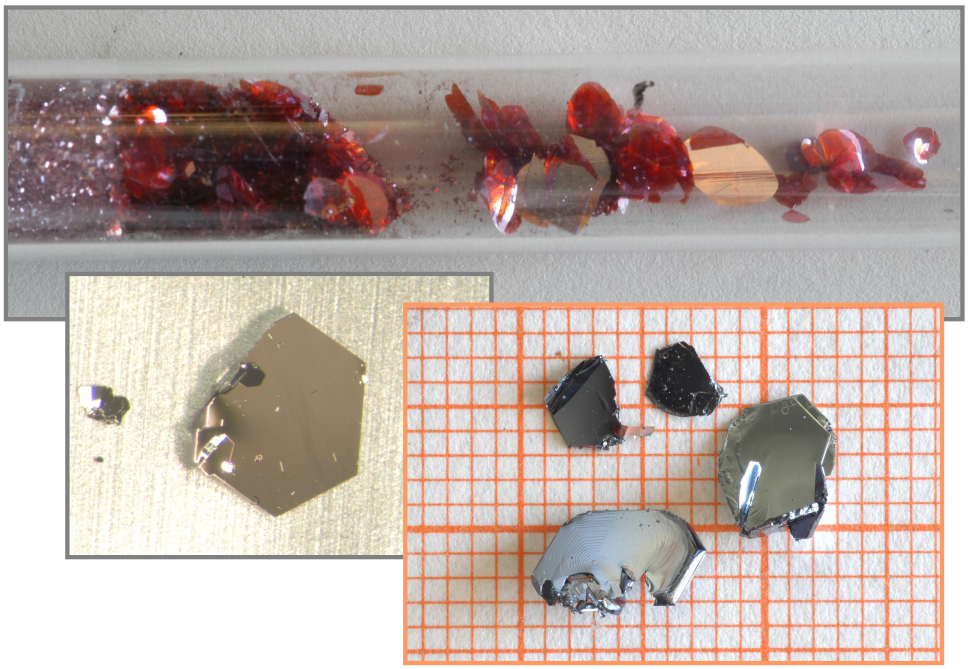

Figure 4.4: *An ampoule after the crystal growth process: HfS_2 single crystals and some remaining polycrystalline material. In the bottom part of the figure, single crystals of WSe_2 (left) and HfS_2 (right) are presented.*

The best quality transition metal selenide and sulfide crystals are achieved by using excess Se and S respectively as a transporting agent. This is because a transporting agent like I_2 tends to contaminate the single crystals [Spa86].

4.2 Fabrication of the FET structures

Fabrication of the field effect structure on the surface of van-der-Waals-bonded crystals poses a challenge, because many conventional fabrication processes cause irreversible damage to the surface of the crystals by disrupting the molecular order, generating interfacial trapping sites, and creating barriers to charge injection. For example, sputtering of an insulator like Al_2O_3 onto a crystal creates such a high density of defects on the surface that the field-effect is completely suppressed. As shown in Fig. 4.5 the surface is damaged, probably by high energy particles in the plasma.

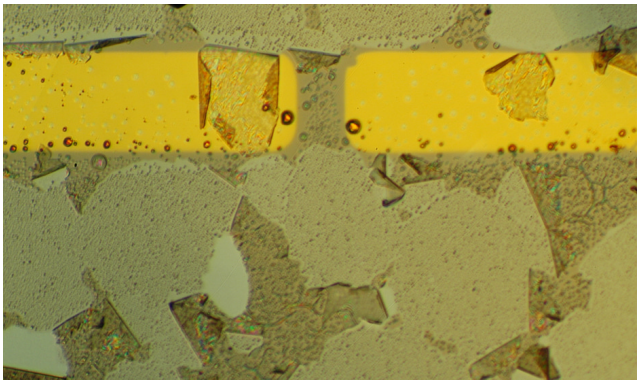

Figure 4.5: *Surface of WSe_2 single crystal with evaporated Au source and drain contacts after the sputtering of Al_2O_3*

A critical procedure when creating an organic single crystal FET is also to evaporate the metal source- and drain-contacts through a shadow mask. This is necessary because the thermal load on the crystal surface in the deposition process generates traps at the metal/organic interface that result in a poor FET performance. Despite this, I used a liquid nitrogen cooling system to maintain the crystal temperature at room temperature, kept the deposition rate at a low level ($1\mathring{A}$/s) and chose a large distance (50 cm) between the evaporation source and the sample holder in order to minimize damage of the crystal surface. The highest carrier mobility I obtained for a rubrene single crystal device with evaporated silver contacts was O.7 cm^2/Vs. This value is one order of magnitude lower than what I normally achieve for a rubrene single crystal FETs (see chapter 5). I had more success when I used a water based solution of colloidal carbon as a contact material, which provided a low contact resistance to organic crystals. It is still not understood why painted

graphite contacts act so well for the charge injection in organic FETs. Several attempts to create a home-made conducting paste based on gold powder with properties similar to the purchased carbon paint failed even though gold has the same work-function as graphite (4.8 eV). A disadvantage of this method is that it is often painstakingly difficult to prepare small and nicely-shaped contacts on the hydrophobic surfaces of the organic crystals.

In the future, it would be useful to better understand the mechanism of damaging of organic crystals in the process of contact fabrication in order to make the preparation of high-quality contacts routinely possible with many different metals. In particular, preparation of high quality contacts will help to elucidate the role of the work function of the metallic electrodes, which seems to play a less prominent role than was initially expected [VFO$^+$04, BGMP04].

Concerning this matter, transition metal dichalcogenides are more robust. In general, the thermal deposition of metals on the crystal surface is trouble-free; it is even possible to sputter the contacts. Occasionally, I observed instead of homogenous metal overlayers the formation of three-dimensional metal clusters, because the interaction between the surface of van-der-Waals-bonded crystal and adsorbed metals is weak.

After many attempts, it became clear that sputtering of Al_2O_3, as well as other dielectrics like SiO_2 and Teflon on the surface of the crystals will not lead to a working device. An experience which I share with all research groups active in this field. So for a long time, finding a suitable gate dielectric material and therefore the right technique, was the limiting step in the device fabrication. The breakthrough came with using thin polymer films of parylene as a gate dielectric material [DFG$^+$98, PPG03]. Parylene was developed over thirty years ago primarily to provide a protective coating for printed circuit boards. Today, it is also used for medical coating applications. This material with a dielectric constant $\epsilon = 2.65$ forms transparent pinhole-free conformal coatings with excellent mechanical and dielectric properties: the breakdown electric field can be as high as $\sim$10 MV/cm for the thickness 0.1μm.

The parylene coating process consists of three distinct steps as outlined in Fig. 4.6, which were performed in a home-built reactor. The first step is vaporization of the solid dimer at approximately 150° C. The second step is the pyrolysis of the dimer at the two methylene-methylene bonds at about 680° C to yield the stable monomeric diradical, para-xylylene. Finally, the monomer polymerizes in the deposition zone (the sample location) at room temperature and pressure $\sim$0.1 Torr. The samples are positioned approximately 35 cm away from the pyrolysis zone of the parylene reactor. This process is particulary gentle for the crystal surface, because the substrate temperature

never rises more than a few degrees above ambient and since parylene is chemically inert it does not react with crystal material. A necessary fourth component in this system is the mechanical vacuum pump and associated protective traps. It is important to mention that parylene was deposited onto the crystals with prefabricated source and drain contacts with wires already attached, otherwise connecting the contact pads might be difficult. This is simply because parylene uniformly covers the hole sample and the sample holder. The thickness of the parylene layers was determined with a

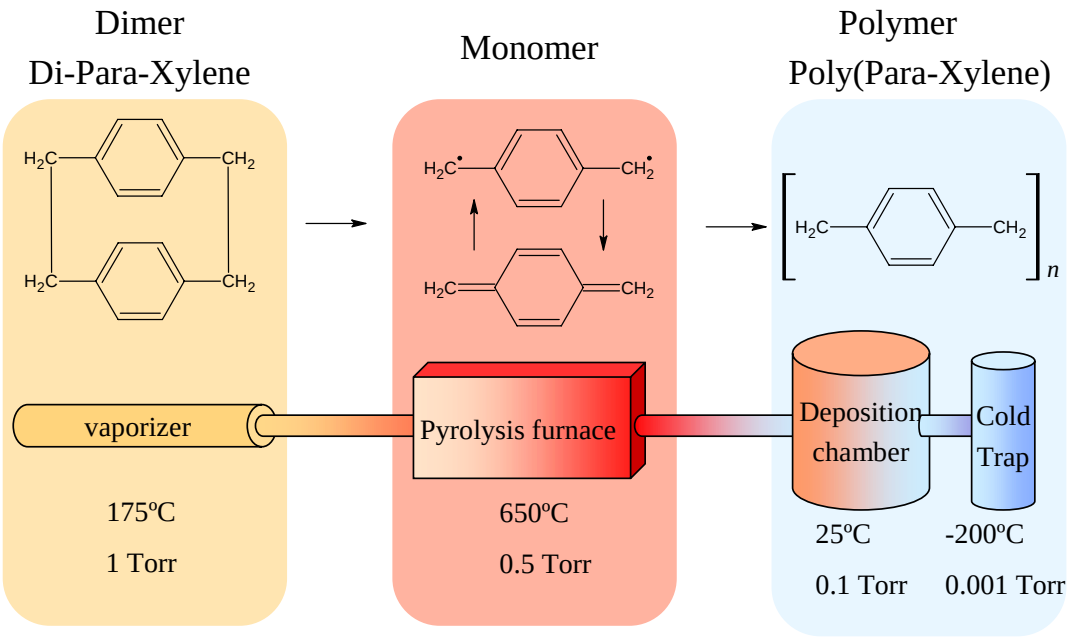

Figure 4.6: *The parylene coating process*

profilometer. They ranged between 0.5 and 1.7μm. From this value (t) and the tabulated dielectric constant of parylene (ϵ_r= 2.65) the gate insulator capacitance per unit area (C_i) was calculated by applying Eq. 4.1,

$$C_i = \frac{\epsilon_r \cdot \epsilon_o}{t} \tag{4.1}$$

assuming the simple model of a parallel-plate capacitor.

On top of the parylene layer, between the source and drain, the gate electrodes were painted with colloidal graphite paint. Besides carbon paint a 30 nm thick silver film was also deposited as a gate contact material. A

disadvantage of this method is that the thermal load of the evaporation process sometimes damages the parylene layer; in that case a huge leakage current is observed.

The described fabrication technique is distinguished by its generality and reproducibility. With parylene as a gate insulator material, I was able to successfully produce FETs based on a variety of organic as well as transition metal dichalcogenide semiconductors. The output of working devices, at least for rubrene single crystal FETs, approached 100%. Additionally, the parylene films deposited onto crystals withstand multiple thermal cycling between 300 K and 10 K, an important feature for low temperature measurements. A schematic and a photo of a ready device are shown in Fig. 4.7.

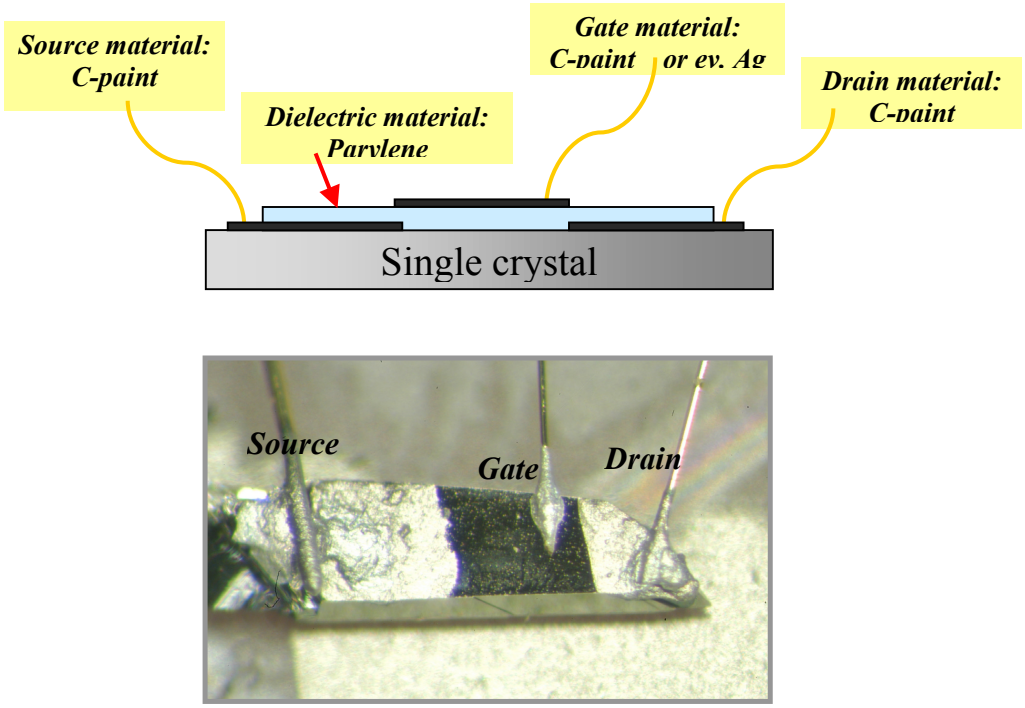

Figure 4.7: *A schema of a FET, summarizing all materials used for the device fabrication. The bottom part of the figure shows a photo of a pentacene single crystal field effect transistor.*

At room temperature, the transistor characteristic was measured using a HP test fixture connected to a HP 4145B semiconductor parameter analyzer. The low temperature measurements were performed in helium atmosphere in a Quantum Design cryostat with a secondary Pt100 resistor in proximity to

the sample to crosscheck the temperature. Data were also collected with an HP 4145B semiconductor parameter analyzer. In all the measurements, the source-drain voltage V_SD and the gate voltage V_G were applied with respect to the grounded source contact (see Fig. 2.2).

Chapter 5

Rubrene

Field effect transistors based on rubrene single crystals demonstrate a maximal hole mobility of 13 cm^2/Vs. The mobility values obtained from the FET characteristics are reproducible and nearly electric field independent. A strong anisotropy of the mobility has been observed. The mobility increases very slightly with cooling but decreases significantly at low temperatures.

5.1 Introduction

Rubrene is distinguished from all other organic semiconductors by an exceptionally high carrier mobility of 30 cm^2/Vs at 200 K [PMB+04] in single crystal field effect transistors. This places it in the center of interest of many groups working on plastic electronics. Pentacene and related acenes, oligothiophenes and fullerenes are the most studied organic FET materials today, and have the highest reported mobility, around ten times lower than rubrene. The carrier transport mechanism in all of these organic semiconductors is still not well understood. The lack of defect-free crystals and the immaturity of organic FET technology seem to limit wider applications of organic semiconductors in microelectronics. In particular, it is still impossible to predict how far, in what way the room temperature mobility can be increased, and why the mobility in organic semiconductors doesn't increase dramatically upon cooling. Therefore, I believe that further study of the technology and the operation of the rubrene single crystal FET will significantly contribute to improving the properties of other FETs and lead to the design of molecules with the desired enhanced properties. Nevertheless, the currently achievable mobility in thin-film organic FETs, such as amorphous silicon, is high enough for many practical applications like organic LEDs, FETs and solar cells. Still, an increase of mobility would simplify circuit de-

sign and allow fabrication of high frequency microelectronic devices. Rubrene has many advantages; it is commercially available and therefore easy to acquire. When grown from the vapor phase, rubrene forms large, orthorhombic, high quality crystals characterized by a small mosaic spread. Measured physical parameters such as high mobility have been reproduced in several laboratories using different crystal growth and FET preparation methods [PPG04, PMB$^+$04, SdBIM04, BLR04, GHK$^+$04]. In this Chapter, I compare rubrene single crystal FETs using Parylene as a dielectric material and compare my results with those reported earlier [GHK$^+$04, PPG04, PMB$^+$04].

5.2 Rubrene room temperature measurements

At room temperature, carrier mobilities above 1 cm^2/Vs have been routinely achieved on numerous rubrene crystals from different batches. The output characteristic of a rubrene single crystal device is presented in Fig.5.1. The

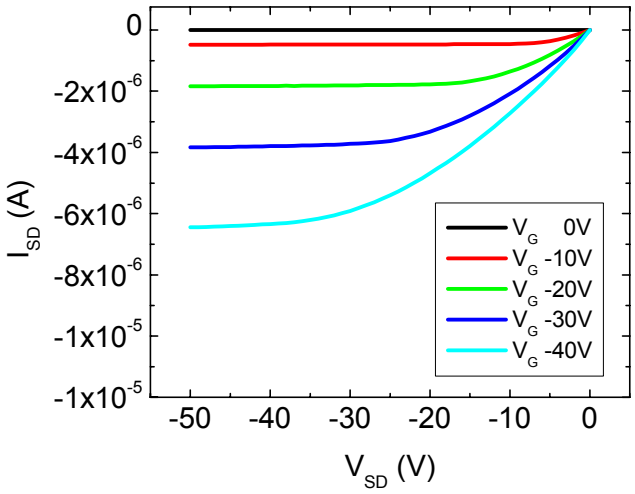

Figure 5.1: *The output characteristic of a Rubrene single crystal FET*

highest mobility I obtained was 13 cm^2/Vs, as derived from the saturation region. This is slightly less than reported FET mobilities obtained using PDMS stamps on rubrene single crystals [PMB$^+$04], but it is still exceptionally high compared to other organic single crystals, like pentacene (2.2 cm^2/Vs) [RKT$^+$] and tetracene (1.3 cm^2/Vs) [GHK$^+$04]. Besides the high field effect mobilities, the devices showed small threshold voltages V_{TH} (below -1V), a relatively large on/off ratio of 10^5 and a sharp field effect onset.

Additionally, nearly all transistors showed a quadratic dependence of the saturation current versus the gate bias ($V_G^x \propto I_{SDsat}$ for $x \sim 1.8 - 2.1$) (Fig.5.2) and a linear behavior of the source-drain current for gate bias $V_G < |V_{SD} - V_T|$ ($V_G^x \propto I_{SD}$ for $x \sim 0.8 - 1.1$). These FET features imply ohmic source and drain contacts [LPS03]. This goes along with the

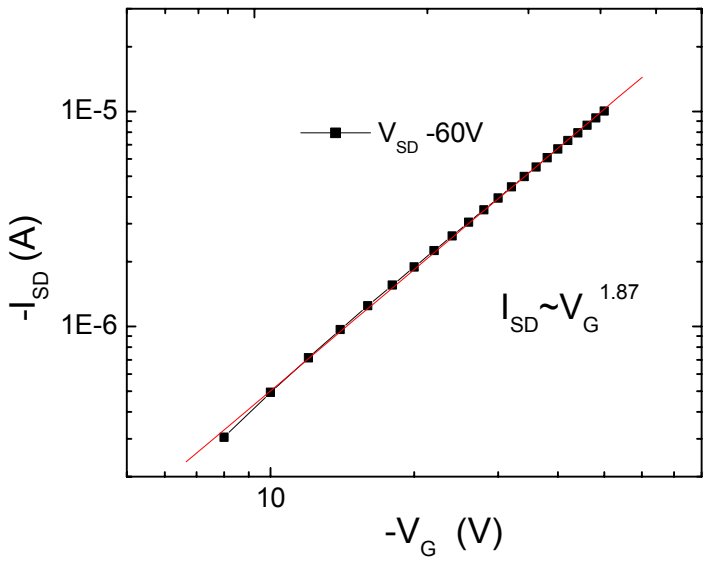

Figure 5.2: *The dependence of the saturation current on the gate bias*

fact that for a sufficiently large gate- and source-drain bias (-20V), the carrier mobility is independent of the longitudinal field (source-drain voltage) and only weakly dependent on the transverse field (gate voltage) (Fig.5.3). For $V_{SD} = V_G$, a peak in mobility and decrease of mobility with increasing gate voltage is observed. This peak is predominant in the crystals showing the highest mobility. Such a dependence was not observed in any other organic material since the mobility in other materials was significantly lower than in rubrene. It is possible that the high quality of rubrene FETs allows one to see the first indications of channel narrowing. Such an effect has already been observed in inorganic FETs where the mobility is higher. However, the lack of a pronounced mobility increase upon cooling prevents me from definitely excluding the contact effect [PSL$^+$03] on the conductivity of the channel. The quality of the rubrene crystals has been tested by measuring x-ray rocking curves. A single peak of the (600) Bragg reflection was observed with the full width at half maximum of around 0.016°, indicating a small mosaic spread in the crystals. This value is about a factor of five smaller than in

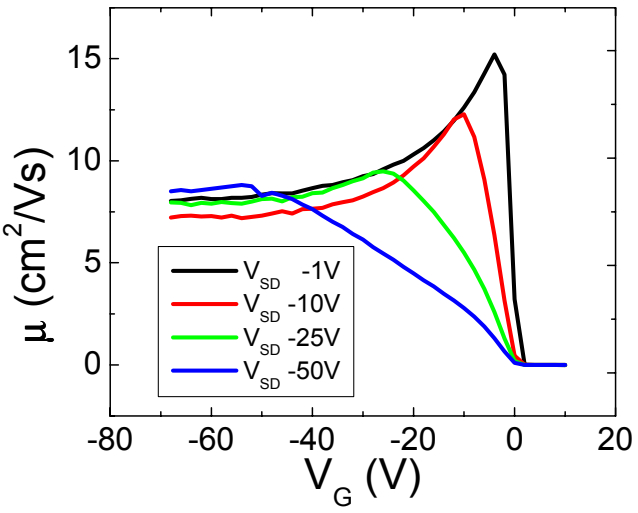

Figure 5.3: *The mobility versus the gate voltage. (calculated from the linear regime)*

other crystals, such as pentacene [Sie]. It is not clear if the low mosaicity is connected with the high symmetry (orthorhombic) of rubrene crystals but the agreement between high mobility and perfect crystallinity in rubrene is remarkable.

Due to the anisotropy of the crystal structure and the direction-dependent overlap of the π-electrons, the charge transport properties of molecular crystals are expected to be anisotropic. Anisotropy has been observed in time of flight measurements [KM01] in antracene single crystals and on single crystal rubrene FETs using PDMS stamps [SZP$^+$04, PMB$^+$04]. To study the anisotropy of a rubrene single crystal I chose a source and drain contact configuration as shown in Fig.5.2. Such a configuration allows the measurement of three field effect transistors in two different crystallographic directions on the same crystal. I picked a thick crystal grown close to equilibrium in a sealed ampoule. Four contacts in the configuration presented in Fig. 5.2, served alternatively as source or drain electrodes. The whole crystal (100) face was covered by a parylene layer and between each two electrodes a gate contact was placed. Within the (100) plane, the highest mobility (5.3 cm^2/Vs) was observed along the b direction, which is consistent with the molecular packing in the rubrene crystal. The π-electron overlap of the adjacent molecules in the b direction is the highest and the mobility is 3-times greater along the b-direction than along the a-axis. For comparison, V. Podzorov et. al. reported a ratio of anisotropy between 2.5 and 3. [PMB$^+$04].

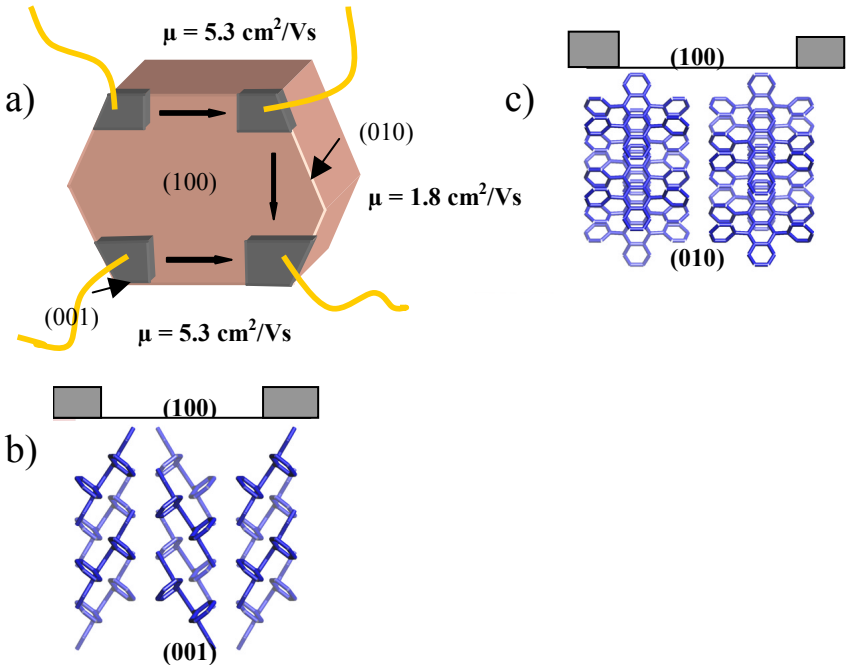

Figure 5.4: *a) The source-drain contact configuration to measure the mobility in different crystallographic directions. b) The crystallographic structure along the b direction. c) The crystallographic structure along the a direction.*

The source drain current flows in a thin surface layer. Therefore, the growth steps formed during crystal layer by layer growth may be responsible for the observed anisotropy. On the rubrene (100) face AFM measurements were performed. Fig.5.5 shows a representative profile of the rubrene crystal surface. 1.3-1.4 nm high monolayers steps were observed separated by 600 nm wide terraces. However, larger step free regions up to 3 μm^2 were also found. These measurements show an excellent molecular smoothness of rubrene surfaces and the observed anisotropy results from the bulk orientation of molecules and not from any anisotropy of the steps on the crystal surface.

5.3 Rubrene low temperature measurements

Two transport regimes are seen on Fig.5.6: at high temperatures, T=260-300K, the mobility increases with cooling; at T<260K, the mobility rapidly decreases with cooling. The gain in mobility is only 15% from 6.5 to 7.5

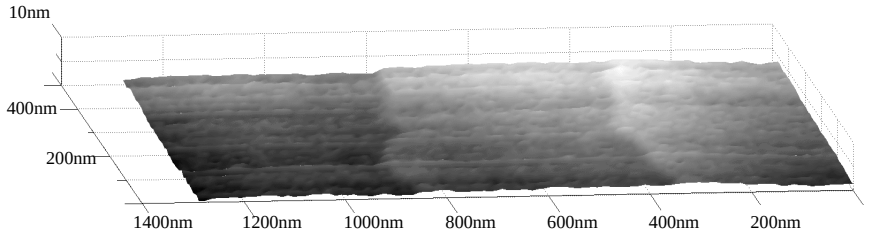

Figure 5.5: *AFM picture of the rubrene (100) face*

cm^2/Vs. Podzorov et al. [PMB+04] described a larger mobility increase with cooling (of approximately 50%), which may be explained by the fact that the deposition of parylene on the single crystal surface causes more defects in the channel than in Podzorov's stamps measurements. The low-temperature drop can be fit (over a limited range 200-120K) by an activation dependence

$$\mu(T) = \mu_0 \exp(-T_0/T) \tag{5.1}$$

with the activation energy $k_B T_0 \sim 25meV$. The former regime corresponds to the intrinsic transport of polaronic charge carries, whereas at low temperatures the charge transport is dominated by the multiple trapping and release of carriers by shallow traps [HHH00, PMB+04]. Observation of the signatures of the intrinsic transport at high T does not imply that the trapping process is completely eliminated. On the contrary, the higher the temperature, the higher the total number of shallow traps involved in the trap-and-release processes. However, at high T, the time that the polaron spreads within a shallow trap with energy E_{tr}

$$\tau \propto \exp(E_{tr}/k_B T) \tag{5.2}$$

might be smaller than the time it propagates between the traps, τ. If this is the case ($\tau_{tr} \ll \tau$), the effective drift mobility in the MTR model [Bub60]

$$\mu = \mu_0 \left(\frac{\tau}{\tau + \tau_0} \right) \tag{5.3}$$

reduces to the intrinsic (trap-free) mobility μ_0. In the opposite limit (τ_{tr}), the charge transport is dominated by trapping and $\mu_{eff} = \mu_0(\tau/\tau_{tr}) \propto \exp(E_{tr}/k_B T)$. This regime is observed for the studied rubrene FET at T<260K. The exponential drop of μ with decreasing T in this transport regime is governed mainly by the exponential increase of τ_{tr}. The activation energy in the Arrhenius-like dependence, $k_B T_0$ (Fig.5.6) is the integral characteristic of a broad distribution of shallow traps rather then a single trap

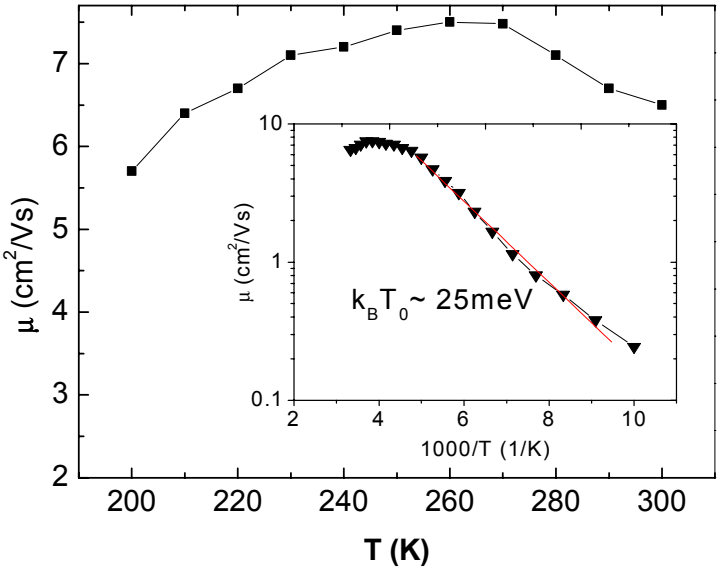

Figure 5.6: *The temperature dependence of the field-effect mobility of a rubrene OFET. The inset is an Arrhenius plot of the mobility for the same device*

level. The crossover from the intrinsic to the thermally-activated transport has also been observed in TOF measurements of organic crystals with low impurity concentrations [PK75].

To summarize, single crystals grown from purified material show excellent crystallinity and very small rocking curve width. Field effect transistors on rubrene single crystals using colloidal graphite electrodes and parylene as a dielectric demonstrate a maximal mobility of 13 cm^2/Vs. A strong anisotropy of the mobility has been measured. The mobility slightly increases with cooling but drops significantly at low temperatures. I was able to reproduce many of rubrene features previously observed by other authors, to improve the crystal growth process and to make progress in single crystal FET technology. However for a better understanding of the physics of rubrene devices, further technological progress is required. A significant increase of low temperature mobility and a better understanding of the surface chemical processes addressed in ref.[PPG04] will contribute to increased appreciation of organic semiconductors.

Chapter 6

Impurities

Obtaining pure crystals of a high quality is the first challenge in the process of making single-crystal organic field-effect transistors. Structural defects and impurities in crystals can seriously deteriorate the desired electronic transport properties of the crystal by creating physical and chemical traps. In the case of anthacene for example, it has been shown that even ppm traces of the natural impurity tetracene will form charge traps for holes and electrons [Kar90]. Due to the prominent position of rubrene and pentacene in the research of OFETs, this chapter focuses on their impurities, which are formed during the growth process or already exist as byproducts in the commercial powder.

6.1 Impurities of rubrene

During the crystal growth process, downstream from the red rubrene crystals, small pale yellow needle-like crystals are also formed (Fig. 6.1). These

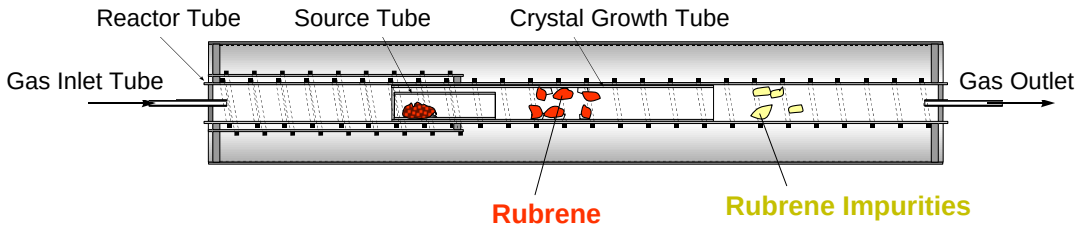

Figure 6.1: *The horizontal vapor phase transport method. The formation of rubrene (red crystals) and the impurities of rubrene (pale yellow crystals) in different zones of the furnace.*

impurities were collected and used for further gas phase crystal growth. An x-ray structure analysis was performed using these crystals, and two rubrene related molecules were identified . Compound A, ($C_{42}H_{30}$) is richer; the other compound B ($C_{42}H_{26}$) is poorer in hydrogen than rubrene ($C_{42}H_{28}$). The molecular structure of both molecules A and B is shown in Fig. 6.2.

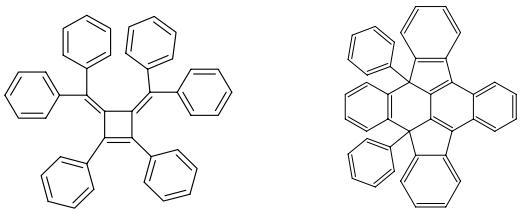

Figure 6.2: *On the left, the molecular structure of compound A ($C_{42}H_{30}$). On the right, the molecular structure of compound B ($C_{42}H_{26}$)*

Molecule A has been reported earlier to form by the reaction of diaryl 1,1 dibromoethylene with active metallic nickel [IMO88]. Since dibromoethylene is used in the syntheses of rubrene [DBC90], this indicates that molecule A is likely to be present in the starting material. This is consistent with the mass spectroscopy data where traces of compound A in the commercial rubrene were found. Molecule B has two hydrogen atoms less than rubrene, suggesting an oxidation reaction taking place during the growth process. This may be possible because the carrier gas (argon) that was used for growing crystals has also few ppm of oxygen. The structure of the molecule can be explained as the fusing of the phenyl rings to the tetracene backbone (Fig. 6.3). Compound A crystallizes in a monoclinic unit-cell with space group

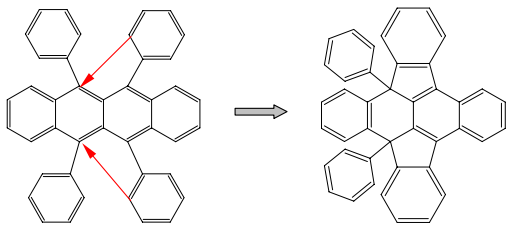

Figure 6.3: *Formation of compound B*

$P2_1/n$. Around the cyclobutadiene, six phenyl groups are present, four of them attached two by two to an intermediate carbon atom. The planes formed by these rings are at different angles out of the plane of the central

four-atom ring. The phenyl groups of molecule A show quite a large deviation from being parallel. This can be explained by the molecular packing in which the phenyl groups are avoiding each other. Although the phenyl groups are oriented at different angles, the molecule stays reasonable flat. As

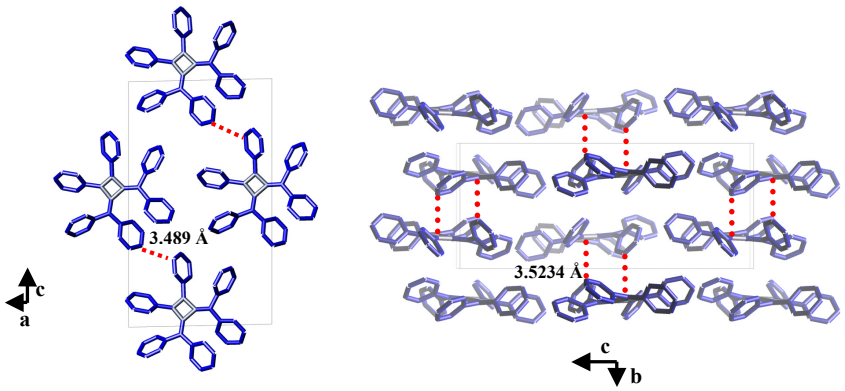

Figure 6.4: *Packing of the molecules in compound A: On the left, one of the layers is shown. On the right, the arrangement of the layers in the crystal.*

shown in Fig. 6.4, a layer of molecules is formed. The molecular packing is obtained by applying the 2_1 symmetry, forming parallel layers perpendicular to the b-axis (Fig. 6.4). The remarkably short carbon-carbon intermolecular distance (3.49 Å) occurs between molecules in the plane. The shortest distance between two parallel planes is 3.52 Å, this distance occurs between a carbon of the four-member rings and a carbon of a phenyl group.

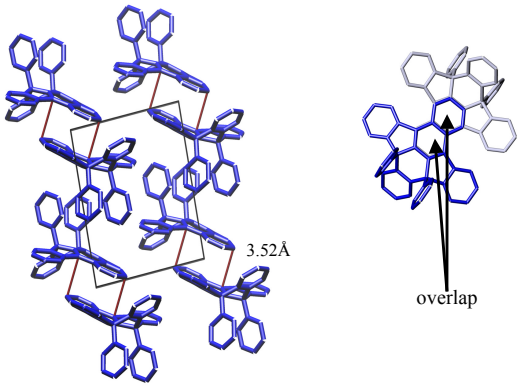

Figure 6.5: *Packing of the molecules in compound B: On the left, the crystal structure. On the right, the overlap between the two closest molecules.*

The molecules constituting compound B have a structure very similar to rubrene. The two five-member rings are fused with the tetracene-like part of the rubrene molecule. This arrangement breaks the extended aromatic system on the tetracene backbone, producing a curvature. The molecule is quite bulky due to two remaining phenyl groups that are pointing outwards. To take care of these and pack as efficiently as possible, the molecules associate pairwise, turning the phenyl groups in opposite directions (Fig. 6.5). The distance between two molecules in such a dimer is 3.521 Å and there is an overlap of the two molecules via two phenyl groups [Bes04].

On the surfaces of both compounds, A and B, I prepared single crystal field effect transistors. In compound A, every second bond is a double bond and the molecule has 21 π-electron pairs. Every carbon atom has an sp^2 hybridized electron. The device showed field-effect (Fig. 6.6). At room

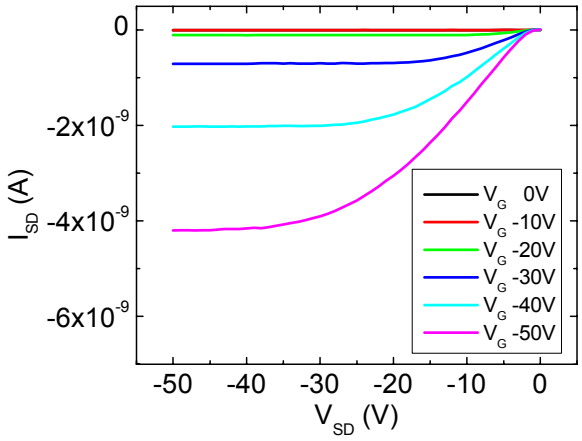

Figure 6.6: *The output characteristic of a compound A ($C_{42}H_{30}$) single crystal FET*

temperature, the field effect transistor exhibits an on/off ratio larger than 10^4 . From the saturation regime I determined a hole mobility of around 2.3 $*10^{-2}$ cm^2/Vs. In contrast, the second compound, with the same number of carbon atoms has 20 π-electron pairs and the sp^2 hybridization of some carbon atoms has been lost. The molecule B is not field-effect active.

As a conclusion, the discovery of compound A and B emphasizes the necessity of a good knowledge of the crystallization process and the starting material. Compound A is still a conjugated molecule, therefore the device based on compound A showed quite good field-effect properties.

6.2 Impurities of pentacene

At moderate temperatures (320℃), the material pentacene undergoes several disproportionation reactions, which produce 6,13-dihydropentacene and a series of polycondensed aromatic hydrocarbons (Fig. 6.7). Additionally, oxygenated byproducts like 6,13-Pentacenequinoe and 6-Pentaceneone (Fig. 6.7) were formed when UHP grade argon (O_2 2ppm) was employed as carrier gas for the crystal growth process.

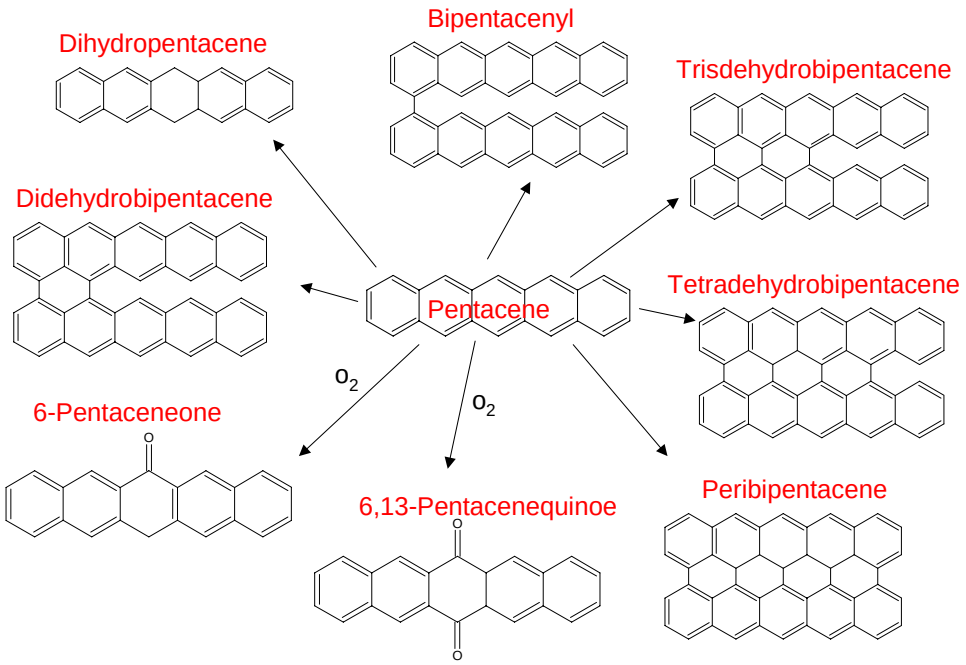

Figure 6.7: *The disproportionation products of pentacene during sublimation*

To reduce the formation of these disproportionation products, the following procedure was used for preparation of ultrapure single crystals. First, commercial pentacene was sublimed in a 30 ml/min flow of argon at 200-320 C° temperature gradient. The pentacene crystals were accompanied by black residue in evaporation source and a violet-blue deposit in low temperature. Pentacene crystals separated from residues were used for subsequent crystal growth in a sealed ampoule. The absence of inert gas provided for sublimation at a slightly lower temperature thereby producing thicker crystals. On the (001) surface of these crystals field-effect transistors were built. The output characteristic of one of these devices is presented in Fig. (6.8).

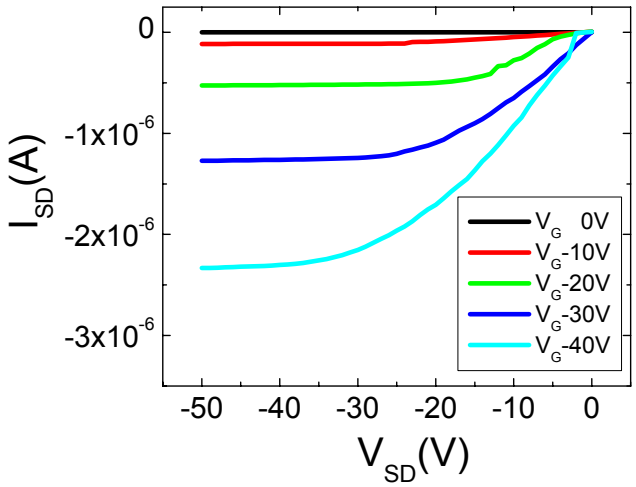

Figure 6.8: *The output characteristic of a pentacene single crystal FET*

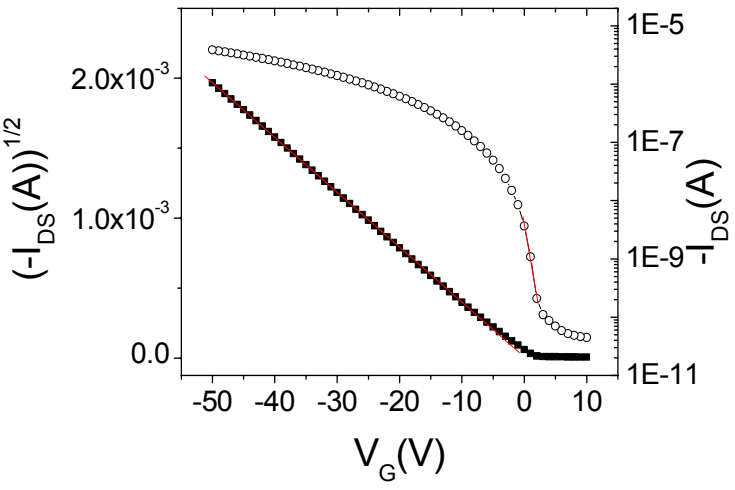

Figure 6.9: *The trans-conductance characteristic of a pentacene FET measured at a fixed $V_{SD} = -60V$ (right axis) and the square root of the drain current in the saturation regime as a function of the gate voltage. (Left axis)*

From the square root of the source drain current ($\sqrt{I_{SD}}$) versus gate voltage (V_G) characteristics (Fig. 6.9), I extracted a field-effect mobility of 2.2 cm^2/Vs. This value is the highest reported for pentacene single crystals [RKT+]. Additionally, the OFET operate as a zero threshold device. The zero threshold operation suggests that the density of the charge traps is very low ($< 10^9 cm^{-2}$). From the trans-conductance characteristic presented in Fig. 6.9, an on/off ratio of 10 ^{5}is obtained. The well defined field-effect onset (Fig. 6.9) of the single crystal OFETs characterized by the subthreshold slope S also reflects a low defect concentration in the single crystal channel. For the studied pentacene devices I calculated a subthreshold slope as small as S = 1.5 V/decade, which corresponds to normalized subthreshold slope of Si = 3V·nF/decade·cm^{-2}. The high purity of the pentacene crystals, with

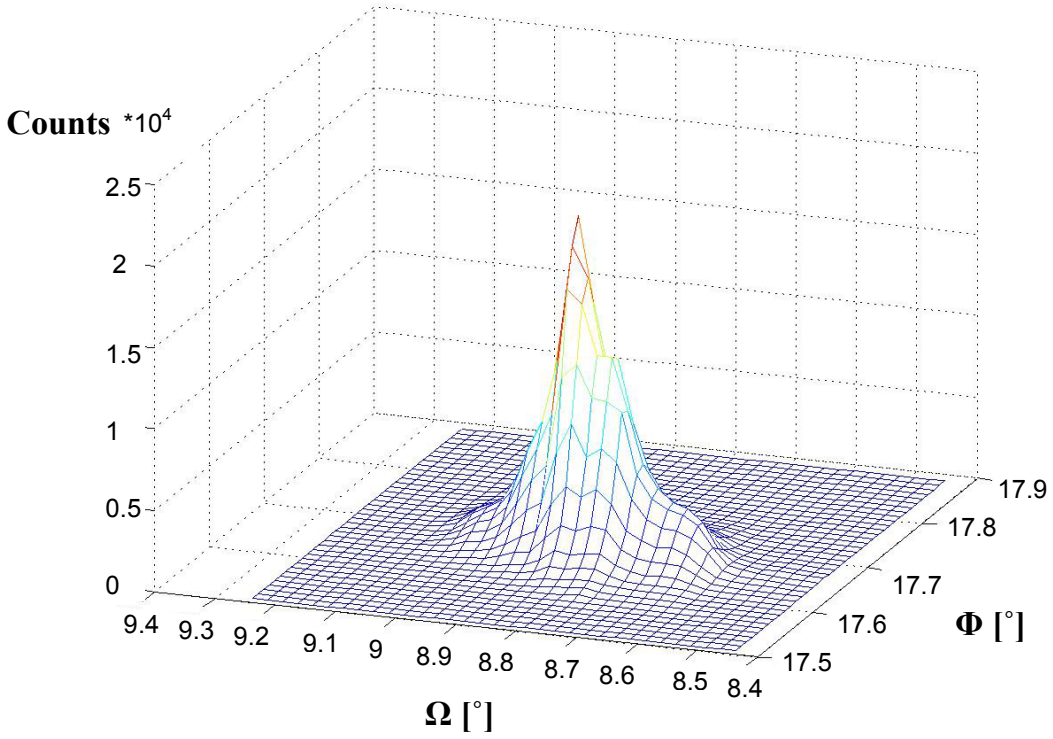

Figure 6.10: *A 2-dimensional rocking curve of pentacene*

only few structural defects has been confirmed by measuring x-ray rocking curves presented in Fig.6.10. The sharp peak of the 2-dimensional rocking curve indicates a small mosaic spread in the crystals.

In conclusion, by optimization of the crystal growth process, avoiding the formation of pentacenequinones, hydrogenated pentacene and other polycon-

densed aromatic hydrocarbon compounds the field-effect mobility has been significantly increased in pentacene-based single-crystal OFETs. The single-crystal devices demonstrate zero threshold operation and very small sub-threshold slopes. The high quality of these single crystals is also reflected in the sharp peak of the 2-dimensional rocking curve.

Chapter 7

Copper phthalocyanine

In this chapter the performance of single crystal field effect transistors based on Copper phthalocyanine (Cu-Pc) is evaluated. These FETs function as p-channel accumulation-mode devices. The high charge carrier mobility combined with a low field-effect threshold along with the highly stable chemical nature of Cu-Pc make it an attractive candidate for device applications.

7.1 The technical relevance of Cu-Pc

Since the first paper on copper phthalocyanine ($CuN_8C_{32}H_{16}$) of de Diesbach and von der Weid in 1927 [dDvdW27], extensive research has been carried out on this material. Fig. 7.1 shows the molecular structure of copper phthalocyanine. The outstanding chemical stability and strong blue dye properties

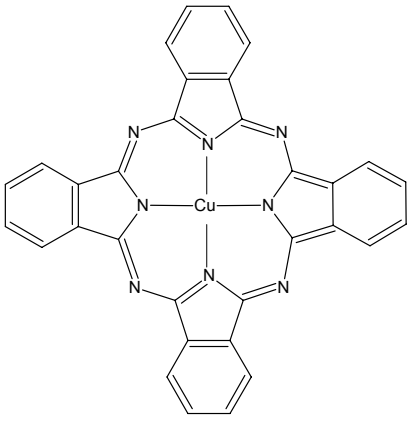

Figure 7.1: *The molecular structure of copper phthalocyanine*

of Cu-Pc resonate through numerous papers and reviews. Several hundred literature references and patents describe the significance of Cu-Pc in science and technology. Mostly, it has been used as paint and dye for textiles and plastics as well as ballpoint pen and printing inks. Even food coloring with Cu-Pc was announced [MT83]. Recently, Cu-Pc has also been applied in chemical sensors [FSMP98] and optical data storage [RKHS97]. The semiconducting behavior of metal phthalocyanines was described as early as 1948 [Var48], but only recently have thin-film field-effect transistors based on Cu-Pc been considered as potential candidates for flexible electronics. However, the reported low thin film field-effect mobilities of α-Cu-Pc [BLD96], much lower than amorphous silicon, have limited the use of this material for transistor applications. Moreover, the high chemical stability of Cu-Pc distinguishes this material from other high mobility organic semiconductors, like pentacene or rubrene, and stimulates research on improving the electrical properties of this compound. [BGMP04] Additionally, the lack of reports on photochemical reactivity of Cu-Pc suggests that this material is suitable for light emitting diodes, organic lasers, or solar cell applications. The capabilities of Cu-Pc have not been well recognized since most research has been conducted on thin films, which crystallize in the α-phase polymorph, where disorder and grain boundaries mask the intrinsic semiconducting properties. To avoid grain boundaries and limit the concentration of impurities and defects, Cu-Pc single crystals were used to evaluate the transport properties.

7.2 Crystal structure and rocking curve

The structure (Fig.7.2) of the gas-phase-grown Cu-Pc single crystals was confirmed by X-ray diffraction to be the same as described in ref. [LR36a, LR36b]. They crystallize in the beta form, with monoclinic unit cell parameters a =14.616(2)Å, b =4.8042(6)Å, c =17.292(3)Å, and β=105.39(2)Å, and space group $2P_{1/n}$, Z=2. This unit cell may be obtained from the original unit cell by the transformation (0,0,-1;0,1,0;1,0,1). The molecular packing produces two individual tilted stacks of Cu-Pc molecules running along the b-axis that are tilted against each other by 90°.

The quality of the Cu-Pc crystals has been tested by measuring x-ray rocking curves of the (-101) face presented in Fig. 7.3. A single peak of the (-404) Bragg reflection was observed with the full width at half maximum of around 0.05°, indicating a small mosaic spread in the crystals.

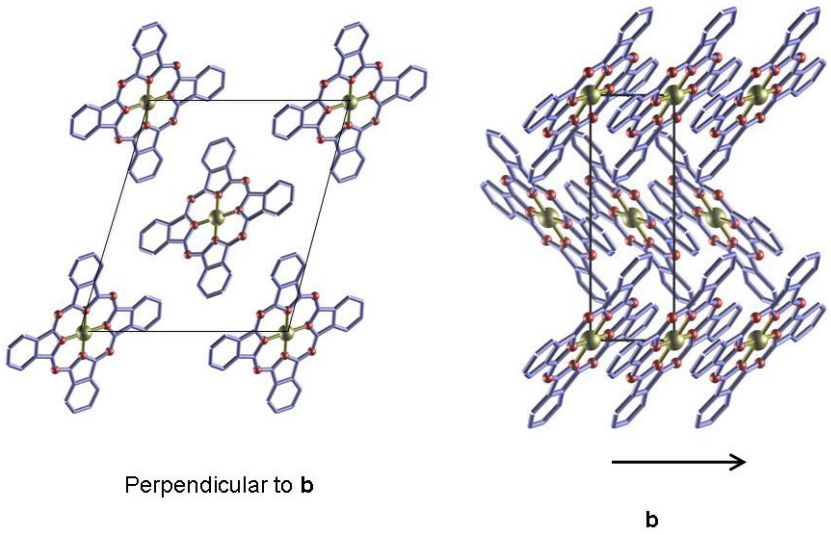

Figure 7.2: *The crystal structure of the β-phase of copper phtalocyanine (Cu-Pc). A strong π-orbital overlap exists along the b-axis.*

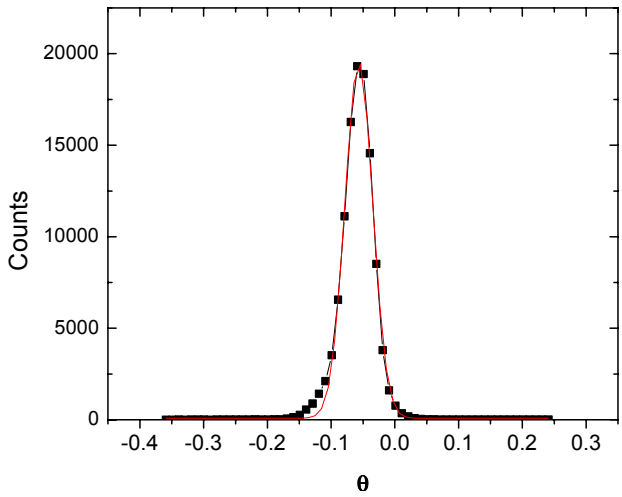

Figure 7.3: *The rocking curve of the Bragg reflection (-4 0 4)*

7.3 FET-characteristics of Cu-Pc

The Cu-Pc single crystals form long needles, therefore the charge-transport properties were measured in the direction parallel to the long crystal axis (b-axis) on the (-101) face. As shown in Fig.7.2, this direction corresponds to the strongest overlap between π-orbitals of adjacent molecules.

The current-voltage (I-V) characteristics of a Cu-Pc single crystal device with a channel length L of approximately $380\mu m$ and width W of 100μm is presented in Fig.7.4. The channel width was limited by the width of the crystals. For small source-drain voltages (V_{SD}) the FET operates in the linear regime. If the source-drain voltage is increased, the gate field is no longer uniform and a depletion area is formed at the drain contact. Beyond a certain source drain voltage the current becomes saturated. From

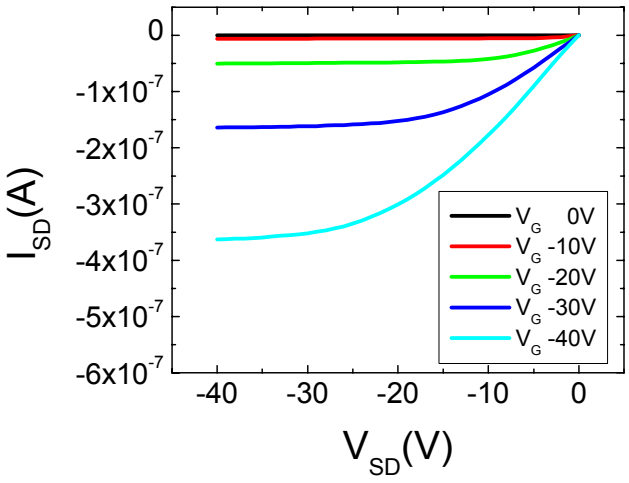

Figure 7.4: *The output characteristic of a Cu-Pc single crystal FET*

the trans-conductance characteristic, I obtained a threshold voltage (V_T) of around -5V at $V_{SD} = -40V$ (Fig. 7.5). Assuming that the density of electrically active traps is proportional to the charge needed to fill them, the density of the charged traps at the Cu-Pc/ Parylene interface is estimated to be $3{\cdot}10^{10}$ cm^2. The low threshold voltage and resulting low trap density indicates the high quality of the single crystals. A negative onset voltage V in p-type transistors indicates a "normally-off" FET. From this trans-conductance characteristic I also determined an on/off ratio of 10^4. The sharpness of the field-effect onset is characterized by the subthreshold swing. The Cu-Pc single crystal FETs exhibit a subthreshold swing (S) of S=2.6

V/decade, which is equivalent to a normalized subthreshold swing (S_i) of 7V·nF/decade·cm^{-2}. For pentacene single crystal FETs, I obtain a smaller value (Si = 3V·nF/decade·cm^{-2}) [RKT^{+}]. On the other hand, a normalized subthreshold swing for a thin film field effect transistor based on Cu-Pc estimated from Zang et al. [ZWWY04] is 4-times higher than my value. This also indicates the low defect concentration in the single crystal channel. From the square root of the source drain current ($\sqrt{I_{SD}}$) versus gate voltage

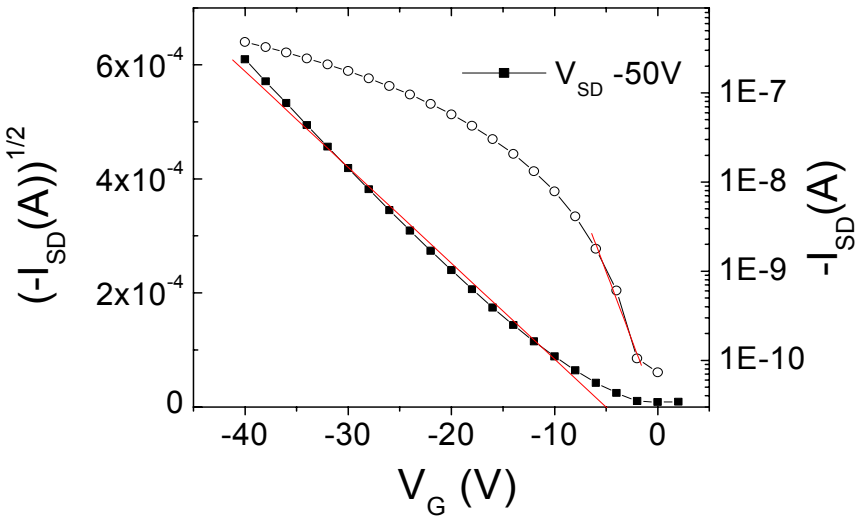

Figure 7.5: *The trans-conductance characteristic of a Cu-Pc FET measured at a fixed $V_{SD} = -40V$ (right axis) and the square root of the drain current in the saturation regime as a function of the gate voltage. (Left axis)*

(V_G) characteristics (Fig. 7.5), I extracted a field-effect mobility of 1cm^2/Vs. The field-effect mobility is estimated for a fixed source drain voltage (V_{SD}) of -40V in the saturation regime using Eq.2.7

This value is an order of magnitude higher than reported by Zang et al. [ZWWY04] for thin film devices having source-drain electrodes sandwiched between copper phthalocyanine (Cu-Pc) and cobalt phthalocyanine (Co-Pc).

It is worth noticing that a mobility of 1 cm^2/Vs is the highest measured in this study but that mobilities between 0.4 and 1 cm^2/Vs are routinely achieved on numerous crystals from numerous batches. This also indicates that substantially improved thin film FETs can be produced by using optimized thin film technology and by tuning the composition and structure of phthalocyanine compounds.

In summary, for CuPc devices a room temperature mobility of about 1 cm^2/Vs and an on/off ratio larger than 10^4 can be achieved. These transistor parameters are comparable with widely used amorphous silicon and the highest hole mobilities reported for "conventional organic semiconductors" like tetracene (1.3 cm^2/Vs) [GHK+04] or pentacene (2.2 cm^2/Vs) [RKT+] (2-2.5 cm^2/Vs) [BLC+]. Taking into account the exceptional chemical stability of copper phthalocyanine, this semiconductor seems to be the material of choice for field effect transistors in displays and organic solar cells. In both these applications, the large amount of light emitted (display) or absorbed (solar cells) would require a very stable semiconductor, and arenes (which photodimerizes and oxidizes) [RKT+] or rubrene (which photo-oxidizes) [PPG04] do not satisfy this requirement.

Chapter 8

Tetracene Derivatives

The substitution of hydrogen atoms by large, polarizable halogen atoms on the tetracene molecule changes only a little the HOMO and LUMO levels; mainly it affects the packing of the molecules. In this chapter, I discuss the different crystal structures of Tetracene derivates and correlate them with their field effect mobilities.

8.1 Crystal structure and mobility

Quantum mechanical calculations have predicted that high mobility in OFETs can be obtained when conjugated molecules have strong interactions with neighboring molecules to maximize the overlap of π molecular orbitals [CBB01]. In addition, Curtis and coworkers have recently made a structural analysis on some common organic semiconductors, discussing the correlation between solid state packing and transport [CCK04]. Theoretically speaking, a cofacial π stacking structure is expected to provide more efficient orbital overlap and thereby facilitate carrier transport. So far, however, most of the organic semiconductors that have shown high mobility and high on/off ratio in polycrystalline thin film devices have a herringbone structure which reduces the overlap [NLGJ98]. In fact, there has been little experimental evidence that π stacked materials have higher mobility. This may be because of the scarcity of π stacked materials [PCF$^+$02, AEP02] and the difficulty of examining transport properties at molecular levels. The mobility in polycrystalline films is not intrinsic but depends on the purity of the conjugated molecules and on the film morphology. Single crystal devices, which are in principle free of grain boundaries, are ideal for the investigation of intrinsic carrier transport properties of molecular semiconductors. In order to study the effect of molecular packing on charge transport, it would be optimal to

have two materials with only a difference in molecular packing while the other parameters such as injection barrier are as similar as possible. In this study, halogenated tetracene derivatives (Fig. 8.1) have been synthesized in which the molecular packing is sensitive to the substituents while their HOMO levels are similar. They provide an ideal system for investigating

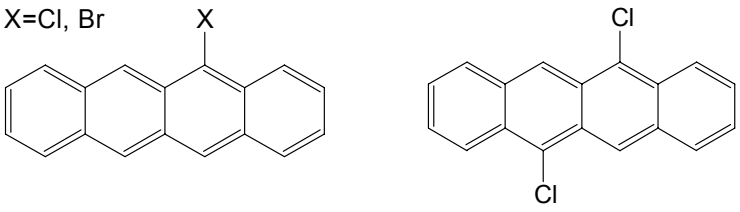

Figure 8.1: *The molecular structures of substituted tetracene*

structure-property relationships among organic semiconductors. The solid state packing pattern of conjugated molecules depends on the nature of both conjugated core and functional groups [CCK04]. Semi-empirical calculations show that substitution of bromo or chloro groups in tetracene lowers both HOMO and LUMO levels. The substitution of electron withdrawing groups is expected to alter not only the size and shape of the molecule but also the electronic properties, which may result in the change of the packing mode of tetracene derivatives. Previously, Sarma and Desiraju pointed out that halogen groups promote π stacking [SD86]. Also, Anthony and coworkers reported that one or more substitutions of relatively bulky groups into peri-postions of polyacenes disrupt the herringbone structure of the compounds [AEP02].

Halogenated tetracene derivatives were synthesized from tetracene using copper chloride, copper bromide or n- bromosuccinimide (NBS) in chlorobenzene or bromobenzene. The products were soluble in common organic solvents and purified with recrystallization or column chromatography. Single crystals were grown from either solution or vapor phase [LKSS98] for structural analysis and transistor fabrication.

Mono-bromo and mono-chloro tetracene are isostructural. They both crystallize in space group $P2_l/c$. The molecules are arranged in a "double" herringbone pattern, where pairs of molecules stack with the halogen on opposite sides (Fig. 8.2). Two such molecules overlap with a displacement of half a benzene ring in both the a and c directions. These stacks are tilted against each other by 34.8° [Bes04]. Even though the molecules are close together, the field effect mobilities of the devices based on mono-bromo and

mono-chloro tetracene single crystals grown from vapor phase is only 0.2 cm^2/Vs and 0.3 cm^2/Vs respectively. Since the molecular packing is still based on a herringbone pattern, the mobilities are therefore rather small.

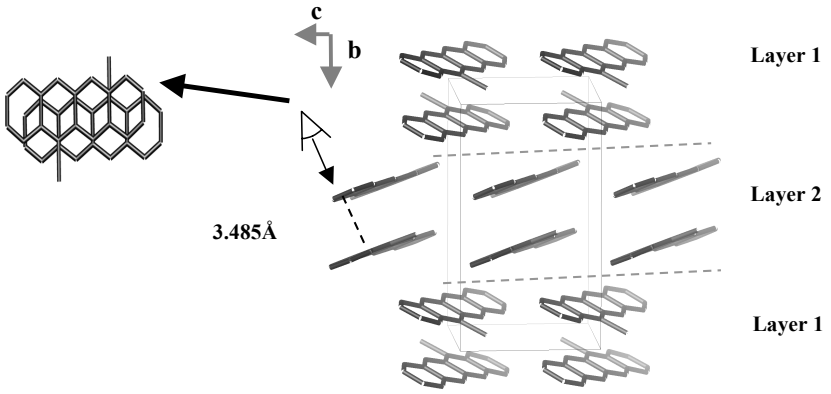

Figure 8.2: *The crystal structure of mono-bromo and mono-chloro tetracene.*

With a second halogen attached in the trans di-chloro tetracene, the molecular packing is even more affected. The molecular packing is shown

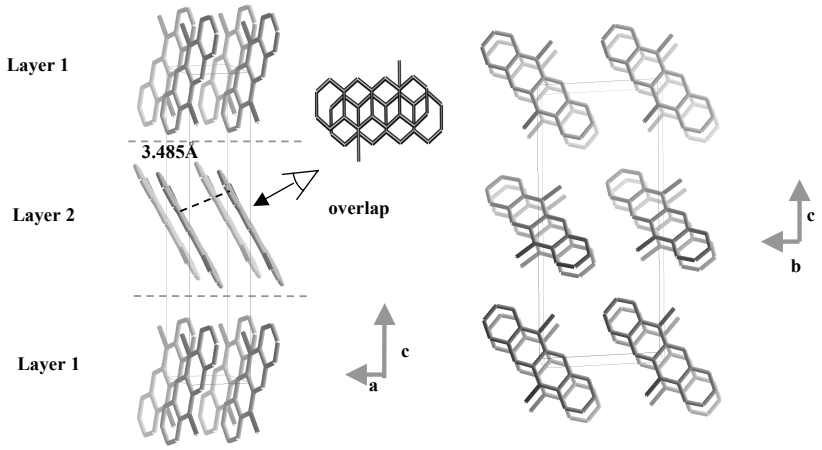

Figure 8.3: *The crystal structure of di-chloro tetracene.*

in Fig. 8.3, where the molecules form individual stacks. The same intermolecular distance and the same overlap is found between the molecules, but

this time the overlap occurs in the whole stack running along the a-axis. As a consequence one can imagine that the hopping process will be easier in this compound along this direction. Such an arrangement is expected to produce one-dimensional conduction paths. The improved packing of the crystal structure is reflected in the hole mobility of $\sim$1.6 cm^2/Vs obtained from the single crystal field effect transistors grown from the vapor phase. The mobility of 1.6 cm^2/Vs may not be the upper limit since the crystal growth and FET-fabrication have not been optimized. For a device with "ohmic" contacts the drain current is expected to vary linearly with the source-drain voltages for gate bias $V_G < |V_{SD} - V_T|$. The output characteristic presented in Fig. 8.4 indicates that this is not the case for single crystal transistors based on di-chlorotetracene. However, the value is higher than for pure tetracene devices [GHK$^+$04].

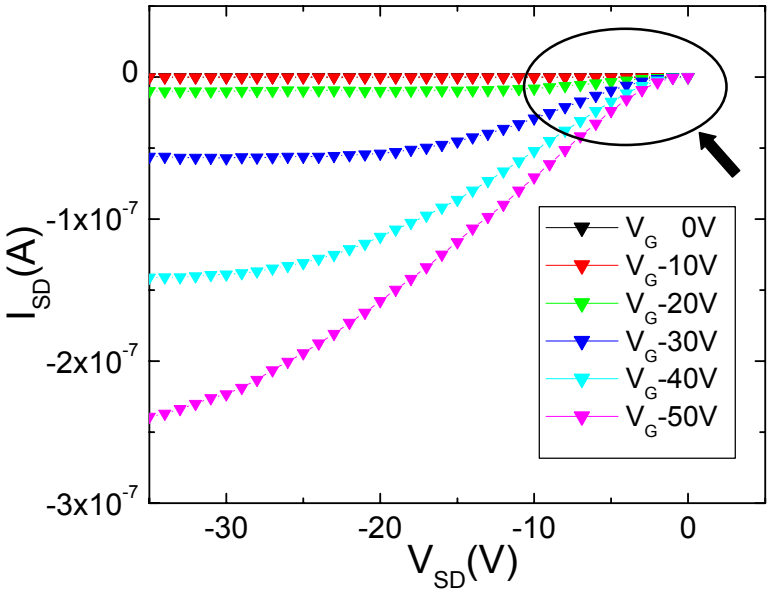

Figure 8.4: *The output characteristic of a single crystal transistor based on di-chlorotetracene. The area marked with a black oval indicates problems with the carrier injection. Therefore, the transistor performance may be contact limited.*

I also built field effect transistors on single crystals grown from solution. The transistor performance of the crystals depends on the quality of the crystals. As given in Table 8.1, crystals grown from solution showed much poorer transistor behavior than those from vapor. This may be attributed to rough surfaces, crystal imperfection, and a high concentration of impurities

in crystals grown from solution due to the incorporation of solvents into the intra-molecular position in the weakly bonded Van der Waals network of molecules. This is important because the conduction channel is located within the first few monolayers of the single crystals at the semiconductor-dielectric interface.

	Crystal growth	Structure	Mobility [cm^2/Vs]	on/off
mono-bromo	Solution	Herringbone	$2.4*10^{-3}$	10^2
	Vapor	Herringbone	0.2	10^2
mono-chloro	Solution	Herringbone	$1.4*10^{-3}$	10^3
	Vapor	Herringbone	0.3	10^3
di-chloro	Vapor	π stack	1.6	10^5
tetracene	Vapor	Herringbone	1.3	10^5

Table 8.1: *Summary of crystal packings and field effect mobilities of single crystal transistors based on tetracene derivatives*

For comparison, thin film transistors were also fabricated by Evert-Jan Borkent(Bell Laboratories) on highly n-doped silicon wafers in both top and bottom contact configuration. Mono-chlorotetracene was thermally evaporated at 10^{-6} Torr to yield cloudy films, showing no field effect in any kind of device. Mobility of thin film transistors based on di-chlorotetracene varied

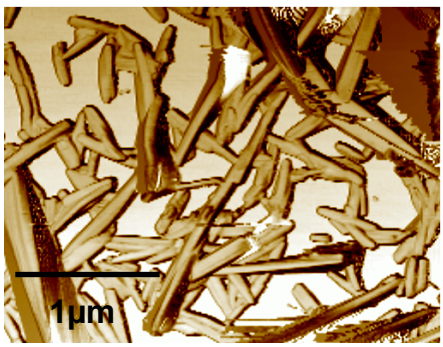

Figure 8.5: *AFM image of di-chlorotetracene thin film deposited on octadecyltrimethoxysilane (OTS) treated SiO_2 substrate at a substrate temperature of 0 ˚C.*

with substrate temperature and surface properties of SiO_2. The best mobil-

ity in thin film devices, 10^{-3} cm^2/Vs, is achieved when di-chlorotetracene is evaporated onto octadecyltrimethoxysilane (OTS) treated SiO_2 (300 nm)/Si substrate held at 0°C. This relatively low mobility can be explained as a result of poor film morphology. The AFM image (Fig. 8.5) showed that evaporated molecules of tetracene derivatives did not cover the whole area of the transistor channel and that the crystallites are not well inter-connected.

In summary, halogenated tetracene derivatives were synthesized and grown into single crystals. Mono-substituted 5 bromo- and 5 chloro- tetracenes have the herringbone structure while 5,11 dichlorotetracene has the π stacking structure. Mobility of 5,11 dichlorotetracene was measured to be as high as 1.6 cm^2/Vs in single crystal transistors. The π stacking structure, which enhances π orbital overlap and facilitates carrier transport, may thus be responsible for this high mobility.

As already discussed in chapter 6, the structural defects and impurities of the single crystals play an important role for the device performance. The calculated mobility for single crystal FETs grown from solution was therefore three orders of magnitude lower.

Chapter 9

Diphenybenzo-dichalcogenophenes

This chapter describes a new prototypical class of materials called Diphenybenzodichalcogenophenes. To develop high performance OFETs, sulfur atoms in the thiophene-comprising molecules are replaced with heavy chalcogen atoms such as selenium and tellurium. This is done in an attempt to enhance the intermolecular overlap. The three materials (those with sulfur, selenium and tellurium) crystallize in a very similar herringbone structure (in contrast to the materials discussed in the previous chapter) and thus allow us to study the influence of chalcogen atoms in very similar surroundings.

9.1 Using single crystals to evaluate new material

Owing to the growing interest in the potential applications of organic semiconductors, the development of new, highly efficient and more stable semiconductors has been of current interest. Due to the relatively low carrier concentration and very high resistivity of pristine organic materials, field-effect transistors continue to be important for evaluating organic semiconductors, as they can give the principal semiconducting parameters such as type of major carrier, mobility of the carrier, on/off ratio, and threshold voltage. One way to find new superior semiconductor material is to use known compounds so far not evaluated as semiconductors, and the other is to design and synthesize potentially interesting new molecules by organic synthetic procedures. In both methods, large and plane π-conjugated molecules appear to be favorable because their molecular structure can maximize the overlap of the intermolecular π electrons, resulting in high carrier mobility. Also the introduction of

long alkyl chains or halogen atoms (see Chapter 8) into plane π-conjugated molecules to facilitate tight packing of the π-backbone in the solid state has been tested. These approaches are based on the idea that large intermolecular overlap brings higher carrier mobility. Another approach to enhance intermolecular overlap is to use heavy chalcogen atoms instead of sulfur atoms in thiophene-based organic semiconductors such as oligothiophenes, thiophene-containing condensed aromatics. Based on this approach, a series of 2,6-dipheneylbenzo[1,2-b:4,5-b']dichalcogenophene derivatives (DPh-BDXs) have been synthesized; the OFET devices fabricated with their thin films are reported to show superior FET characteristics with mobility of $\sim$0.1 cm^2/Vs. Agreeing with our initial expectations the selenium compound

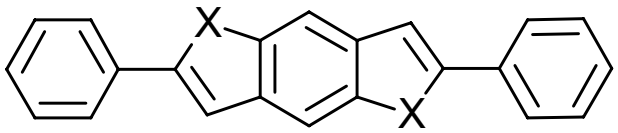

1: X=S, DPh-BDT
2: X=Se, DPh-BDS
3: X=Te, DPh-BDTe

Figure 9.1: *Molecular structures of 2,6-diphenylbenzo[1,2-b:4,5-b']dichalcogenophenes*

(DPh-BDS) shows higher FET mobility than that of the sulfur compound (DPh-BDT), whereas contrary to the expectations the FET mobility of the tellurium compound is the lowest among the series. However, in the thin film FET mobility evaluation, grain boundaries, defects and quality of channel interface in the FET structures may hide the material properties and make it difficult to evaluate structure-properties relations. For this reason, evaluation of organic semiconductors with high quality single crystals is optimal, and therefore I have fabricated single crystal FETs based on DPh-BDXs and reevaluated their device characteristics.

9.2 The FET-performance of DPh-BDXs

The DPh-BDX compounds perform not only as thin film field effect transistors (TFTs) but also as single crystal devices. Table 9.1 compares the TFT and the single crystal FET characteristics of these materials. As expected, I was able to improve the FET hole mobility of all three compounds by using single crystals. However, these mobility values might not be the upper limits for these compounds. Especially in the case of DPh-BDTe, I noticed that

when the crystals were grown in the light, the mobility was $\sim 10^{-2}$ cm^2/Vs combined with a large threshold voltage of ∼-25 V. When the crystal growth was carried out in the dark, the carrier mobility increased and the value of the threshold voltage was reduced, indicating that the concentration of traps in the interface was declining. Unfortunately, it is very difficult to study organic semiconductor/organic dielectric interface in a complete device. Besides the quality of the interface crystal/parylene, for a two terminal device the contact resistance must also be taken into account. It is challenging to distinguish between contact related effects and interface properties of the device. In the following, I present the FET-characteristics of DPh-BDS to exemplify this issue. The source-drain current (I_{SD}) as a function of the

	Thin film FET	**Single crystal FET**
Material	Mobility [cm^2/Vs] on/off	Mobility [cm^2/Vs] on/off V_T [V]
DPh-BDT	0.08 10^3	0.4 10^3 -22
DPh-BDS	0.17 10^5	1.5 10^3 -6
DPh-BDTe	0.07 10^3	0.5 10^3 -5

Table 9.1: *Diphenybenzodichalcogenophenes-Summary of thin film and single crystal device performance*

applied source-drain voltage (V_{SD}) for different gate voltages (V_G)is shown in Fig. 9.2. Similar to rubrene single crystal devices and as expected from the FET theory, for small negative source-drain voltages (V_{SD}) the device operates in the linear regime. When the source-drain voltage increases, the gate field is no longer uniform and a depletion area is formed at the drain contact. Beyond a certain source-drain voltage (V_{SD}), the current becomes saturated. Nevertheless, a more detailed look at the device features reveals the Schottky-barrier of the source and drain contacts.

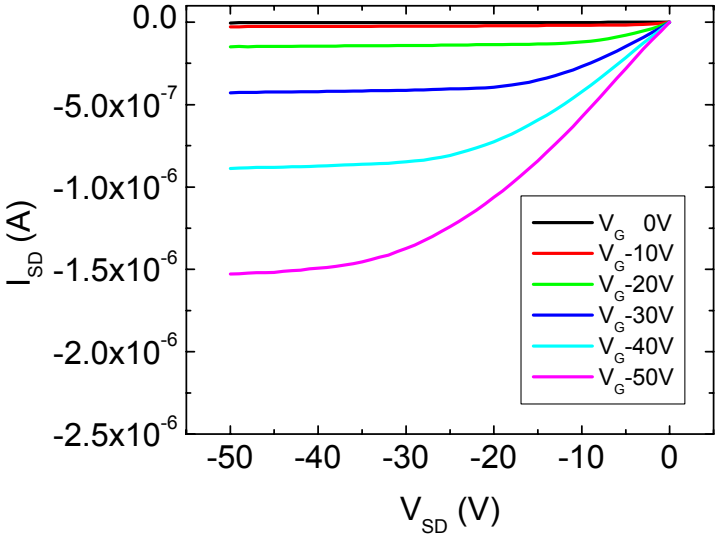

Figure 9.2: *The output-characteristic of a DPh-BDS FET.*

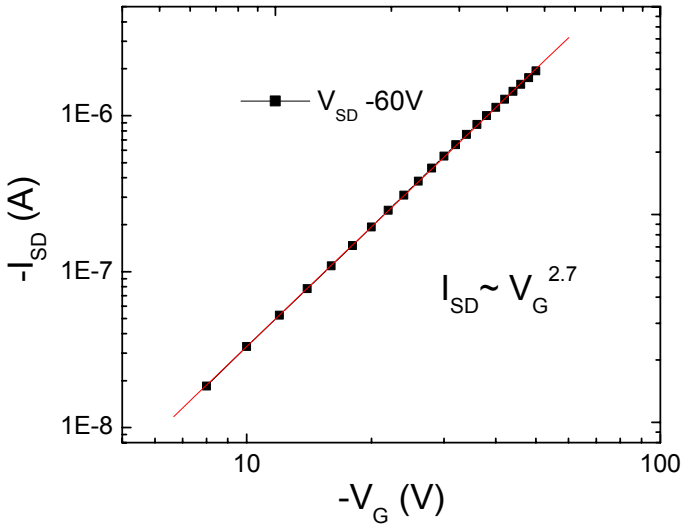

Figure 9.3: *The dependence of the saturation current on the gate bias for a DPh-BDS device*

For instance, the saturation current of a DPh-BDS device (Fig.9.3) depends super-linearly on the gate bias ($V_G^x \propto I_{SDsat}$ for $x \sim 2.7$), whereas rubrene single crystal transistors (see Chapter 3, Fig.5.2) show a quadratic dependence of the saturation current on the gate voltage.

Also the trans-conductance characteristics plotted in Fig.9.4 display a contact related phenomenon. As these characteristics indicate, the DPh-

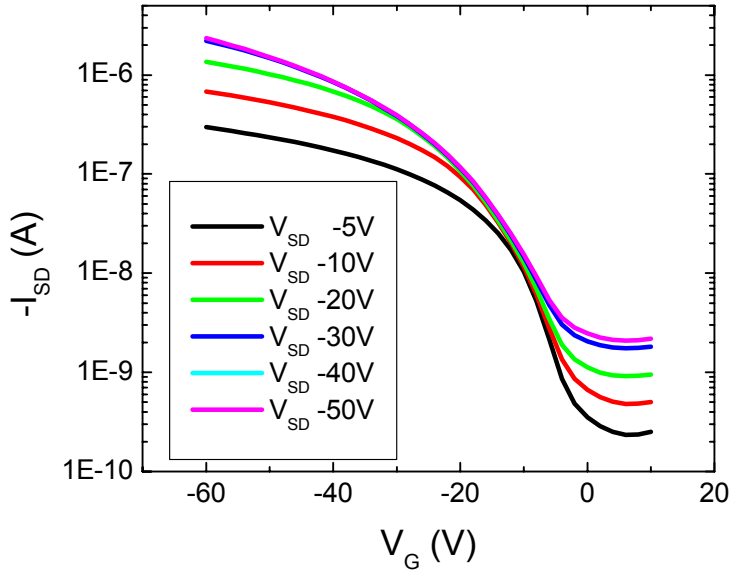

Figure 9.4: *The trans-conductance characteristics of a DPh-BDS FET (same device), for different source-drain voltages.*

BDS single crystal device does not develop a sharp field-effect onset. For small gate voltages, the source-drain current changes only gradually with the applied field. This feature indicates the existence of a resistivity barrier on the contacts. The high contact resistance in a Schottky-type OFET depends non-linearly on the gate voltages. A similar effect that dominates especially in the subtheshold region has also been observed for tetracene single crystal FETs [BGMP04]. Additionally, the trans-conductance characteristics in Fig. 9.4 allow a subthreshold swing (S) of around 7V/decade to be determined, which corresponds to a normalized subthreshold swing (Si) of 11 V·nF/decade·cm^{-2}. For comparison, Rubrene single crystal FETs usually develop a sharper field-effect onset for the best devices; the normalized subthreshold swing is Si=1.7 V·nF/decade·cm^{-2} [PPG03]. The field-effect onset is observed at a negative gate voltage (-1V). For p-type device, this behavior resembles a "normally-off" FET, which seems to be the case for all

organic single crystal field-effect transistors with parylene as a gate dielectric [PPG03, RKT$^+$, BLC$^+$]. Assuming that the density of electrical active traps is proportional to the charge needed to fill these traps, and taking the threshold voltage of -6V from Fig.9.4, the density of the charged traps at the DPh-BDS/parylene interface is $6.6 * 10^{10} cm^{-2}$. In this rough evaluation the contribution of the contacts on the threshold voltage has not been taken into account, but such a procedure allows an estimate of the upper limit of trap concentration mobility. Due to the relatively high bulk conductivity of material the on/off ratio, obtained from the trans-conductance characteristics (Fig.9.4), is below 10^4. From the data presented in Fig. 9.4, the charge carrier mobility in the linear regime ($V_{DS} < V_G - V_T$) can be determined by using the equation 2.5 where C_i is the gate insulator capacitance per unit area. As shown in Fig.9.5 the field-effect mobility depends on the source-drain voltage. With increasing source-drain bias, the mobility increases until it is saturated at 1.5 cm^2/Vs. This means that for a sufficiently large longi-

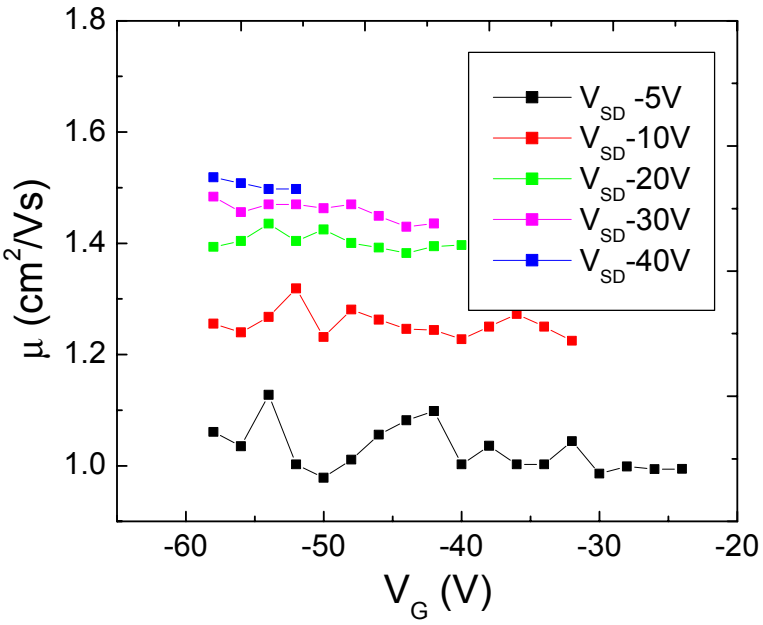

Figure 9.5: *The carrier mobility of a DPh-BDS FET in the linear regime versus the gate bias (obtained from Data in Fig. 9.4)*

tudinal electric field the transistor performance is no longer limited due to the Schottky barrier of the contacts. If we calculate the mobility from the saturation regime ($V_{DS} > V_G - V_T$) applying equation 2.7, the equivalent behavior is found.

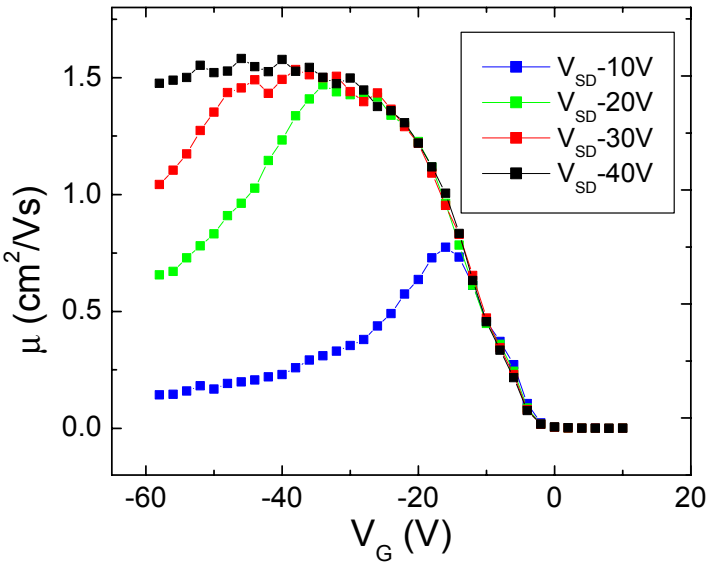

Figure 9.6: *The carrier mobility of a DPh-BDS FET in the saturation regime versus the gate bias (obtained from Data in Fig. 9.4)*

In addition, the same maximum carrier mobility of 1.5 cm^2/Vs can be obtained. V. Podzorov et. al. [PSL$^+$03] and C. Goldmann et. al. [GHK$^+$04] have reported a similar source-drain bias dependence for rubrene single crystal FETs. However, this is not the case for the rubrene single crystal devices I fabricated (see chapter 5, Fig.5.3), where the carrier mobility is independent of the longitudinal field (source-drain voltage). Fig.9.5 also indicates that for a sufficiently large negative gate bias ($V_G < -20V$) the carrier mobility becomes nearly independent of the V_G. This feature reflects the high quality of the crystal, with only a few structural defects [DM02]. It is worth noting that a mobility of 1.5 cm^2/Vs is the highest value I have obtained for a DPh-BDS single crystal device, but that mobilities above 1 cm^2/Vs were routinely measured.

Although the rubrene and DPh-BDS single crystal FETs showed differences in their device performance, the temperature dependence of carrier mobility, displayed in Fig. 9.7 is similar. As already discussed in chapter 5, two transport regimes can be identified: (a) the intrinsic regime observed at high temperatures (300K-280K), where the carrier mobility increases slightly and (b) the shallow trap dominated regime, where an Arrhenius-like dependence of the mobility (see Eq. 3.2) The activation energy is determined (E_A) to be around 25 meV. However, note that at low temperatures the Schottky

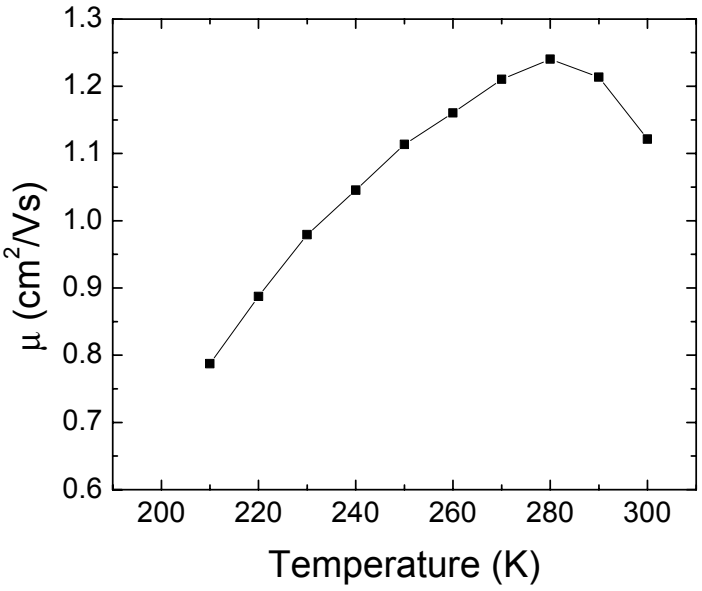

Figure 9.7: *The temperature dependence of carrier mobility calculated from the square root of the saturation current ($V_{SD} = -60V$)*

barrier on the contacts may limit the source drain current and therefore the activation energy calculated from the two electrodes; mobility may need to be corrected for this effect.

To summarize, single crystal FETs based on DPh-BDX compounds show excellent device performance and, compared to thin film devices, their carrier mobility is more than one order of magnitude higher. Special are DPh-BDS devices where I have found that a mobility as high as 1.5 cm^2/Vs can be achieved and that mobility slightly increases with cooling following a strong decrease at low temperatures. Still, I can not conclude that introducing selenium and telluride in aromatic compounds increases the carrier mobility.

Chapter 10

Perylene-TCNQ

This chapter discusses, starting from the individual substances, Perylene and TCNQ (tetracyanoquinonodimethane), the crystal growth, the structure and the field effect properties of the combination Perylene-TCNQ, a charge transfer complex.

10.1 Introduction

The recent high performance of organic field-effect transistors (OFETs) has been accomplished by developing new molecular semiconductor materials [TKK+04, MZB+05]. In the majority of cases prominent organic semiconductor material has been modified by adding or replacing various molecules or atoms to the existing compound. This is done to attempt to enhance the overlap between the neighboring molecules or to change the ionization potential of the compound.

In this chapter I report on a different approach for designing the electronic properties of a semiconductor material in OFETs. To engineer a low Homo-Lumo gap [PBB+02] a electron donor is linked with a electron acceptor. TCNQ is a strong π acid, able to accept one electron owing to the large electronic affinity of its four nitrile symmetric groups and to give a charge transfer reaction with the perylene donor. The family of similar charge-transfer (CT) complexes opens up vast areas of condensed matter physics [IYS98]: their charge carrier properties range from semiconductor over metallic as far as superconductor behavior. Already, Iizuka et. al. [IYS98] has employed a charge transfer complex as a semiconductor material for thin film field effect transistors (TFT). By changing the mixture of TMTSF and TCNQ, they were able to alter the FET characteristic from p-type to n-type. However, for TFTs it is difficult to determine the exact molar ratio between donor

and acceptor and the low carrier mobility indicates that grain boundaries mask the transport properties of the CT. Due to this fact, I decided to use Perylene-TCNQ single crystals to prepare FETs.

10.2 Crystal growth and structure Perylene-TCNQ

Single crystals of perylene-TCNQ were grown by physical vapor transport in a flow of inert gas. Argon was chosen for transport of the perylene TCNQ compounds but other inert gas could be used as well. Both perylene and TCNQ were purchased from Aldrich and used for crystal growth without additional purification. Powder, consisting of a mixture of both substances, was heated in an evaporation zone to 250℃and a 100 cm^3/min flow of argon was directed over the material. In the part of the reactor between the colder zone (held at 200℃) and the evaporation zone (250℃), dark crystals where formed. In the lower temperature area farther in the downstream of argon also pure yellow perylene and TCNQ crystals were formed. Outside the

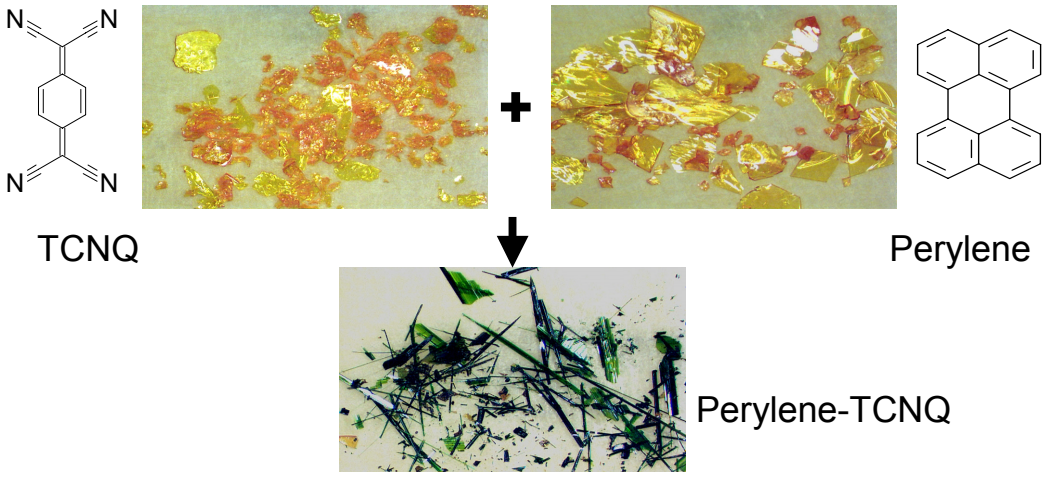

Figure 10.1: *Molecular compound of TCNQ + Perylene*

growth furnace, in the part of the transport tube held at room temperature, a layer of white yellow deposit consisting of impurities was deposited. The composition of the impurities was not closely analyzed. The Needle-like dark crystals with mirror flat side surfaces and the pure and also flat, yellow Perylene and TCNQ were chosen for field effect transistor fabrication and

also x-ray experiments were performed.

As shown in Fig.10.1 the color of crystals from the pure substances Perylene and TCNQ are yellow. The crystals of the CT Perylene-TCNQ on the other hand are black when thick or dark green when very thin.

This drastic change in color of the CT crystals indicates that charge is transferred from the donor Perylene to the acceptor TCNQ. Only a part of an electron is shifted, so the Perylene band is partly empty and the TCNQ band is partially filled thus leaving the charge carriers mobile. A simple model of the band diagram of the pure compounds and the CT is shown in Fig.10.2.

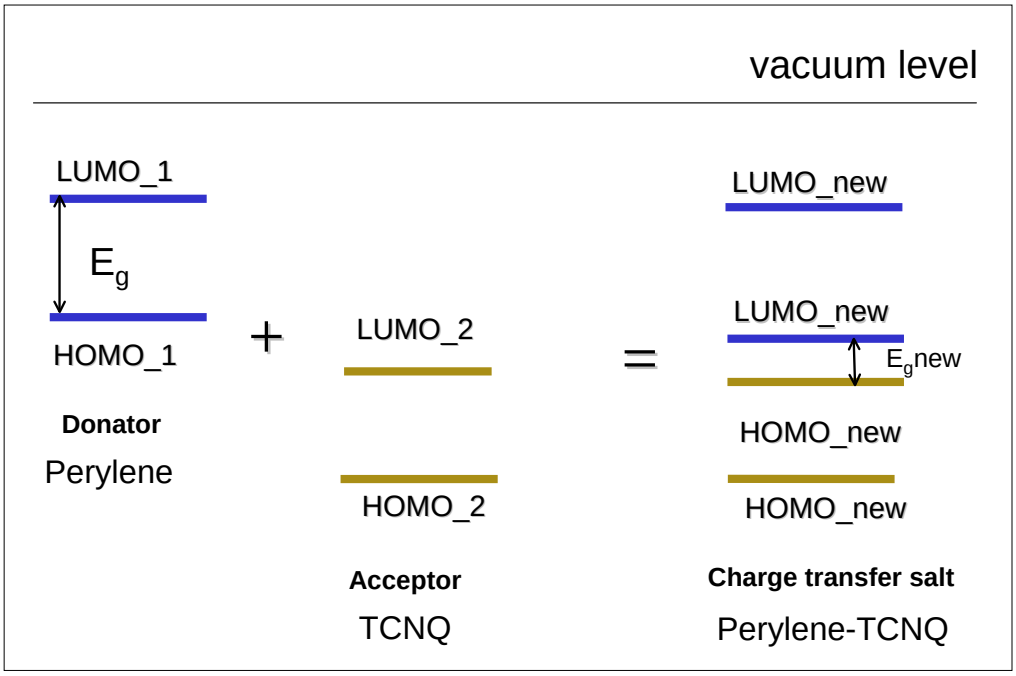

Figure 10.2: *HOMO-LUMO engineering*

The schematic drawing implies that the band gap of the CT is smaller than those of the pure substances. Additionally, to address the color change of the CT crystals, the formation of a molecular compound of TCNQ and Perylene was confirmed by Differential Scanning Calorimetry (DSC)(Fig.10.3). The DSC-measurement was performed by E. Williamson (Bell Laboratories). The CT has a lower melting point (260℃) than the individual compounds TCNQ (297℃) and Perylene (283℃).

The structure of the of the gas-phase-grown Perylene-TCNQ single crystals was confirmed to be the same as described in ref.[TP73]. The molecular

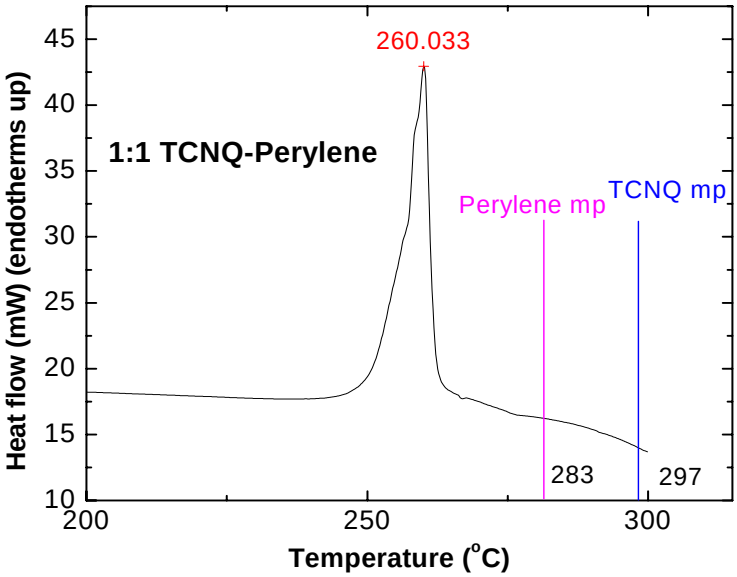

Figure 10.3: *Differential scanning calorimetry*

ratio between Perylene and TCNQ is 1:1. They crystallize in space group $P2_1/b$ Z=2, with monoclinic unit cell parameters a = 7.32Å, b = 14.55Å, c = 10.88 Å, and γ= 90.4°. The molecules stack alternately plane-to-plane along the a-axis of the crystal.

10.3 FET measurements

The single crystal FETs of the pure substances Perylene and TCNQ exhibit only a low field-effect activity. I determined from the saturation regime, by applying equation 2.7 a hole mobility of 10^{-3}cm^2/Vs in Perylene and electron mobility in TCNQ lower than 10^{-3}cm^2/Vs. Menard et al.[MHGR04] reported for TCNQ single crystal FETs a higher electron mobility (2 cm^2/Vs). The low value we obtain from our single crystal FET devices may be explained by the fact that the deposition of the gate-dielectric parylene on the single crystal surface causes more defects in the channel than the PDMS air gap stamps [Pod]. As is shown in Fig.10.4 the single crystal field effect transistors based on CT Perylene-TCNQ functioned as n-type devices. With increasing gate bias V_G, the source-drain current I_{SD} and therefore also the channel conductivity increases. For the best devices an electron mobility of 0.3 cm^2/Vs was archived and a threshold voltage (V_T) of around 10V at $V_{SD} = 50V$ was

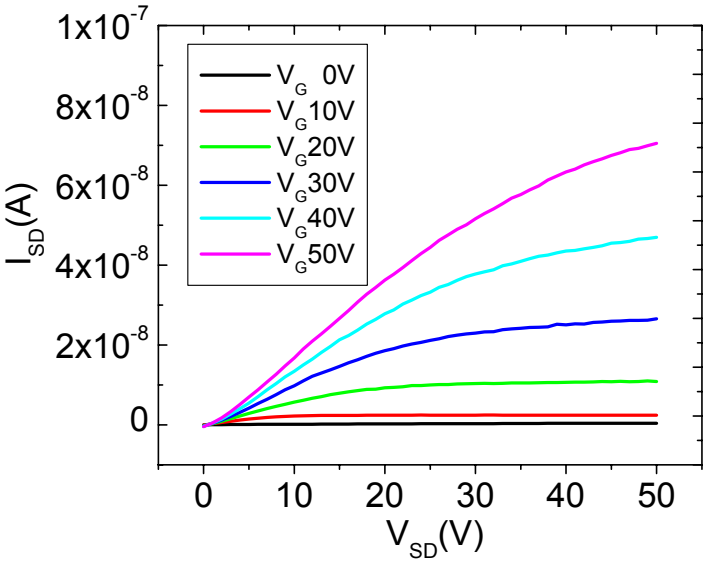

Figure 10.4: *The output characteristic of a Perylene-TCNQ single crystal FET*

determined. The density of the charged traps at the CT Perylene-TCNQ/ Parylene interface is estimated 6 *10 ^{10} cm $^{-2}$.

In conclusion, single crystals of the pure substances Perylene and TCNQ were grown by vapor transport in a stream of inert gas. From both types of crystals, field effect transistors were fabricated. A hole mobility in Perylene and an electron mobility in TCNQ lower than 10^{-3} cm^2/Vs were determined. To engineer the band gap of organic semiconductors, molecular compounds of Perylene and TCNQ (tetracyanoquinonodimethane) were grown. The single crystals of such compounds were grown by gas phase transport. To confirm the formation of the compound Perylene-TCNQ the crystal structure was determined and DSC-measurements were performed. Field effect transistors were fabricated on gas phase Perylene-TCNQ single crystals. An electron mobility as high as 0.3 cm^2/Vs has been measured.

Chapter 11

Summary of OFETs

The field effect performance of all the organic single crystal devices I investigated has been summarized in the following tables. Details on the fabrication and measurement conditions have been described in previous chapters.

Molecules	Crystals	FET-Performance
Decaphenylpentacene 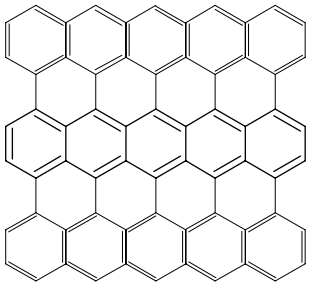 Synthesized in Prof. Nuckolls group, Columbia University	Grown in the flow of inert gas; "platelets-like" crystals	▪ p-type ▪ $\mu = 1.4*10^{-3}$ cm^2/Vs maximal reported mobility ▪ V_T= -22V
Tetraphenylpentacene 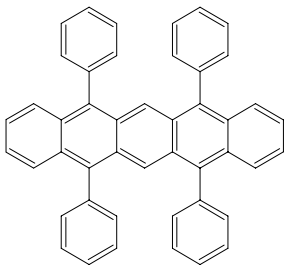 Synthesized in Prof. Nuckolls group, Columbia University	Grown in the flow of inert gas; "platelets-like" crystals	▪ p-type ▪ $\mu = 1*10^{-4}$ cm^2/Vs maximal reported mobility ▪ V_T = -40V

Molecules	Crystals	FET-Performance
Pentacene 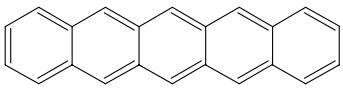 Commercial material from Aldrich	Grown in the flow of inert gas and in a vacuum sealed glass ampoule; "platelets-like" crystals	▪ p-type ▪ $\mu = 2.3$ cm^2/Vs maximal reported mobility ▪ zero threshold operation
Tetracene 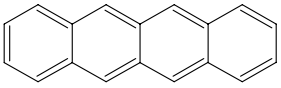 Commercial material from Aldrich	Grown in the flow of inert gas and in a vacuum sealed glass ampoule; "platelets-like" crystals	▪ p-type ▪ $\mu = 0.6$ cm^2/Vs maximal reported mobility $\mu = 1.3$ cm^2/Vs [GHK$^+$04] ▪ V_T= -10V
Antracene 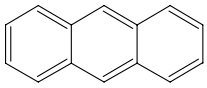 Commercial material from Aldrich	Grown in the flow of inert gas; "platelets-like" crystals	▪ p-type ▪ $\mu = 4.6*10^{-4}$ cm^2/Vs maximal reported mobility $\mu = 0.02$ cm^2/Vs [ALC$^+$04] ▪ V_T= -55V
Rubrene 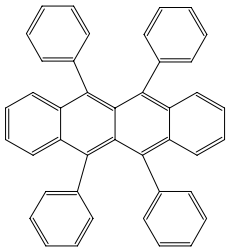 Commercial material from Aldrich	Grown in the flow of inert gas and in a vacuum sealed glass ampoule; "platelets- and needle-like" crystals	▪ p-type ▪ $\mu = 13$ cm^2/Vs maximal reported mobility $\mu = 20$ cm^2/Vs [PMB $^+$04] ▪ zero threshold operation
Dichlorotetracene 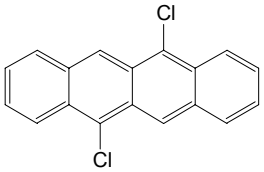 Synthesized in Prof. Bao group, BL and Stanford University	Grown in the flow of inert gas; "platelets- and needle-like" crystals	▪ p-type ▪ $\mu = 1.6$ cm^2/Vs maximal reported mobility ▪ V_T= -13V
Monochlorotetracene 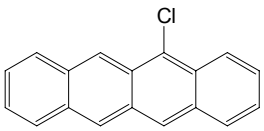 Synthesized in Prof. Bao group, BL and Stanford University	Grown in the flow of inert gas; "platelets- and needle-like" crystals	▪ p-type ▪ $\mu = 0.3$ cm^2/Vs maximal reported mobility ▪ V_T= -13V
	Grown from solution; "platelets-like" crystals	▪ p-type ▪ $\mu = 2.4*10^{-3}$ cm^2/Vs ▪ V_T= -30V

Molecules	Crystals	FET-Performance
Monobromotetracene 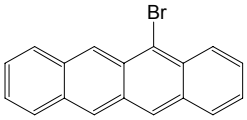 Synthesized in Prof. Bao group, BL and Stanford University	Grown in the flow of inert gas; "platelets-and needle-like" crystals	▪ p-type ▪ μ = 0.2 cm^2/Vs maximal reported mobility ▪ V_T= -5V
	Grown from solution; "platelets-like" crystals	▪ p-type ▪ $\mu = 1.4*10^{-3}$ cm^2/Vs ▪ V_T= -30V
Copper phthalocyanine 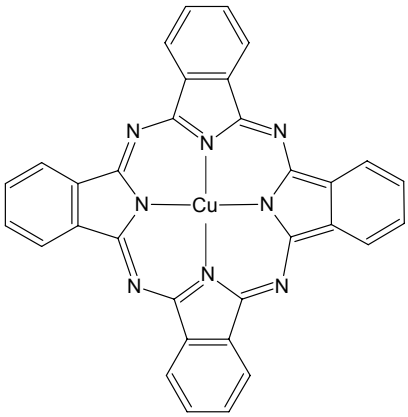 Commercial material from Aldrich	Grown in a flow of inert gas; cm long "needle-like" crystals	▪ p-type ▪ μ = 1 cm^2/Vs maximal reported mobility ▪ V_T= -5V
Fluorinated copper phthalocyanine 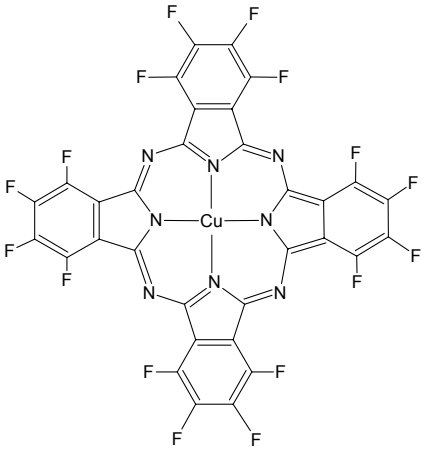 Commercial material from Aldrich	Grown in a flow of inert gas; cm long "needle-like" crystals	▪ n-type ▪ μ = 0.06 cm^2/Vs maximal reported mobility ▪ V_T= 6V
Rubrene-Impurity 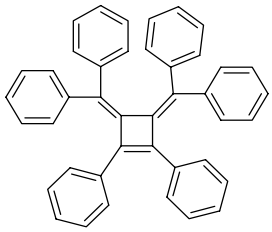 Byproduct of the commercial material from Aldrich	Grown in the flow of inert gas; "needle-like" crystals	▪ p-type ▪ μ = 0.02 cm^2/Vs maximal reported mobility ▪ V_T= -15V

Molecules	Crystals	FET-Performance
DPh-BDT 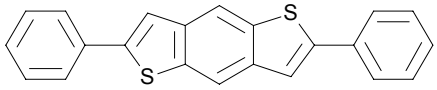 Synthesized in Prof. Takimiya group, Hiroshima University	Grown in the flow of inert gas; "platelets-like" crystals	▪ p-type ▪ μ = 0.4 cm^2/Vs maximal reported mobility ▪ V_T= -22V
DPh-BDS 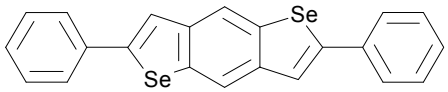 Synthesized in Prof. Takimiya group, Hiroshima University	Grown in the flow of inert gas; "platelets-like" crystals	▪ p-type ▪ μ = 1.5 cm^2/Vs maximal reported mobility ▪ V_T= -6V
DPh-BDTe 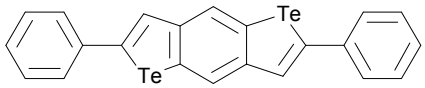 Synthesized in Prof. Takimiya group, Hiroshima University	Grown in the flow of inert gas; "platelets-like" crystals	▪ p-type ▪ μ = 0.5 cm^2/Vs maximal reported mobility ▪ V_T= -5V
Dimethylpentacenequinone 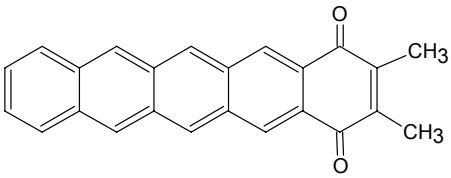 Synthesized in Prof. Nuckolls group, Columbia University	Grown in the flow of inert gas; "needle-like" crystals	▪ p-type ▪ μ = 2*10^{-4} cm^2/Vs maximal reported mobility ▪ V_T= -28V
Hexacenequinone 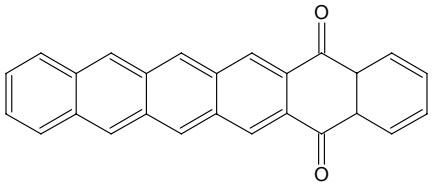 Synthesized in Prof. Nuckolls group, Columbia University	Grown in the flow of inert gas; "needle-like" crystals	▪ p-type ▪ μ = 8*10^{-4} cm^2/Vs maximal reported mobility ▪ V_T= -38V

Molecules	Crystals	FET-Performance
Coronene 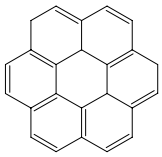 Commercial material from Aldrich	Grown in the flow of inert gas; "platelets-like" crystals	▪ p-type ▪ $\mu = 2*10^{-4}$ cm^2/Vs maximal reported mobility ▪ V_T= -70V
TCNQ 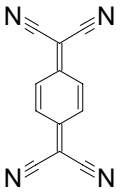 Commercial material from Aldrich	Grown in the flow of inert gas; "platelets-like" crystals	▪ n-type ▪ $\mu \sim 1*10^{-6}$ $\mu = 2$ cm^2/Vs [BGMP04] cm^2/Vs maximal reported mobility $\mu = 2$ cm^2/Vs [BGMP04] ▪ $V_T \sim$ -75V
Perylene 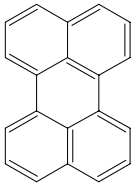 Commercial material from Aldrich	Grown in the flow of inert gas; "platelets-like" crystals	▪ p-type ▪ $\mu = 4.3*10^{-3}$ cm^2/Vs maximal reported mobility ▪ V_T= -35V
Perylene-TCNQ 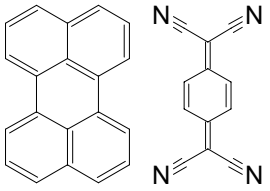 Charge transfer compound	Grown in the flow of inert gas; "needle-like" crystals	▪ n-type ▪ $\mu = 0.3$ cm^2/Vs maximal reported mobility ▪ V_T= 10V
	Grown from solution; "needle-like" crystals	▪ n-type ▪ $\mu = 2.4*10^{-3}$ cm^2/Vs maximal reported mobility ▪ V_T= 10V
Tetraflurotetracene 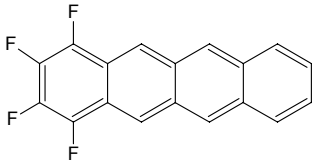 Synthesized in Prof. Nuckolls group, Columbia University	Grown in the flow of inert gas; "needle-like" crystals	▪ p-type ▪ $\mu = 7*10^{-3}$ cm^2/Vs maximal reported mobility ▪ V_T= -22V

Chapter 12

Transition metal dichalcogenides

The inertness of the Van der Waals face of layered transition metal dichalcogenides (TMDs) against chemical reaction in general, and photocorrosion in particular, is among the leading factors for the interest in photovoltaic based materials [Buc92]. So far, they have not been considered to be promising as semiconductor materials for field effect transistors. In this chapter transition metal dichalcogenides, in particular WSe_2, will be evaluated for future device applications.

12.1 TMDs for FET devices?

In modern electronics, the requirements for field effect devices are stringent and often contradictory, e.g., a combination of high charge carrier mobility and mechanical flexibility. Neither of the developed types of FETs satisfies these requirements. For example, silicon FETs have a relatively high μ =500 cm^2/Vs [TTIT94]. However, because of high processing temperatures, the Si-based technology is incompatible with the emerging field of "flexible" electronics. On the other hand, the organic-based FETs that provide the basis for inexpensive, flexible and lightweight electronic devices [SBB$^+$97, Hor98, KB00, Rog01, DTK95, Kla02] are notoriously known for their low charge carrier mobility and poor chemical stability. Although several novel materials have recently been considered for FETs [RNJ99, KMD99, Dua03], the quest for new semiconducting materials and fabrication technologies is a high priority task for the electronic industry. The FET performance depends critically on two parameters: the threshold gate voltage (V_T), corresponding to the formation of the conducting channel, and the mobility of the field-induced

charge carriers (μ). With respect to these parameters, conventional inorganic and organic semiconductors are at opposite ends of a wide spectrum of materials potentially suitable for FET fabrication. Indeed, strong covalent bonding of atoms in inorganic semiconductors such as Si results in a small effective mass of charge carriers and relatively high charge carrier mobility. However, the covalent bonding also leads to a large concentration of chemically active dangling bonds at the Si surface, which trap the field-induced charge. From the year 1947, when J. Bardeen realized the importance of surface states, it took more than two decades to invent the techniques for passivation of the surface charge traps, a critical step in the Si-based FET technology [RH97]. In contrast to Si, the surface of weakly bonded van-der-Waals organic semiconductors (e.g., polyacenes [Hor98, KB00] and conjugated polymers [Sir99]) is characterized by a low density of dangling bonds, and, hence, an intrinsically low density of surface traps. This advantage, however, comes at the price of a low carrier mobility ($\sim$0.1-20 cm^2/Vs) because of the large effective mass of polaronic charge carriers in organic semiconductors (see, e.g. [KH81, PMB$^+$04]).

Field effect transistors based on transition metal dichalcogenides combine several advantages of the existing FETs. The unique structure of these materials results in a highly inert, trap-free basal surface of the single crystals and enables fabrication of FETs with an intrinsically low field-effect threshold and a high mobility of charge carriers, comparable to that in the best single-crystal Si devices. The TMD-based transistors can operate in both electron- and hole-accumulation modes depending on the polarity of the gate voltage (the so-called ambipolar operation, which is rarely observed in high-mobility FETs). Finally, these novel FETs survive bending, owing to the mechanical flexibility of TMD crystals and the polymer parylene film used as the gate insulator. All these properties make the TMD-based transistors very attractive for applications in "flexible" electronics. Field-effect activity has been observed for several transition metal dichalcogenides ($WSe_2, MoSe_2, SnS_2, HfS_2$). However, I focus on the characteristics of the WSe_2-based device.

12.2 FET-characteristics of WSe_2

The dependence of the source-drain current (I_{SD}) on the gate voltage (V_G) for a WSe_2 FET, measured at a fixed source-drain voltage (V_{SD}), the so-called trans-conductance characteristic, is shown in Fig. 12.1. Formation of a conducting channel between the source and drain contacts is manifested by the sharp increase of I_{SD} by several orders of magnitude at both nega-

tive V_G (the p-type conductivity) and positive V_G (the n-type conductivity). The ability of an FET to operate in both electron- and hole-accumulation modes is known as ambipolar operation. A non-zero threshold voltage, V_T, indicates that, despite the chemical inertness of the WSe_2 surface, a small density of charge traps ($\sim 5 \times 10^{11} cm^{-2}$) is still present at the semiconductor/dielectric interface. These traps immobilize a fraction of the field-induced

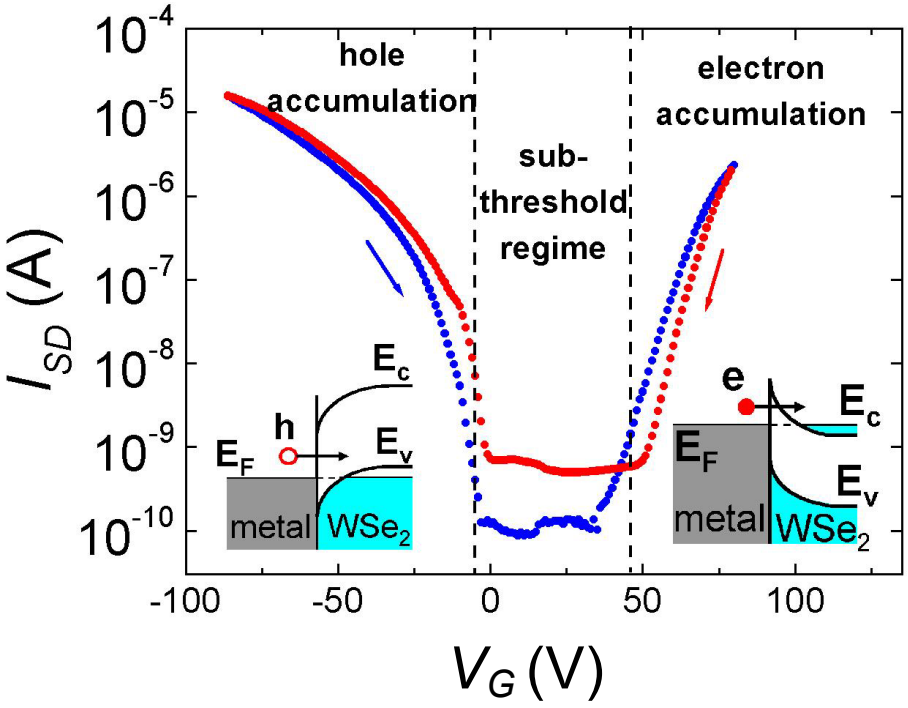

Figure 12.1: *The trans-conductance characteristics of a WSe_2 FET measured at 60 K. The polarity and magnitude of the source-drain voltage in these measurements were fixed ($V_{SD} = +10V$).*

charge and reduce the effective density of the mobile carriers. The conduction channel between the source and drain is formed only when V_G exceeds V_T. The observed hysteresis corresponds to sweeping V_G in the opposite directions shown by arrows. The insets in Fig. 12.1 show bending of the valence (E_V) and conduction (E_C) bands of the semiconductor at the interface between the metallic electrodes and the conduction channel. Depending on the polarity of the gate voltage, either holes are injected into the valence band (at $V_G < 0$), or electrons are injected into the conduction band (at $V_G > 0$). E_F shows the position of the Fermi level of metal. Non-zero

conductivity in the sub-threshold regime (Fig. 12.1) is mostly due to the bulk conductivity of WSe_2 crystals, which could be relatively large at high temperatures. Reports of ambipolar operation in symmetric FETs with a

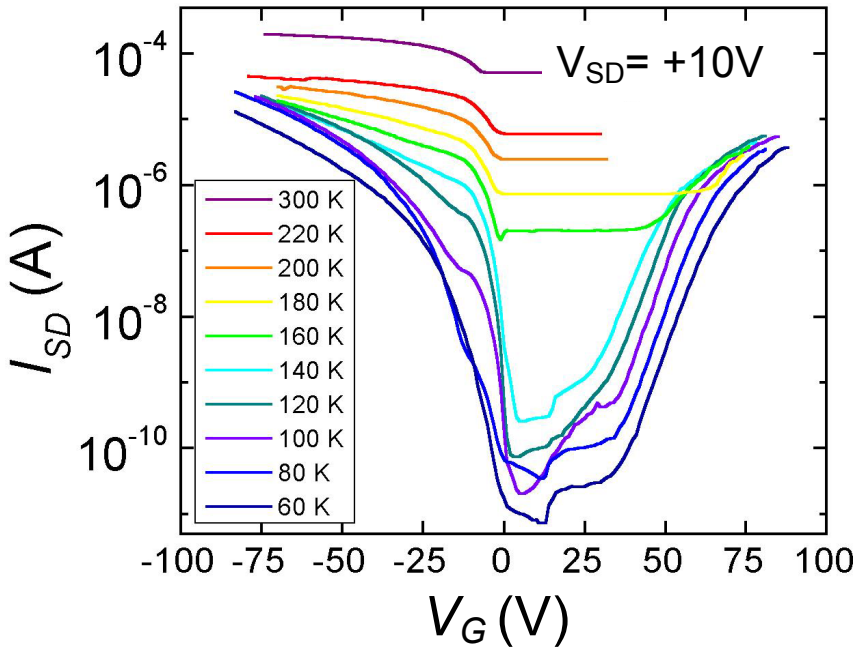

Figure 12.2: *Trans-conductance characteristics of a WSe_2 FET measured at different temperatures at a constant source-drain voltage of fixed polarity ($V_SD = +10V$).*

single conducting channel are rare. Notable examples include the amorphous silicon (α-Si) FETs with rather low electron and hole mobilities (0.1 and 2×10^{-3} cm^2/Vs, respectively) [MN80, Pfl86], and the FETs based on carbon nanotubes [Mar01, Mis03, MYS$^+$04]. Ambipolar transport has been also observed in the organic heterostructure FETs with two active layers made of n- and p-type materials [DTK95, DKTH96] as well as for charge-transfer salt devices [HMTB04]. In the latter case, however, the hole and electron currents are spatially separated. For the ambipolar operation, both the source and drain contacts are required to be efficient n- and p-type injectors. This situation is possible if the Schottky barrier at the interface between the metallic contact and a semiconductor is sufficiently small for both electron and hole injection. Typically, this requires a not-too-large band gap of the semiconductor and an absence of the Fermi level pinning at the semiconductor surface (the pinning is usually caused by the surface charge traps)[HMTB04]. Low

density of charge traps on the chemically inert surface of WSe2 crystals and the relatively small band gap ($\sim 1.2eV$ [LCF87]) facilitate the ambipolar charge injection in WSe_2 devices. The asymmetry of the trans-conductance characteristics with respect to $V_G = 0$ in Fig. 12.1 is caused by substantially different thresholds for n- and p-type operation, as well as by the positive polarity of the source potential ($V_{SD} = +10V$) maintained the same for both negative and positive V_G The hysteresis of the $I_{SD}(V_G)$ dependence has been observed by reversing the V_G sweep at low temperatures ($T \leq 100K$). Similarly to α-Si FETs [KLGP91], it reflects slow "re-charging" of the surface traps on a time scale comparable with the measurement time (the V_G sweep rate was 5 V/min).

The trans-conductance characteristics measured over a wide temperature range are shown in Fig. 12.2. In these measurements, the gate voltage was varied from negative to positive values. The bulk conductivity of WSe_2 decreases rapidly with cooling, and as a result the on/off ratio exceeds 10^4 at $T \leq 150K$. Relatively high bulk conductivity at room temperature is due to an unintentional p-type doping of WSe_2 crystals. Provided that the doping level can be reduced by further optimization of the crystal growth, low room-temperature bulk conductivity and, hence, a high on/off ratio can be realized.

In the ambipolar devices, the electrons and holes can be injected simultaneously into opposite ends of the conduction channel. This interesting situation can be realized if the transverse electric field has opposite signs near the source and drain contacts (as shown in the inset to Fig. 12.3). To illustrate this regime, let us consider the case V_G, $V_{SD} > 0$. Fig. 12.3 shows the I_{SD} dependence for several positive values of V_G. At relatively small $V_G < 40V$ and large $V_{SD} > V_G$, the gate is negatively biased with respect to the source, and the p-type accumulation layer is formed near the source contact. The injection of holes from the source is manifested by a steep increase of the current with V_{SD}. The electron injection from the drain is suppressed in this biasing regime because of a relatively large threshold $V_T(n)$ for formation of the n-type channel ($> 30V$, see Fig. 12.2). However, when V_G exceeds $V_G(n)$, the shape of $I_{SD}(V_{DS})$ characteristic in Fig. 12.3 changes dramatically. For large gate voltages ($V_G > 50V$), an initial increase of I_{SD} at small $V_{SD} < 25V$ corresponds to the injection of electrons from the drain and the formation of the n-type channel. With further increase in V_{SD}, a p-type accumulation layer is formed near the source and the carriers of opposite signs are simultaneously injected from the source and the drain contacts. This regime is especially interesting because holes and electrons move within the same channel in opposite directions and can recombine. The recombination may explain the observation of the negative differential resistance (NDR) in

the I-V curves (the NDR regime is clearly seen in Fig. 12.3 at $V_{SD} > 30V$ and large V_G). Since WSe_2 can be considered as an "almost" direct band-gap semiconductor (the direct gap in WSe_2 is only slightly greater than the indirect fundamental band gap [SELS+83]), the electron-hole recombination might result in light emission. This very interesting possibility of creating a light-emitting transistor requires further studies. It is worth mentioning that light emission has been observed in ambipolar carbon nanotube FETs [Mis03].

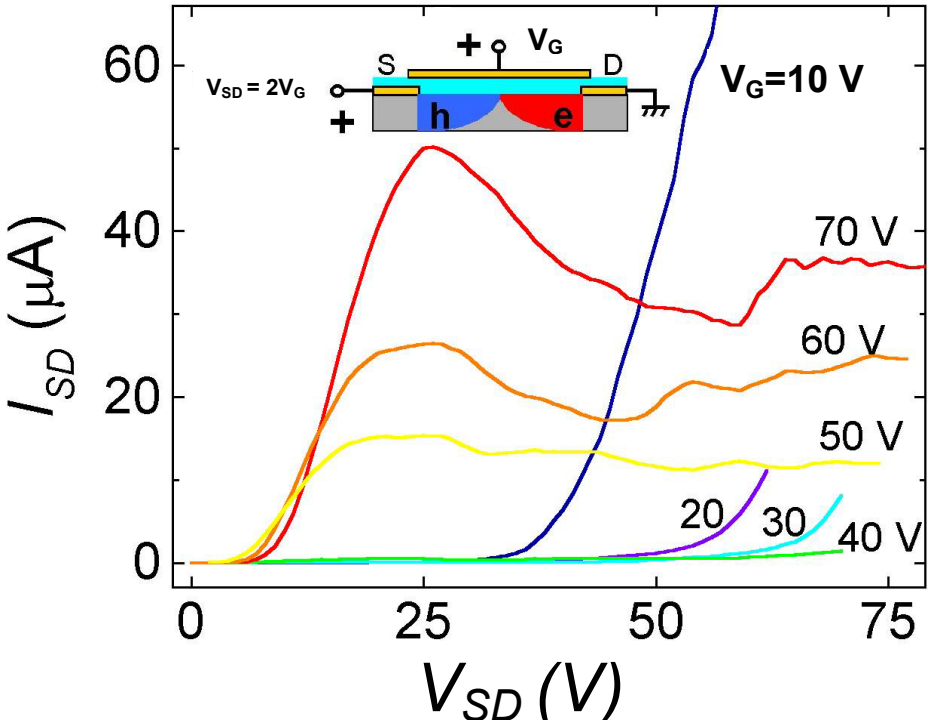

Figure 12.3: *$I_{SD}(V_{DS})$ characteristics of ambipolar WSe_2 FET measured at 120 K for several positive V_G. The inset illustrates the simultaneous formation of the n- and p-type conduction regions when $V_{SD} = 2V_G$.*

Figure 12.4 shows $I_{SD}(V_{SD})$ characteristics for several negative values of V_G. Again, at small $|V_G| < 30V$ and a large negative VS, the electrons are injected from the source contact, and the n-channel formation is manifested by a rapid increase of $|I_{SD}|$. However, at $|V_G| > 40V$, the conduction is dominated by the drain-injected holes. With increasing $|V_{SD}|$ in this regime, I_{SD} exhibits the expected saturation due to the pinch-off of the conducting

channel. The negative differential resistance for this bias regime is weaker; it was observed only for $V_G = -20, -30V$(see the inset in Fig. 12.4). The NDR asymmetry, observed for different bias polarities (compare Figs. 12.3 and 12.4), is due to a substantial difference in the thresholds for formation of the n-type and p-type channels.

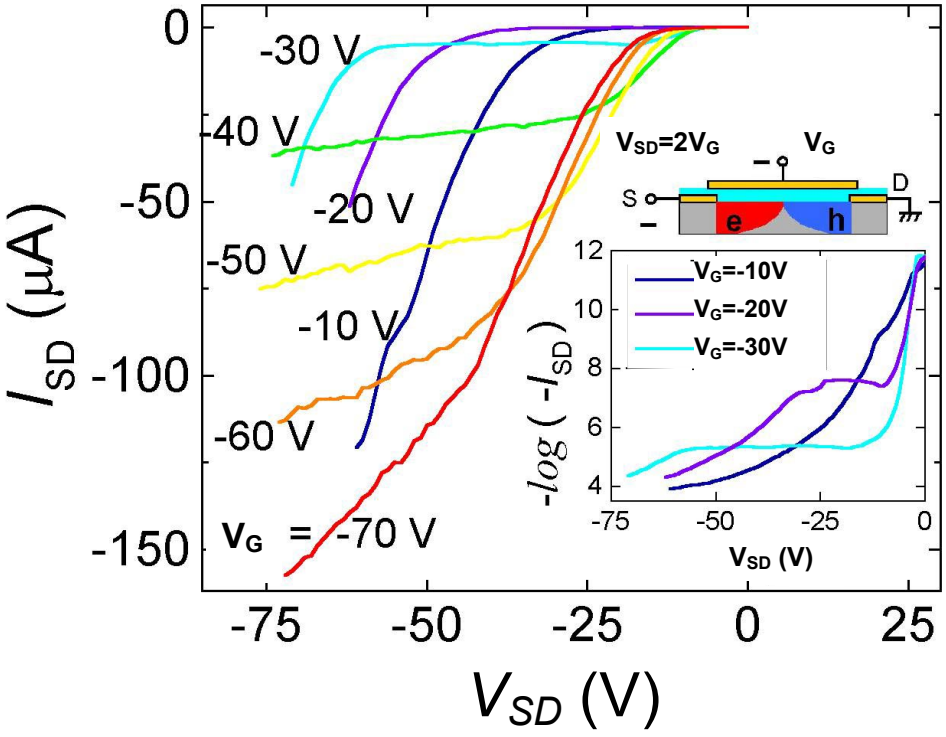

Figure 12.4: $I_{SD}(V_{DS})$ *characteristics of an ambipolar* WSe_2 *FET measured at 120 K for several negative* V_G*. The negative differential resistance was observed at* $V_G = -20, -30V$*; the corresponding curves in the semi-log format are plotted in the inset. The cartoon illustrates simultaneous formation of the n- and p-type conduction regions at* $V_{DS} \sim 2V_G$*.*

For extracting the intrinsic mobility of charge carriers in WSe_2 FETs, i.e. the mobility that is not limited by the contact resistance, we have studied the FETs with an additional pair of voltage probes located between the source and drain contacts. The V_G -dependence of I_{SD} and the potential difference between these voltage probes, V_{12}, for such a gated 4-probe device are shown in Fig. 12.5. This dependence has been measured at room temperature

at fixed $V_{SD} = 1V$. With increasing $|V_G|$, the Schottky contact resistance decreases sharply, and the voltage drop across the middle section of the channel V_{12} increases.

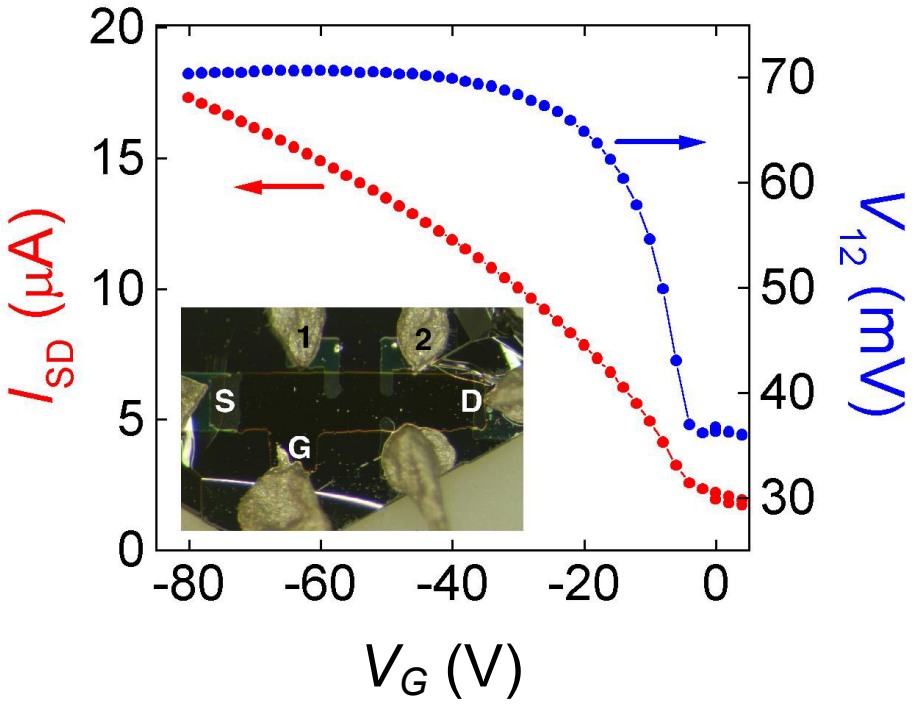

Figure 12.5: *The dependences $I_{SD}(V_G)$ and $V_{12}(V_G)$, measured for a 4-probe WSe_2 FET at a fixed source-drain voltage ($V_{SD} = 1V$) at room temperature. The inset is a photograph of one of the 4-probe devices with the source (S), drain (D), gate (G) electrodes and two voltage probes (1 and 2).*

For sufficiently large $|V_G|$, the dependence $I_{SD}(V_G)$ becomes quasi-linear, which corresponds to a V_G - independent mobility of the charge carriers. In this regime, the intrinsic mobility ~ 500 cm^2/Vs was obtained using the equation for the 4-probe device,

$$\mu = \frac{D}{WC_i} \times \frac{d(I_{SD} - I_0/V_{12})}{dV_G} \tag{12.1}$$

where $C_i = 2 \pm 0.2nF/cm^2$ is the capacitance between the gate and the channel, D is the distance between the voltage probes 1 and 2, and I_0 is the current in the subthreshold regime. This mobility, which is comparable to

the mobility in commercial Si MOSFETs, demonstrates the great potential of the WSe_2 FETs. Note that the "apparent" mobility, estimated from the data in Fig. 12.5 using the conventional 2-probe expression,

$$\mu = \frac{D}{WC_iV_{SD}} \times \frac{d(I_{SD} - I_0)}{dV_G} \tag{12.2}$$

is much lower ($\sim$ 100 cm^2/Vs) because of the contact resistance.

In conclusion, the layered TMDs combine the advantages of organic and inorganic semiconductors: they provide surfaces with an intrinsically low density of trap states and high carrier mobility. Especially promising characteristics have been observed for WSe_2-based devices, which exhibit the intrinsic mobility $\sim$ 500 cm^2/Vs for the field-induced holes at room temperature. This number is comparable to the mobility in the best (non-flexible) Si MOSFETs and exceeds μ in flexible organic TFTs by $\sim$ 3 orders of magnitude. In contrast to the Si devices, the WSe_2 FETs can operate in the ambipolar mode. To the best of our knowledge, this is the first observation of a high-mobility ambipolar regime in a planar symmetric FET. The practical applications of the FETs based on transition metal dichalcogenides might be numerous, provided that the technology of highly-ordered TMD films is developed. The ambipolar FETs can be used in complementary circuits that require both n-type and p-type devices. These devices hold a great promise for optoelectronic applications due to the possibility of radiative recombination of electrons and holes simultaneously injected the conduction channel. The unique electrical characteristics, in combination with mechanical flexibility, make field effect transistors based on transition metal dichalcogenides very attractive for "flexible" electronics.

Chapter 13

Conclusion

With parylene as a gate-dielectric material, I was able to successfully produce FETs based on a variety of organic as well as transition metal dichalcogenide semiconductors. The results of this work are briefly summarized below.

- By employing single crystals, the device performance, including the charge carrier mobility, the field effect threshold, and the subthreshold slope, have been significantly improved. The FET characteristics are no longer limited by the disorder common for thin films.

- To limit the concentration of impurities, it is preferable to grow crystals by physical vapor transport since crystals grown from solution tend to incorporate the solvents into the intra-molecular position in the weakly bonded Van der Waals network of molecules.

- However, organic materials especially are known for undergoing several disproportionation reactions during the sublimation process. The products of these reactions may become embedded into the host crystal. To limit the formation of impurities and therefore improve the electronic charge transport in the crystal the sublimation temperature and the presence of oxygen during the growth process should be reduced.

- If the structure of a molecules is conjugated, impurities themselves can show field effect activity. In general, an important criterion for the choice of potential organic semiconductor material seems to be to pick molecules that consist of an alternating sequence of single and double bonds which allow charge transport though the molecules.

- So far, of all the organic semiconductor materials, rubrene exhibits the best device performance. A mobility anisotropy and an increase of

mobility with cooling indicating intrinsic charge transport was observed only for rubrene single crystal FETs.

- Modifying tetracene molecules allows changing the herring bone packing, thus affecting the electronic transport properties of the system. The π- stacking structure was obtained when two hydrogen atoms of tetracene were substituted by chlorine, and a mobility exceeding that of tetracene was observed along the stack direction. Overall, the π-orbital overlap in the crystal plays a crucial role for the device performance of the semiconductor material.

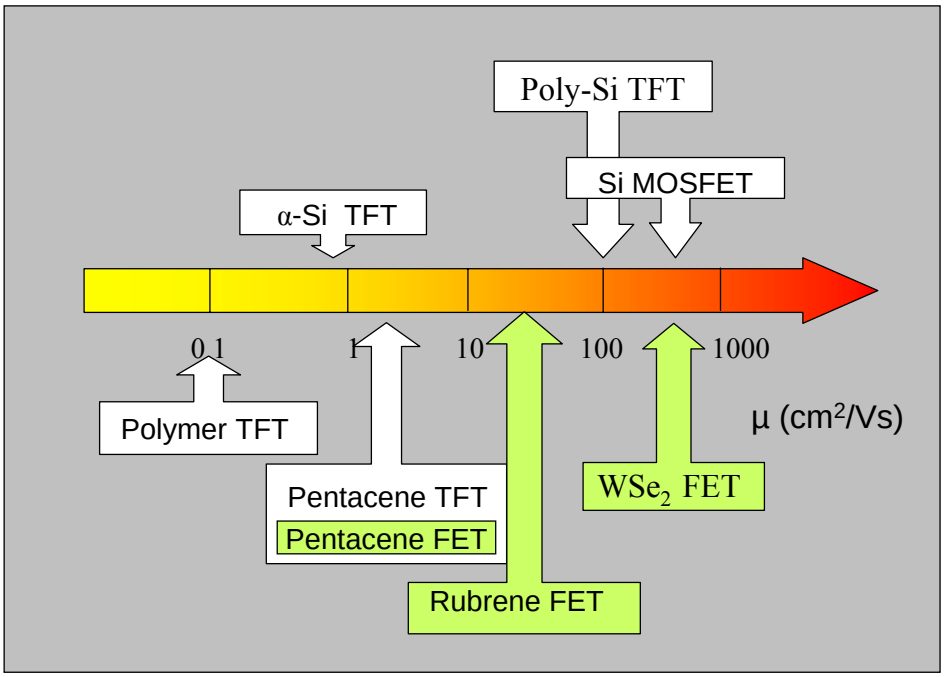

Figure 13.1: *The scale of the field effect mobilities in different types of field effect transistors based on organic and silicon solids. The green labels mark devices that are described in this thesis*

- The perylene-TCNQ charge-transfer salt presents a different approach, where the combination of two different molecules in a crystal produces a partial charge transfer from one molecule type to the other. Here, the molecules alternate in stacks forming a quasi-one-dimensional semiconductor material. This arrangement leads to a small band gap system where n-type field effect activity is observed.

- Layered transition metal dichalcogenides are interesting alternative to organic semiconductors. Similar to organic materials their surface is Van der Waals determined. Therefore, an intrinsic low density of trap states at semiconductor/dielectic interface is observed. The WSe_2-based devices with their high carrier mobilities and ambipolar operation are especially promising.

The schema presented in Fig.13.1 visualize the progress that has been made since the beginning of these thesis studies. The carrier mobilities I achieved for the single crystal FETs based on layered semiconductors are comparable with or even exceed those obtained for the best silicon based devices. Therefore, for future industrial applications, layered semiconductors as presented in this thesis provide a promising basis for novel materials for inexpensive, flexible and lightweight electronic devices.

Chapter 14

Zusammenfassung

Die Verwendung von Parylen als Dielektrikum ermöglichte mir die Untersuchung von Einkristallfeldeffekttransitoren auf der Basis von organischen und anorganischen Halbleitermaterialien. Die Ergebnisse dieser Arbeit sind im folgenden zusammengefasst.

- Die Kenndaten der Feldeffekttransistoren wie Ladungsträgerbeweglichkeit, Steilheit und Schwellenspannung konnten durch die Verwendung von Einkristallen deutlich verbessert werden, da der Ladungstransport in Einkristallen nicht durch Korngrenzen limitiert ist.

- Aus der Gasphase gezogene Kristalle zeigen deutlich bessere Transporteigenschaften als jene aus der Lösung. Da organischen Kristalle aus einzelnen Molekülen aufgebaut sind, welche nur durch van der Waals Kräfte zusammengehalten sind, werden Lösungsmittelreste daher einfach ins Kristallgitter eingebaut.

- Problematisch für die Qualität der Kristalle kann auch der Gasphasentransport sein. Speziell für Pentacen sind unter dem Einfluss von hohen Temperaturen und Sauerstoff eine Vielzahl von Zerfallsprodukten bekannt. Diese können wiederum zu Kristallverunreinigungen und Kristallbaufehlern führen. Daher hat sich das Züchten der Pentacenkristalle im Vakuum bei einer niedrigen Sublimationstemperatur besonders bewährt. Die Transporteigenschaften der Kristalle konnten aufgrund dieser Methode signifikant verbessert werden.

- Auch Materialverunreinigungen selbst können Feldeffekt zeigen, falls die Verbindung eine konjugierte Molekülstruktur aufweist. Dies ist generell ein wichtiges Kriterium für die Auswahl potenzieller organischer Halbleitermaterialien. Nur die konjugierte Struktur ermöglicht einen optimalen Ladungsträgertransport im Molekül.

- Von alle untersuchten organischen Halbleitern ist das Material Rubren besonders hervorzuheben. Die Rubren-Einkristalltransistoren weisen die höchste Ladungsträgerbeweglichkeit und die niedrigste Schwellenspannung auf. Faktoren wie Zunahme der Ladungsträgerbeweglichkeit bei sinkenden Temperaturen und der Anisotropie der Ladungsträgerbeweglichkeit bezüglich der Kristallstrukur deuten darauf hin, dass intrinsische Transporteigenschaften in Rubren-Einkristalltransistoren beobachtet werden.

- Werden bei einem Tetracenmolekül zwei Wasserstoffatome durch zwei Chloratome ersetzt so hat dies vor allem Einfluss auf die Kristallstruktur. Durch diese Modifikation kann die Überlappung der π-Orbitale im Kristall verbessert werden, diese wiederum bestimmen wesentlich die Transporteigenschaften des Materials. Daher wird für Dichlorotetracen-Einkristalle eine höhere Ladungsträgerbeweglichkeit gemessen als für reines Tetracen.

- Das Kombinieren zweier Moleküle Perylen und TCNQ führt zu einer weiteren Materialklasse, den Ladungstransfer-Salzen. Die quasi eindimensionale Kristallstruktur befördert den parzillen Ladungstransfer zwischen Perylen und TCNQ. Die Transistoren dieses Mischsystems sind n-type.

- Die Familie der Schicht-Übergangsmetall-Dichalkogenide sind eine interessannte Alternative zu organischen Halbleitern. Ähnlich wie die organischen Materialien besitzen auch sie eine van der Waals Oberfäche, welche für eine geringe Defektdichte am Interface Isolator / Halbleiter verantwortlich ist. Besonders vielversprechend sind WSe_2-Einkristalltransistoren mit ihrer hohen Ladungsträgermobilität für Löcher und Elektronen.

Bibliography

[AEP02] J. E. Anthony, D. L. Eaton, and S. R. Parkin. *Org. Lett.*, 4:15, 2002.

[Bao04] Zh. Bao. *Nat. Mat.*, 3:137, 2004.

[BB48] J. Bardeen and W.H. Brattain. *Phys. Rev.*, 74:230, 1948.

[Bes04] C. Besnard. PhD thesis, Lund, 2004.

[BGMP04] R.W. I. De Boer, M. E. Gershenson, A. F. Morpurgo, and V. Podorov. *Phys. Status Solid*, A 201 (6):1302, 2004.

[BLC$^+$] V. Y. Butko, D. V. Lang, X. Chi, J. C. Lashley, and A. P. Ramirez. to be publised.

[BLD96] Zh. Bao, A. J. Lovinger, and A. Dodabalapur. *Appl. Phys. Lett.*, 69:3066, 1996.

[BLR04] V. Y. Butko, J. C. Lashley, and A. P. Ramirez. *cond-mat/0405077*, 2004.

[Bub60] R. H. Bube. *Photoconductivity in solids.* Wiley, New York, 1960.

[Buc92] E. Bucher. *Photovoltaic properties of solid state junctions of layered semiconductors, in Photoelectrochemistry and Photovoltaics of Layered Semiconductors.* Kluwer Academic Publishers, Dordrecht, Boston, London, 1992.

[CBB01] J. Cornil, D. Beljonne, and J. L. Bredas. *Adv. Mater*, 13:1053, 2001.

[CCK04] M. D. Curtis, J. Cao, and J. W. J. Kampf. *J. Am. Chem. Soc.*, 126:4318, 2004.

[DBC90] J. A. Doge, J. D. Bain, and A. R. Chamberlin. *J. Org. Chem.*, 55:4190, 1990.

[dDvdW27] H. de Diesbach and E. von der Weid. *Helv. Chim. Acta*, 10:886, 1927.

[DFG+98] C. D. Dimitrakopoulos, B. K. Furman, T. Graham, S. Hegde, and S. Purushothaman. *Syn. Met.*, 92:47, 1998.

[DKP+99] C. D. Dimitrakopoulos, I. Kymissis, S. Purushothaman, D. A. Neumayer, P. R. Duncombe, and R. B. Laibowitz. *Adv. Mater.*, 11:1372, 1999.

[DKTH96] A. Dodabalapur, H. E. Katz, L. Torsi, and R. C. Haddon. *Appl. Phys. Lett.*, 68:1108, 1996.

[DM02] C. D. Dimitrakopoulos and P. R. L. Malenfant. *Adv. Mater.*, 14:99, 2002.

[DPK+99] C. D. Dimitrakopoulos, S. Purushothaman, J. Kymissis, A. Callegari, and J. M. Shaw. *Science*, 283:822, 1999.

[DTK95] A. Dodabalapur, L. Torsi, and H. E. Katz. *Science*, 268:270, 1995.

[Dua03] X. Duan. *Nature*, 425:274, 2003.

[EH69] D. Emin and T. Holstein. *Ann. Phys.*, 53:439, 1969.

[Emi85] D. Emin. *Basic issue of electronic transport in insulating polymers*. Marcel Dekker, New York, (1985).

[FSMP98] G. G. Fedoruk, D.I. Sagaidak, A. V. Misevich, and A. E. Pochtenny. *Sensors and Actuators*, B 48:351, 1998.

[GD88] A. Gravezzotti and G. R. Desiraju. *Acta Cryst. B*, 44:427, 1988.

[GHK+04] C. Goldmann, S. Haas, C. Krellner, K. P. Pernstich, D. J. Grundlach, and B. Batlogg. cond-mat/ 0403210, 2004.

[GHRH99] G.Horowitz, R. Hajlaoui, Bourguiga R, and R. Hajlaoui. *Syn. Met.*, 101:401, 1999.

[HHH00] G. Horowitz, M. E. Hajlaoui, and R. Hajlaoui. *J. Appl. Phys.*, 87:4456, 2000.

[HMTB04] T. Hasegawa, K. Mattenberger, J. Takeya, and B. Batlogg. *Phys. Rev. B*, 69:245115, 2004.

[Hol59] T. Holstein. *Ann. Phys.*, 8:343, 1959.

[Hor98] G. Horowitz. *Adv. Mater.*, 10:365, 1998.

[Hor99] G. Horowitz. *J. Mater. Chem.*, 44:2021, 1999.

[IMO88] M. Iyoda, A. Mizusuna, and M. Oda. *Chem. Lett.*, 1:149, 1988.

[IYS98] T. Ishiguro, K. Yamaji, and G. Saito. *Organic Superconductors*. Springer-Verlag, Berlin, (1998).

[JBP04] O. D. Jurchescu, J. Baas, and T. T. M. Palstra. *cond-mat/ 0404130*, 2004.

[KA60] D. Khang and M.M. Atalla. Silicon-silicon dioxide field induced surface devices. In Carnegie Institute of Technology, editor, *IRE Solid-State Devices Res. Conf.*, Pittsburgh, Pa., 1960.

[Kar90] N. Karl. *Defect control in Semiconductors*. Elsevier North Holand, Amsterdam, 1990.

[KB00] H. E. Katz and Z. Bao. *J. Phys. Chem.*, B 104:671, 2000.

[KH81] K. C. Kao and W. Hwang. *Electrical Transport in Solids*. Pergamon Press, Oxford, 1981.

[Kla02] H. Klauk. *J. Appl. Phys.*, 92:5259, 2002.

[KLGP91] J. Kanicki, F. R. Libsch, J. Griffith, and R. Polastre. *J. Appl. Phys.*, 69:2339, 1991.

[KM01] N. Karl and J. Marktanner. *Molecular crystals and liquid crystals*, 355:149, 2001.

[KMD99] C. R. Kagan, D. B. Mitzi, and C. D. Dimitracopoulos. *Science*, 286:945, 1999.

[KSSL97] Ch. Kloc, P. G. Simpkins, T. Siegrist, and R. A. Laudise. *J. Cryst. Growth*, 182:416, 1997.

[LCF87] J. R. Lince, D. J. Carré, and P. D. Fleischauer. *Phys. Rev. B*, 36:1647, 1987.

[LGNJ97] Y. Y. Lin, D. J. Gundlach, S. F. Nelson, and T. N. Jackson. *IEEE Trans. Electron Devices*, 44:1325, 1997.

[Lie77] R. M. A. Lieth. *Preparation and Crystal Growth of Materials with Layered Structures*. D. Reidel Pub. Co., Dordrecht, Holland; Boston, USA, 1977.

[Lil30] J.E. Lilienfeld. *U.S. patent*, 1,745.175, 1930.

[LKSS98] R.A. Laudise, Ch. Kloc, P.G. Simpkins, and T. Siegrist. *J. Cryst. Growth*, 187:449, 1998.

[LPS03] T. Lindner, G. Paasch, and S. Scheinert. *48. Internationales Wissenschaftliches Kolloquium Technische Universitaet Ilmenau*, 2003.

[LR36a] R.P. Linstead and J.M Robertson. *J. Chem. Soc. London*, page 1736, 1936.

[LR36b] R.P. Linstead and J.M Robertson. *Strukturbericht*, 4:320, 1936.

[LS70] P. G. LeComber and W. E. Spear. *Phys. Rev. Lett.*, 25:509, 1970.

[Mar01] R. Martel. *Phys. Rev. Lett.*, 87:256805, 2001.

[Mat02] C. C. Mattheus. PhD thesis, Groningen, 2002.

[MHGR04] E. Menard, V. Podzorov S.-H. Hur, A. Gaur M.E Gershenson, and J. A. Rogers. *Adv. Materials*, 16:2097, 2004.

[Mis03] J. A. Misewich. *Science*, 300:783, 2003.

[MN80] M. Matsumura and Y. Nara. *J. Appl. Phys.*, 51(12):6443, 1980.

[MT83] F. H. Moser and A.L. Thomas. *The Phthalocyanines*. CRC, 1983.

[MYS+04] E. D. Minot, Y. Yaish, V. Sazonova, J. Y. Park, M. Brink, and P. L. McEuen. *cond-mat/0211152*, 2004.

[MZB+05] H. Moon, R. Zeis, J. E. Borkent, C. Besnard, A. Lovinger, T. Siegrist Ch. Kloc, and Z. Bao. *JACS*, 127:3069, 2005.

[NLGJ98] S. F. Nelson, Y.-Y. Lin, D. J. Gundlach, and T. N. Jackson. *Appl. Phys. Lett.*, 72:1854, 1998.

[PBB+02] D. F. Perepichka, M. R. Bryce, A. S. Batsanov, E. J. L. McInnes, J. P. Zhao, and R. D. Farley. *Chem. Eur. J. 8*, 20:4656, 2002.

[PCF+02] T. M. Pappenfus, R. J. Chesterfield, C. D. Frisbie, K. R. Mann, J. Casado, J. D. Raff, and L. L. Miller. *J. Am. Chem. Soc.*, 124:4184, 2002.

[Pfl86] H. Pfleiderer. *IEEE Trans. Electron.*, Devices ED-33:145, 1986.

[PK75] K. H. Probst and N. Karl. *Phys. Stat. Sol. (a)*, 27:499, 1975.

[PMB+04] V. Podzorov, E. Menard, A. Borissov, V. Kiryukhin, J. A. Rogers, and M. E. Gershenson. *Phys. Rev. Lett.*, 93:1302, 2004.

[Pod] V. Podzorov. *private communication.*

[PPG03] V. Podzorov, V. M. Pudalov, and M. E. Gershenson. *Appl. Phys. Lett.*, 82:1739, 2003.

[PPG04] V. Podzorov, V. M. Pudalov, and M. E. Gershenson. cond-mat/ 0406738, 2004.

[PS82] M. Pope and C. E. Swenberg. *Electronic processes in organic crystals.* Oxford University Press, 1982.

[PSL+03] V. Podzorov, S. E. Sysoev, E. Loginova, V. M. Pudalov, and M. E. Gershenson. *Appl. Phys. Lett.*, 82:3504, 2003.

[Rap97] L. Rapoport. *Nature*, 387:791, 1997.

[Rem01] M. Remskar. *Science*, 292:479, 2001.

[RH97] M. Riordan and L. Hoddeson. *Crystal fire: the birth of information age.* W.W. Norton & Co., New York London, 1997.

[RKHS97] T. Reinot, W. H. Kim, J. M. Hayes, and G. J. Small. *J. Opt. Soc. Am.*, B 14:602, 1997.

[RKT+] L. Roberson, J. Kowalik, L. Tolbert, Ch. Kloc, R. Zeis, X. Chi, and C. Wilkins. to be publised.

[RNJ99] B. A. Ridley, B. Nivi, and J. M. Jacobson. *Science*, 286:746, 1999.

[Rog01] J. A. Rogers. *Proc. Natl. Acad. Sci.*, 98:4835, 2001.

[SBB+97] Z. Shen, P.E. Burrows, V. Bulovic, S. R. Forrest, and M. E. Thompson. *Science*, 276:2009, 1997.

[SD86] J. A. R. P. Sarma and G. R. Desiraju. *Acc. Chem. Res.*, 19:222, 1986.

[SdBIM04] A. F. Strassen, R. W. I. d. Boer, N. N. Iosad, and A. F. Morpurgo. *cond-mat/0407293*, 2004.

[SELS+83] R. Spaeh, U. Elrod, M. Lux-Steiner, E. Bucher, and S. Wagner. *Appl. Phys. Lett.*, 43:79, 1983.

[SHS89] M. Shur, M. Hack, and J. G. Shaw. *J. Appl. Phys.*, 66:3371, 1989.

[Sie] T. Siegrist. private communication.

[Sir99] H. Sirringhaus. *Nature*, 401:685, 1999.

[SLSO+85] R. Spaeh, M. Lux-Steiner, M. Obergfell, E. Bucher, and S. Wagner. *Appl. Phys. Lett.*, 47:871, 1985.

[SP48] W. Shockley and G.L. Person. *Phys. Rev.*, 74:232, 1948.

[Spa86] R. Spaeh. PhD thesis, Konstanz, 1986.

[Sze85] S. M. Sze. *Semiconductor Devices: Physics and Technology.* Wiley, New York, 1985.

[SZP+04] V. C. Sundar, J. Zaumseil, V. Podzorov, E. Menard, R. L. Willett, T. Someya, M. E. Gershenson, and J. A. Rogers. *Science*, 303:1644, 2004.

[TKK+04] K. Takimiya, Y. Kunugi, Y. Konda, N. Niihara, and T. Otsubo. *JACS*, 126:5084, 2004.

[TMGH92] R. Tenne, L. Margulis, M. Genut, and G. Hodes. *Nature*, 360:444, 1992.

[TP73] I. J. Tickle and C. Keith Prout. *J.C.S. Perkin*, page 720, 1973.

[TTIT94] S. Takagi, A. Toriumi, M. Iwase, and H. Tango. *IEEE Trans. Electron Devices*, 41:2357, 1994.

[TW85] R. Tenne and A. Wold. *Appl. Phys. Lett.*, 47:707, 1985.

[TZ01] R. Tenne and A. Zettl. *Nanotubes from Inorganic Materials*. Springer-Verlag, Berlin Heidelberg, 2001.

[Var48] A. T. Vartanyan. *Zh. Fiz. Khim.*, 22:769, 1948.

[VFO+04] H. Vázquez, F. Flores, R. Oszwaldowski, J. Ortega, R. Pérez, and A. Kahn. *cond-mat/0405491*, 2004.

[YK58] J. Yamashita and T. Kurosawa. *J. Phys. Chem. Solids*, 5:34, 1958.

[YTAKK95] K. Yase, Y. Takahashi, N. Ara-Kato, and A. Kawazu. *Jpn. J. Appl. Phys.*, 34:636, 1995.

[ZLH+96] J. Zhang, J. Liu, J. L. Huang, P. Kim, and C. M. Lieber. *Science*, 274:757, 1996.

[ZWWY04] J. Zhang, J. Wang, H. Wang, and D. Yan. *Appl. Phys. Lett.*, 84:142, 2004.